Civil Engineering and Applied Solutions, 2026; 2(1): 1–11

Civil Engineering and Applied Solutions

Research Article

journal homepage: ceas.journals.umz.ac.ir

CEAS
Civil Engineering
and Applied Solutions

Prediction of Shear Capacity of RC Deep Beams Via a Soft Computing Method

Masoud Mahmoudabadi [a*], Seyed Mohammad Reza Hasani [b]

[a] *Department of Civil Engineering, Faculty of Engineering, University of Qom, Qom, Iran*
[b] *Department of Civil Engineering, Qom Branch, Islamic Azad University, Qom, Iran*

ARTICLE INFO

Keywords:
Shear capacity
Artificial intelligence
Support vector machine
Reinforced concrete deep beam

Article history:
Received 23 August 2025
Accepted 18 September 2025
Available online 01 January 2026

ABSTRACT

It is well known that the shear capacity of RC deep beams is affected by many mechanical and geometric parameters. The accurate prediction of the shear capacity still stands out as one of the major stumbling blocks in structural engineering practice. Traditional prediction methods have often proven less than precise. On the other hand, artificial intelligence-based methods, particularly those represented by SVMs, have presented themselves as a promising alternative. This research employed an enhanced machine learning technique, known as WLS-SVM, to estimate the shear capacity of reinforced concrete deep beams. In assembling a comprehensive dataset, 214 experimental results are obtained from the literature. From selected inputs and outputs, under the supervision of a teaching-learning type approach, a predictive model is derived via WLS-SVM. This model is compared with other AI-based methods and codified design procedures. It presented the best accuracy, with major statistical indicators, including an R^2 of 0.9804, showing the superiority of the WLS-SVM approach when compared to other methods. Therefore, the study's results reveal WLS-SVM as a very accurate and viable option for the structural calculation and design of reinforced concrete deep beams.

1. Introduction

Reinforced concrete (RC) deep beams play a crucial role in construction as structural members and as elements that help in distributing loads, particularly in systems like folded plates, base walls, and pile caps found in tall buildings [1]. Although widely adopted and valued, RC deep beams exhibit notable design differences compared to conventional structural components, mainly because numerous factors considerably affect their nonlinear response and resistance to shear forces. Because of the complex behavior of these beams, there is no universally accepted and precise definition that is consistent across all design codes. However, most codes define a beam as “deep” if the span-to-depth ratio (L/D) is less than 5 [2]. This ratio varies across standards: it is less than 5 in European codes, less than 2.5 in Canadian codes, and less than 4 in American codes. Due to the complexity of the shear mechanism and the wide range of influencing parameters in RC deep beams, developing a general and accurate model to estimate their shear strength is quite challenging. As a result, it is not feasible to calculate the exact shear strength of such beams through a closed-form analytical solution [3]. Over the past few decades, the shear behavior and strength of RC deep beams have received relatively little attention in research. Among the various analytical methods introduced in this context, the strut-and-tie method has emerged as one of the most commonly utilized techniques [4].

In recent decades, the use of artificial intelligence (AI) has gained significant traction as an emerging subject of study within the field of structural engineering [5, 6]. AI has demonstrated great success in simulating complex problems, making it a powerful tool for prediction. It enables structural designers to estimate the performance of reinforced concrete members more accurately. AI-based approaches have proven effective in accurately capturing the complex nonlinear correlations between the shear strength of RC deep beams and the various influencing factors [7]. Therefore, AI-based techniques are increasingly being recognized as innovative and promising tools in the field of civil engineering. Numerous studies have employed artificial intelligence (AI) methods and their

---

[*] Corresponding author.
E-mail addresses: m.mahmoudabadi@qom.ac.ir (M. Mahmoudabadi).

https://doi.org/10.22080/ceas.2025.29893.1037
ISSN: 3092-7749/© 2026 The Author(s). Published by University of Mazandaran.

How to cite this article: Mahmoudabadi, M., Hasani, SMR. Prediction of Shear Capacity of RC Deep Beams Via a Soft Computing Method. Civil Engineering and Applied Solutions. 2026; 2(1): 1-11. doi:10.22080/ceas.2025.29893.1037.

various subfields, such as fuzzy logic and metaheuristic algorithms, in the field of structural engineering [5, 8]. A common trend in AI-based approaches involves developing more efficient models through ensemble modeling [9]. In this approach, new group models are created by combining individual models such that the ensemble model achieves higher learning accuracy and reduced error diversity among its components. In contrast to a single model that is trained on a limited portion of the dataset or under fixed training conditions, ensemble approaches typically produce more reliable and better-generalizing models. This is because different learners may complement each other by avoiding similar errors. Additionally, ensemble learning allows the full exploitation of the training dataset, which is particularly beneficial when only a limited amount of data is accessible. According to Chou and Pham [10], integrating two or more powerful learners within an ensemble framework yields markedly better performance than relying on single learners alone. Therefore, combining multiple learners can help reduce prediction errors and variance in results, as the aggregated outcome typically offers higher accuracy than that of a single learner [7, 9].

Support vector machine (SVM) is recognized as a leading artificial intelligence technique for capturing nonlinear patterns, often outperforming older methods like neural networks in tasks involving classification and regression [11]. First introduced by Vapnik in 1995 [12], SVM falls under the category of supervised learning techniques. In comparison to other similar methods, SVM provides a wide array of advantages, including strong predictive capabilities and the capacity to create precise decision boundaries, even when the training data is limited in size. Additionally, SVM can effectively model complex nonlinear relationships [13]. SVM has been widely applied in various civil engineering applications. For instance, Chen et al. [14] used SVM to predict deformation and stress parameters in tunnels, and Liu et al. [15] employed SVM to model energy consumption in buildings. Several studies [16-18] have made noteworthy contributions in civil engineering that have applied machine learning as a powerful modeling tool.

The least squares support vector machine (LS-SVM) represents an enhanced variant of the standard SVM, integrating additional capabilities and achieving computational efficiency through rapid processing [19]. This approach has shown success in addressing both nonlinear and complex engineering tasks [20]. During the training phase, LS-SVM applies a least squares objective to derive linear equations in the dual formulation. Accordingly, the resulting linear system can be efficiently solved using iterative techniques, such as the conjugate gradient algorithm.

To ensure the best possible performance from both SVM and LS-SVM models, it is essential to accurately tune their parameters. In the case of SVM, this involves selecting suitable values for the regularization factor (γ) and the parameter associated with the RBF kernel (σ). Inappropriate choices for these parameters can significantly reduce the prediction accuracy of the model. Similarly, LS-SVM requires predefined values for the regularization and kernel parameters. It is important to highlight that selecting the best parameter values is a non-trivial process and can be framed as a standard optimization challenge. WLS-SVM, or weighted least squares support vector machine, represents an improved form of LS-SVM, in which error terms are weighted to enhance the performance of the original algorithm [21]. Integrating these weights leads to improved model accuracy in predictions. When evaluated against LS-SVM, the WLS-SVM approach demonstrates superior effectiveness in function approximation applications [22].

In the present study, the WLS-SVM method is employed to predict the shear capacity of reinforced concrete deep beams. Accordingly, the following sections first examine the performance of the WLS-SVM approach, and then assess the prediction results. These outcomes are compared with those obtained from existing design codes and other artificial intelligence methods reported in the literature. The rest of this article will cover parts, shear strength of reinforced concrete deep beams, experimental data, research methodology, data processing, results and discussion, and conclusion.

2. Shear strength of reinforced concrete deep beams

Various methods have been proposed for the design of deep beams. The american concrete institute (ACI) code [23] is based on a truss model, in which the concrete contribution is determined through empirical observations. The shear strength of reinforced concrete deep beams, as defined by ACI provisions, can be calculated using Eqs. 1 to 4.

$$V_c = v_c b_w d = \left(3.5 - 2.5\frac{M_u}{V_u d}\right) \times \left(1.9\sqrt{f_c'} + 2.5\rho_w \frac{V_u d}{M_u}\right) b_w d \tag{1}$$

in these equations, f_c' is the 28-day compressive strength, and ρ_w is the longitudinal reinforcement ratio, calculated using Eq. 2.

$$\rho_w = A_s / b_w d \tag{2}$$

the parameters b_w, M_u, V_u, and d represent the beam width, bending moment at the critical section, shear force, and effective depth of the beam, respectively. In beams containing transverse reinforcement, the nominal shear capacity V_n is calculated as the combined effect of the concrete contribution V_c and the shear reinforcement component V_s, as presented in Eq. 3.

$$V_n = V_c + V_s \tag{3}$$

the term V_s is determined using Eq. 4, where:

$$V_s = \left[\frac{A_v}{12s}\left(1 + \frac{L_n}{d}\right) + \frac{A_{vh}}{12s_2}\left(11 - \frac{L_n}{d}\right)\right] f_y d \tag{4}$$

in Eq. 4, Ln is the effective span of the beam; A_v and A_{vh} are the areas of vertical and horizontal shear reinforcement perpendicular and parallel to the longitudinal reinforcement within spacings s and s_2, respectively; fy is the yield strength of the stirrups; s is the stirrup spacing; and ρv is the ratio of vertical shear reinforcement. Similarly, the canadian standards ssociation (CSA) code [24] estimates the total shear strength of RC deep beams as the sum of concrete and shear reinforcement contributions. In CSA provisions, two different expressions are provided for the concrete contribution v_c, depending on the amount of transverse reinforcement and the effective depth, as shown in Eq. 5, subject to conditions given by Eqs. 6 and 8, or alternatively, Eqs. 7 and 8.

$$v_c = \frac{V_c}{b_w d} = 0.2\sqrt{f_c'} \tag{5}$$

if:

$$A_v \geq \frac{0.006\sqrt{f_c'}\,b_w s}{f_{yv}} \text{ and } d \leq 300\text{mm} \tag{6}$$

or:

$$v_c = \frac{V_c}{b_w d} = \left(\frac{260}{1000+d}\right)\sqrt{f_c'} \geq 0.1\sqrt{f_c'} \tag{7}$$

if:

$$A_v < \frac{0.006\sqrt{f_c'}\,b_w s}{f_{yv}} \text{ and } d > 300\text{mm} \tag{8}$$

the shear contribution from reinforcement in the CSA code is expressed in a manner similar to that defined in the ACI code.

3. Experimental data

3.1. Data description

This work utilizes a dataset comprising 214 experimental observations related to reinforced concrete deep beams. These data were gathered from eight separate experimental investigations reported in the literature [25-32]. Fig. 1 illustrates the details of the RC deep beams.

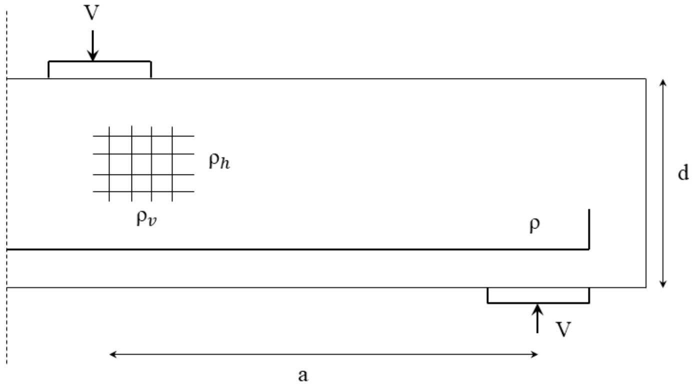

Fig. 1. Geometry of a reinforced concrete deep beam.

The input variables in the WLS-SVM method were selected based on the key parameters influencing the shear capacity of RC deep beams as defined in design codes. Table 1 presents the statistical descriptions of the input and output variables.

Table 1. Summary statistics of input and output data in the current study.

Variables	**Unit**	**Min**	**Max**	**Mean**	**Sdt**
Effective depth (*d*)	mm	217	802	420.7	108.5
Web width of the beam (*b*)	mm	77	306	134.1	49.1
Concrete compressive strength (*f′c*)	MPa	13.9	73.7	33.4	15.89
Shear span-to-effective depth ratio (*a/d*)	-	0.28	2.8	1.23	0.54
Longitudinal reinforcement ratio (ρ)	%	0.53	4.1	1.79	0.69
Horizontal shear reinforcement ratio (ρ_h)	%	0	2.48	0.33	0.46
Vertical shear reinforcement ratio (ρ_v)	%	0	2.66	0.55	0.67
Ultimate shear strength (*V/bd*)	MPa	1.74	13.3	5.4	2.15

4. Research methodology

Support Vector Machines (SVMs) face two significant drawbacks: (1) difficulty in fine-tuning kernel parameters, and (2) heavy dependence on support vectors for defining the decision boundary. To overcome these shortcomings, Suykens et al. [33] proposed the WLS-SVM, which enhances the LS-SVM framework by incorporating weights into the error terms, thereby improving the efficiency in solving a broad range of problems.

Considering a training sample set of size N, denoted by $\{(x_k, y_k)\}_{k+1}^{N}$, where $x_i \in R^d$ represents input data and $y_i \in R$ is the output. Based on this setup, the WLS-SVM model is expressed as the following optimization task in the primal weight domain [34]:

$$\text{Minimize: } J(w,e) = \frac{1}{2}w^T w + \frac{1}{2}\gamma \sum_{i=1}^{N} \bar{v}_i e_i^2$$

$$\text{Subjected to: } y_i = w^T \emptyset(x_i) + b + e_i \qquad (9)$$

$$i = 1,2,\dots,N$$

here, $\emptyset(0): R^d \rightarrow R^{\bar{d}}$ is a mapping function that transforms the input data into a higher-dimensional feature space. The vector $w \in R^d$ represents the weight function in the primal space, while $b \in R$ and $e_i \in R$ represent the bias and error terms, respectively. Within the primal formulation, the learning and optimization task of the WLS-SVM corresponding to Eq. 9 can be written as follows:

$$\mathrm{y(x)} = w^T \emptyset(x) + b \qquad (10)$$

in general, the structure of the mapping function $\emptyset$(x) is unknown, and its direct computation is complex. Hence, solving Eq. 9 directly for w is infeasible. Consequently, the WLS-SVM regression formulation is derived by constructing a corresponding Lagrangian function, as illustrated in:

$$L(w,b,e_i,x) = j(w,e) - \sum_{i=1}^{N} \alpha_i (w^T \emptyset(x_i) + b + e_i - y_i) \qquad (11)$$

where α_i are the Lagrange multipliers. The optimality conditions are determined from:

$$\frac{\partial L}{\partial w} = 0, \frac{\partial L}{\partial b} = 0, \frac{\partial L}{\partial e_i} = 0, \dots, \frac{\partial L}{\partial \alpha_i} = 0 \qquad (12)$$

by eliminating *w* and *e*, the resulting system becomes:

$$\begin{bmatrix} \Omega + V_Y & I_N^T \\ I_n & 0 \end{bmatrix} \begin{bmatrix} a \\ b \end{bmatrix} = \begin{bmatrix} y \\ 0 \end{bmatrix} \qquad (13)$$

where:

$$V_Y = diag\left\{\frac{1}{\overline{v_1}} \dots \frac{1}{\overline{v_N}}\right\}$$

$$\Omega_{i,j} = \langle \emptyset(x_i), \emptyset(x_j) \rangle_H \qquad (14)$$

$$i,j = 1,2,\dots,N$$

$$y = [y_1, \dots, y_N]^T;\ I_N^T[1, \dots, 1]$$

$$\alpha = [\alpha_1, \dots, \alpha_N] \qquad (15)$$

Widodo and Yang [35] proposed the following expression for the weight coefficients $\overline{v_N}$:

$$\overline{v_N} = \begin{bmatrix} 1 & if: \left|\frac{e_i}{\hat{s}}\right| \leq c_1 \\ \dfrac{c_2 - \left|\frac{e_i}{\hat{s}}\right|}{c_2 - c_1} & if: c_1 \leq \left|\frac{e_i}{\hat{s}}\right| \leq c_2 \\ 10^{-1} & otherwise \end{bmatrix} \qquad (16)$$

where $\hat{s}$ is a robust estimate of the standard deviation of the error variable $\left(e_{i = a_i / D_{ii}^{-1}}\right)$. Constants c_1 and c_2 are typically taken as 2.5 and 3, respectively. The term D_{ii}^{-1}refers to the i-th diagonal entry of the inverse matrix *D*, which appears on the left-hand side of Eq. 13. According to Mercer's theorem, the kernel function *K*(.,.) must be selected so that:

$$K(x_i . \overline{x_j}) = \langle \emptyset(x_i), \emptyset(x_j) \rangle_H$$

$$i,j=1,2,\dots,N \qquad (17)$$

as a result, the WLS-SVM formulation is obtained as:

$$y(x) = \sum^{N} \alpha_i K(x_i, x) + b \tag{18}$$

the function $K(x_i . \bar{x_j})$ is essentially an inner product of two vectors in the feature space. To represent it as such, the kernel function $K(x_i . \bar{x_j})$ must be a symmetric, positive-definite function satisfying Mercer's condition. Support Vector Machines (SVMs) typically employ one of three kernel types in practical applications: radial basis function (RBF), polynomial, or linear. Among these, the RBF kernel is the most widely utilized within the WLS-SVM framework, and its formulation is given below [33]:

$$K_{RBF}(x, \bar{x}) = exp(-\frac{\|x - \bar{x}\|^2}{\sigma^2}) \tag{19}$$

here, σ^2 represents a positive constant, typically known as the kernel width. An illustration of the WLS-SVM model's architecture is provided in Fig. 2.

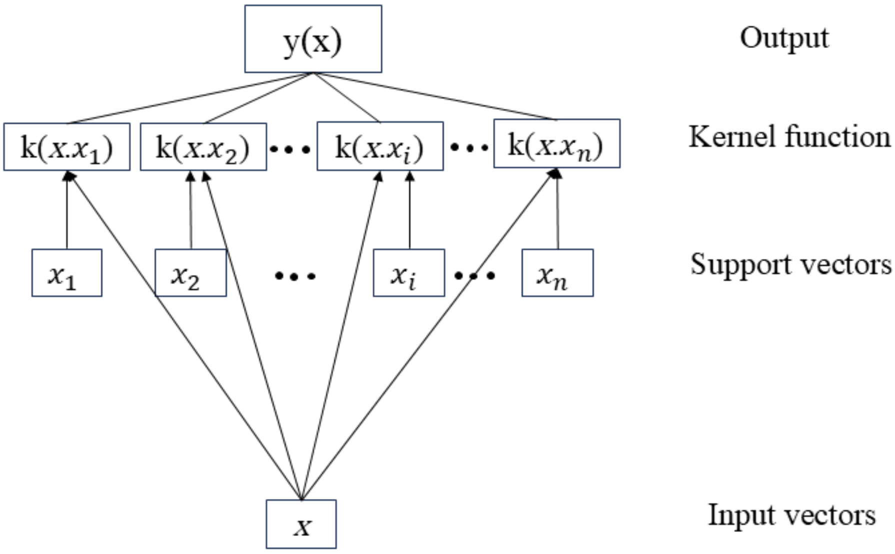

Fig. 2. Structure of the WLS-SVM method.

5. Data processing

To normalize the input and output parameters, Eq. 20 was used. Normalization should be performed prior to applying many data mining methods, such as neural networks, SVM, and K-Means clustering. This process ensures that all input parameters are treated equally by the algorithm and that no single parameter dominates the others due to differences in scale.

$$x_i^n = \frac{x_i - x_{min}}{x_{max} - x_{min}} \tag{20}$$

in this equation, x_i refers to the input data, x_{min} and x_{max} represent the minimum and maximum values of x within the entire dataset, and x_i^n denotes the normalized value.

5.1. Initial parameters

Before initiating the search loop within the predefined parameter domains, six parameters (C, γ_1, γ_2, σ^2, α, and β) must be initially estimated. Proper tuning of these parameters in various SVM-based methods significantly enhances model performance. Table 2 presents the parameter ranges considered in this study [36].

Table 2. Adjust the initial control parameters.

Parameters	Symbol	Upper bound	Lower bound	Ref.
Regularization parameter in the SVM method	C	10^5	10^{-5}	[37]
RBF kernel parameter in SVM method	γ_1	10^5	10^{-5}	[37]
Regularization parameter in the WLS-SVM method	γ_2	10^5	10^{-5}	[37, 38]
RBF kernel parameter in WLS-SVM method	σ^2	10^5	10^{-5}	[37, 38]
Ensemble learning coefficients	(α,β)	0	1	-

5.2. WLS-SVM evaluation using k-fold cross-validation

To develop the prediction model, the data must be divided into training and validation subsets. Although simple splitting techniques exist for this purpose, such approaches are highly sensitive to which data points are selected for training and which for validation. This sensitivity can lead to fluctuations in model accuracy—sometimes overestimating, and at other times underestimating, performance. To overcome this issue and provide a more reliable evaluation of model accuracy, the present study adopts the k-fold cross-validation method, which is widely used in AI research [10]. k-fold cross-validation is one of the most common forms of cross-validation and is extensively applied in machine learning. In this method, the dataset is divided into k equally sized folds, ensuring that both training and validation subsets exhibit similar distributions and adequate variability.

In the present work, a three-fold cross-validation approach was applied, allocating 67% of the dataset for training purposes and the remaining 33% for validation. The dataset was randomly partitioned into three distinct subsets. During each fold, one subset served as the validation set, while the other two were utilized for training. This strategy guarantees that every data sample contributes to both the training and validation phases at least once. Given that $k = 3$ was selected, each model underwent training three separate times throughout the parameter tuning process. As a result, three separate validation error averages are obtained for the objective function. The overall average of these three validation scores provides a reliable indicator of the WLS-SVM model’s general predictive performance.

5.3. Prediction using the WLS-SVM method

At this stage, the WLS-SVM method begins its training process using the initial parameter values (C, γ_1, γ_2, σ^2), and subsequently, the trained model is validated using the validation dataset. It is important to note that data preprocessing is carried out to achieve the highest prediction accuracy.

5.4. Performance metrics

To assess the effectiveness of the WLS-SVM model, multiple statistical metrics were employed, including the correlation coefficient (R), mean absolute percentage error (MAPE), mean absolute error (MAE), and root mean square error (RMSE), and the coefficient of determination (R^2), which quantifies the average error observed during validation. When R and R^2 approach a value of 1, it indicates a higher agreement between predicted and actual outputs. Similarly, lower values of MAPE, MAE, and RMSE indicate higher accuracy in the predictions made by the WLS-SVM method. Eqs. 21-25 present the mathematical formulas for these performance evaluation metrics.

$$MAE = \left(\frac{1}{n}\right) \times \sum_{i=1}^{n} (|p_i - y_i|) \tag{21}$$

$$MAPE = \left(\frac{1}{n}\right) \times \sum_{i=1}^{n} (|p_i - y_i|/y_i) \times 100 \tag{22}$$

$$RMSE = \sqrt{\left[\left(\frac{1}{n}\right) \times \sum_{i=1}^{n} (|p_i - y_i|)^2\right]} \tag{23}$$

$$R^2 = \left(\frac{n\sum y_i \times p_i - (\sum y_i)(\sum p_i)}{\sqrt{(n(\sum y_i^2) - (\sum y_i^2))} \times \sqrt{(n(\sum p_i^2) - (\sum p_i^2))}}\right)^2 \tag{24}$$

$$R = \frac{n\sum y_i \times p_i - (\sum y_i)(\sum p_i)}{\sqrt{(n(\sum y_i^2) - (\sum y_i^2))} \times \sqrt{(n(\sum p_i^2) - (\sum p_i^2))}} \tag{25}$$

where p_i is the predicted value, y_i is the actual value, and n is the sample size. The histograms of the input variables are shown in Fig. 3.

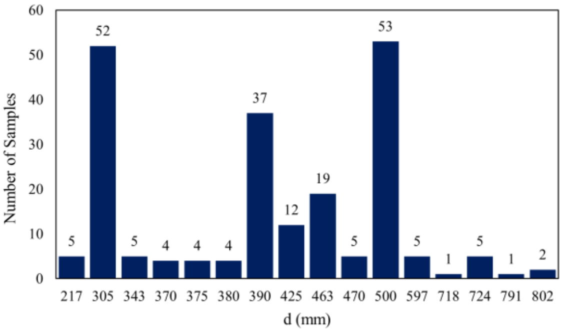

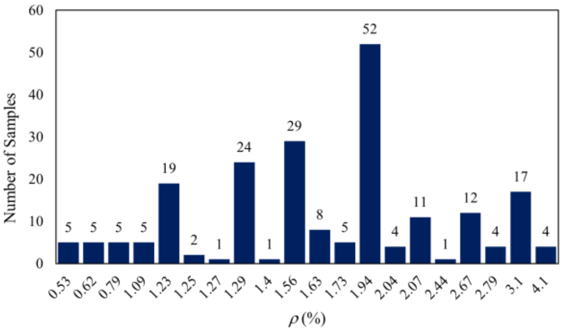

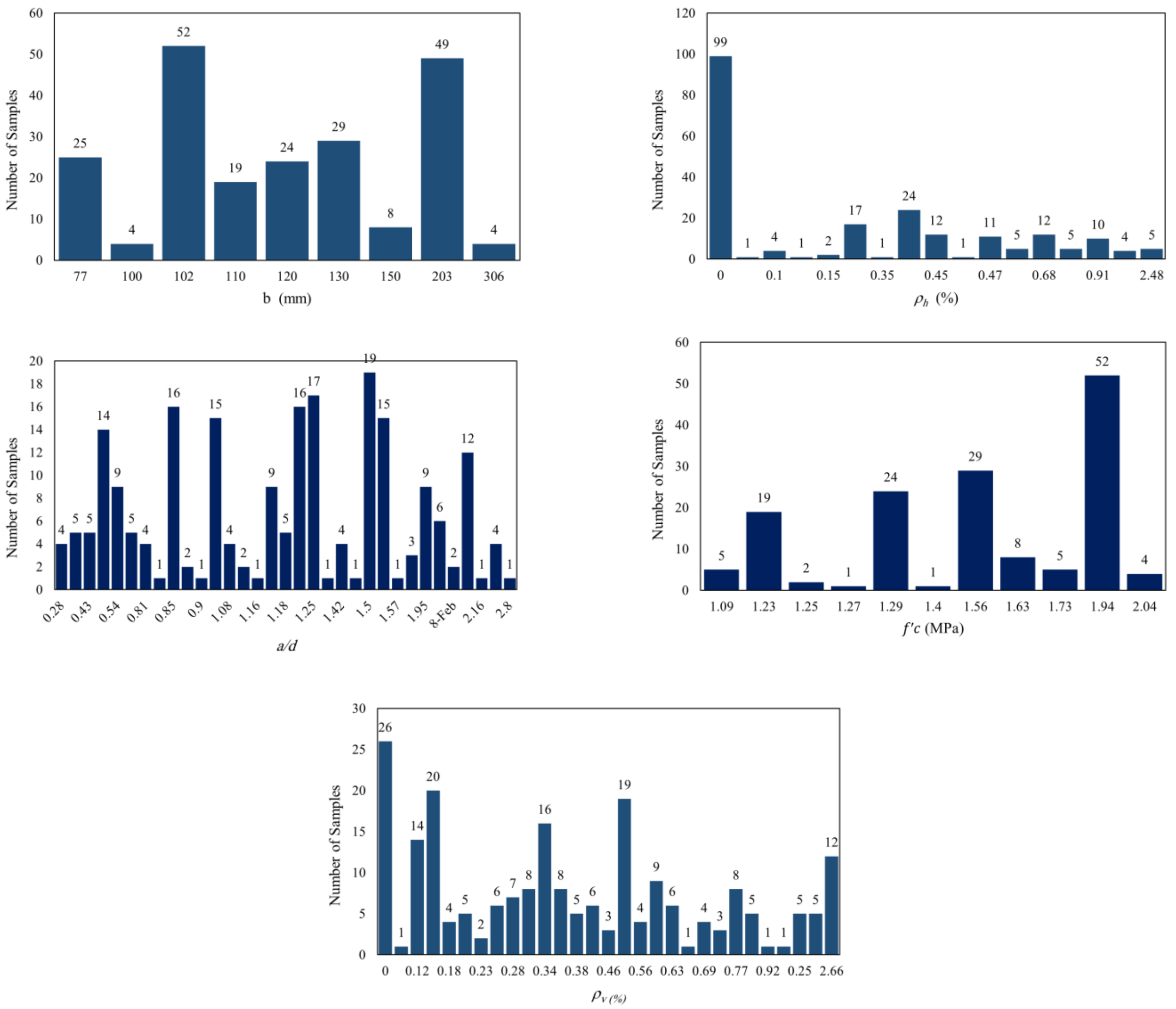

Fig. 3. Histogram of the input variables.

6. Results and discussion

In this work, a three-fold cross-validation strategy ($k = 3$) was applied by randomly splitting the dataset into separate subsets for training and validation purposes. To develop a predictive model for the shear strength of reinforced concrete deep beams using the WLS-SVM method, the data were split into a training set and a validation set. The validation data was used to test the trained and deployed model. In total, using fold cross-validation, 171 randomly selected samples were assigned to the training set and 43 to the validation set. The training set itself was further divided into two internal subsets: one for fitting the model and the other for validating the training performance and fine-tuning the learned model.

6.1. Training phase and parameter selection

Optimal performance of the WLS-SVM technique relies on appropriately selecting the values of the regularization factor γ^2 and the RBF kernel width σ^2. In this study, the best parameter values were identified through a trial-and-error process. Table 3 presents the optimal values of the tuning parameters for WLS-SVM. As shown in Fig. 4, the training results obtained using WLS-SVM with the optimized tuning parameters demonstrate strong model performance. Based on the evaluation metrics (R, R^2, MAE, MAPE, RMSE), the WLS-SVM approach produces values near 1 for R and R^2, and low values for MAE, MAPE, and RMSE, indicating high prediction accuracy. Therefore, the tuned model is ready to predict new test data.

Fig. 5 compares multiple WLS-SVM runs and the statistical outcomes. As shown, the 19th run achieved the lowest MAE, MAPE, and RMSE values, while its R and R^2 values were closest to 1 compared to other runs.

6.2. Validation phase and prediction outcomes

Based on the optimized parameters provided in Table 3 and the trained WLS-SVM model, the predicted outcomes for both training and validation stages are illustrated in Figs. 6a and 6b, respectively. The results indicate that WLS-SVM achieved an R^2 of 0.9279 during training and 0.9804 during validation ($R^2 \geq 0.95$), demonstrating a high level of accuracy in predicting the shear strength of RC deep beams.

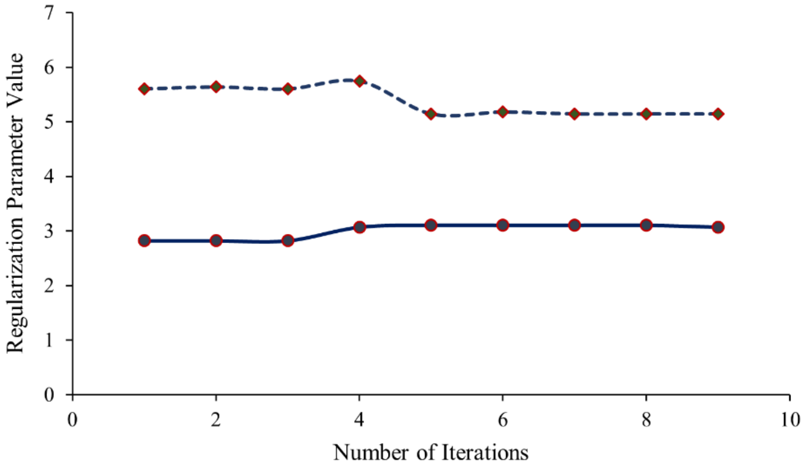

Fig. 4. Parameter tuning procedure and convergence behavior.

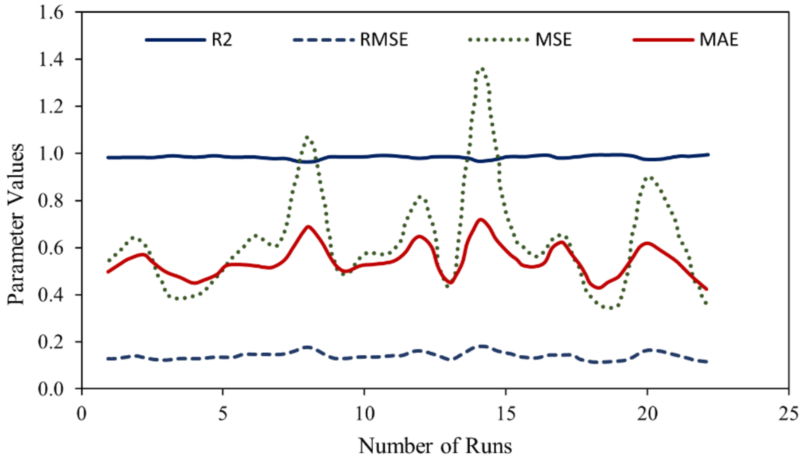

Fig. 5. Comparative analysis of performance metrics (R², MAPE, MAE, RMSE) across multiple runs.

Furthermore, the low MAPE value, which is close to zero, confirms that the predicted shear strength using the WLS-SVM method is reliable. Hence, this method can be considered an effective tool for designing and predicting the shear strength of reinforced concrete deep beams.

Additionally, the statistical results indicate that the proposed WLS-SVM method can minimize discrepancies between training and test performance metrics, thereby avoiding significant prediction issues.

Table 3. Tuned parameter values for the WLS-SVM model during the training stage.

WLS-SVM		
Parameters	γ_2	σ_2
Value Selected in This Study	5.13	3.1037

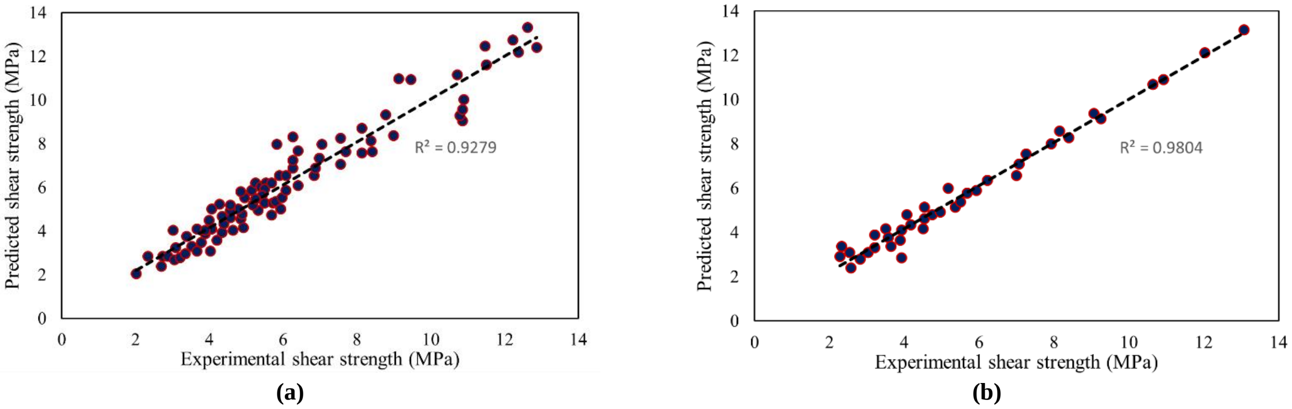

(a) (b)

Fig. 6. Comparison between predicted and experimental shear capacities: (a) Results from the training dataset, (b) Results from the validation dataset.

6.3. Comparison of WLS-SVM with other AI methods

To comprehensively assess the effectiveness of the WLS-SVM model, its results were benchmarked against various alternative AI techniques, which include:

(1) a basic SVM model without parameter adjustment,

(2) LS-SVM without tuning,

(3) SVM optimized using the Symbiotic Organisms Search (SOS) algorithm,

(4) LS-SVM enhanced through SOS,

(5) Tree-based multiple linear regression (MLR-Reg), and

(6) a hybrid SVM–LS-SVM approach applied without parameter calibration [39].

Table 4 presents the average values and standard deviations of performance metrics for each method. The results show that the proposed WLS-SVM method achieved the best values:

RMSE = 0.107, R^2 = 0.9887, MAPE = 9.48, and MAE = 0.478. Furthermore, Table 4 confirms that WLS-SVM outperformed the compared AI methods in terms of accuracy.

Table 5 presents a comparison between the WLS-SVM results, the CSA and ACI code-based predictions, and the results obtained from the Gravitational Search Algorithm (GSA), which is an optimization method based on gravitational laws and mass interactions.

Table 4. Performance comparison between WLS-SVM and other AI-based techniques.

Methods	Results validation					
	R^2	R	MAPE (%)	MAE (MPa)	RMSE (MPa)	Ref.
SVM	0.7598	0.8717	16.51	0.904	1.2167	[39]
LS-SVM	0.8525	0.9271	12.27	0.5669	0.736	[39]
Optimized SVM	0.9189	0.9586	8.26	0.4035	0.5508	[39]
Optimized LS-SVM	0.9189	0.9586	8.09	0.4084	0.5514	[39]
MLR-Reg Tree	0.9285	0.9636	10	0.515	0.6799	[39]
SVM-LSVM	0.8383	0.9156	11.31	0.594	0.7812	[39]
WLS-SVM	0.9804	0.9945	9.48	0.48	0.11	Present study

Table 5. Comparison of WLS-SVM prediction results with those obtained from various design codes and the GSA algorithm.

Methods	$V_{actual}/V_{predicted}$	MAPE	MAE	Ref.
ACI 318-11	0.569	16.19	1.23	[23]
Canadian Standards Association	0.58	18.8	0.91	[24]
General Services Administration	0.15	10.9	0.49	[1]
WLS-SVM	0.998	9.48	0.478	Present study

7. Conclusion

In this study, a novel artificial intelligence method known as Weighted Least Squares Support Vector Machine (WLS-SVM) was employed to predict the shear strength of reinforced concrete deep beams. For this purpose, the relevant shear-influencing parameters were first collected, and a dataset consisting of 214 experimental samples was compiled. The WLS-SVM model was implemented using eight selected input features, and its performance was assessed through evaluation metrics such as R^2, MAEP, RMSE, and MAE.

The results demonstrated that WLS-SVM is a powerful computational tool capable of analyzing complex relationships among various parameters involved in predicting the shear strength of RC deep beams. When compared with alternative AI methods and conventional design standards, the WLS-SVM approach demonstrated superior predictive accuracy, yielding RMSE = 0.107, R^2 = 0.9804, MAEP = 9.48%, and MAE = 0.478. This study confirms that the WLS-SVM method, due to its high predictive performance, can be considered a strong alternative to conventional AI methods and code-based approaches in predicting the shear capacity of RC deep beams. Finally, it can be concluded that WLS-SVM offers the added advantage of being readily implementable in parallel computing architectures, resulting in significantly reduced processing time compared to other techniques while maintaining similar levels of prediction accuracy.

Statements & Declarations

Author contributions

Masoud Mahmoudabadi: Conceptualization, Methodology, Formal analysis, Resources, Writing - Original Draft.

Seyed Mohammad Reza Hasani: Resources, Writing - Original Draft.

Funding

The authors received no financial support for the research, authorship, and/or publication of this article.

Data availability

The data presented in this study will be available on interested request from the corresponding author.

Declarations

The authors declare no conflict of interest.

References

[1] Cakir, F., Acar, V., Aydin, M. R. Experimental and numerical assessment of intraply hybrid composites strengthened RC deep beams. Mechanics of Advanced Materials and Structures, 2025; 1-24. doi:10.1080/15376494.2025.2476208.

[2] Fathalla, E., Mihaylov, B. Shear behaviour of deep beams strengthened with high-strength fiber reinforced concrete jackets. Engineering Structures, 2025; 325: 119404. doi:10.1016/j.engstruct.2024.119404.

[3] Liu, C., Xu, D., Duanmu, X. Analysis of shear strength influencing factors in reinforced concrete deep beams: A modified calculating model. Journal of Building Engineering, 2024; 95: 110243. doi:10.1016/j.jobe.2024.110243.

[4] Tamimi, M. F., Alshannaq, A. A., Abu Qamar, M. a. I. Enhancing reliability in reinforced concrete deep beams through probabilistic analysis and topology optimized strut-and-tie models. Structures, 2024; 70: 107872. doi:10.1016/j.istruc.2024.107872.

[5] Prayoonwet, W., Koshimizu, R., Ozaki, M., Sato, Y., Jirawattanasomkul, T., Yodsudjai, W. Shear strength prediction for RC beams without shear reinforcement by neural network incorporated with mechanical interpretations. Engineering Structures, 2024; 298: 117065. doi:10.1016/j.engstruct.2023.117065.

[6] AlHamaydeh, M., Markou, G., Bakas, N., Papadrakakis, M. AI-based shear capacity of FRP-reinforced concrete deep beams without stirrups. Engineering Structures, 2022; 264: 114441. doi:10.1016/j.engstruct.2022.114441.

[7] Zhang, G., Ali, Z. H., Aldlemy, M. S., Mussa, M. H., Salih, S. Q., Hameed, M. M., Al-Khafaji, Z. S., Yaseen, Z. M. Reinforced concrete deep beam shear strength capacity modelling using an integrative bio-inspired algorithm with an artificial intelligence model. Engineering with Computers, 2022; 38: 15-28. doi:10.1007/s00366-020-01137-1.

[8] Baghdadi, A., Babovic, N., Kloft, H. Fuzzy Logic, Neural Network, and Adaptive Neuro-Fuzzy Inference System in Delegation of Standard Concrete Beam Calculations. Buildings, 2023; 14: 15. doi:10.3390/buildings14010015.

[9] Feng, D.-C., Wang, W.-J., Mangalathu, S., Hu, G., Wu, T. Implementing ensemble learning methods to predict the shear strength of RC deep beams with/without web reinforcements. Engineering Structures, 2021; 235: 111979. doi:10.1016/j.engstruct.2021.111979.

[10] Chou, J.-S., Pham, A.-D. Enhanced artificial intelligence for ensemble approach to predicting high performance concrete compressive strength. Construction and Building Materials, 2013; 49: 554-563. doi:10.1016/j.conbuildmat.2013.08.078.

[11] Kaloop, M. R., Roy, B., Chaurasia, K., Kim, S.-M., Jang, H.-M., Hu, J.-W., Abdelwahed, B. S. Shear strength estimation of reinforced concrete deep beams using a novel hybrid metaheuristic optimized SVR models. Sustainability, 2022; 14: 5238. doi:10.3390/su14095238.

[12] Vapnik, V. N. The Nature of Statistical Learning Theory. 2nd ed. New York (NY): Springer International Publishing; 1999. doi:10.1007/978-1-4757-3264-1.

[13] Megahed, K. Prediction and reliability analysis of shear strength of RC deep beams. Scientific Reports, 2024; 14: 14590. doi:10.1038/s41598-024-64386-w.

[14] Chen, R., Zhang, P., Wu, H., Wang, Z., Zhong, Z. Prediction of shield tunneling-induced ground settlement using machine learning techniques. Frontiers of Structural and Civil Engineering, 2019; 13: 1363-1378. doi:10.1007/s11709-019-0561-3.

[15] Liu, Z., Wu, D., Liu, Y., Han, Z., Lun, L., Gao, J., Jin, G., Cao, G. Accuracy analyses and model comparison of machine learning adopted in building energy consumption prediction. Energy Exploration & Exploitation, 2019; 37: 1426-1451. doi:10.1177/0144598718822400.

[16] Acar, E., Rais-Rohani, M. Ensemble of metamodels with optimized weight factors. Structural and Multidisciplinary Optimization, 2009; 37: 279-294. doi:10.1007/s00158-008-0230-y.

[17] Chou, J.-S., Yang, K.-H., Lin, J.-Y. Peak shear strength of discrete fiber-reinforced soils computed by machine learning and metaensemble methods. Journal of Computing in Civil Engineering, 2016; 30: 04016036. doi:10.1061/(ASCE)CP.1943-5487.0000595.

[18] Hoang, N.-D., Tran, X.-L., Nguyen, H. Predicting ultimate bond strength of corroded reinforcement and surrounding concrete using a metaheuristic optimized least squares support vector regression model. Neural Computing and Applications, 2020; 32: 7289-7309. doi:10.1007/s00521-019-04258-x.

[19] Luo, H., Paal, S. G. Metaheuristic least squares support vector machine-based lateral strength modelling of reinforced concrete columns subjected to earthquake loads. Structures, 2021; 33: 748-758. doi:10.1016/j.istruc.2021.04.048.

[20] Gharehbaghi, S., Yazdani, H., Khatibinia, M. Estimating inelastic seismic response of reinforced concrete frame structures using a wavelet support vector machine and an artificial neural network. Neural Computing and Applications, 2020; 32: 2975-2988. doi:10.1007/s00521-019-04075-2.

[21] Luo, H., Paal, S. G. A novel outlier-insensitive local support vector machine for robust data-driven forecasting in engineering. Engineering with Computers, 2023; 39: 3671-3689. doi:10.1007/s00366-022-01781-9.

[22] Prayogo, D., Cheng, M.-Y., Wu, Y.-W., Tran, D.-H. Combining machine learning models via adaptive ensemble weighting for prediction of shear capacity of reinforced-concrete deep beams. Engineering with Computers, 2020; 36: 1135-1153. doi:10.1007/s00366-019-00753-w.

[23] American Concrete Institute (ACI). ACI 318-25: Building Code for Structural Concrete—Code Requirements and Commentary. Farmington Hills (MI): ACI; 2025.

[24] Canadian Standards Association (CSA). CSA A23.3:19: Design of Concrete Structures. Longueuil (QC): CSA; 2019.

[25] Clark, A. P. Diagonal Tension in Reinforced Concrete Beams. ACI Journal Proceedings, 1951; 48: 145-156. doi:10.14359/11876.

[26] Kong, F.-K., Robins, P. J., Cole, D. F. Web Reinforcement Effects on Deep Beams. ACI Journal Proceedings, 1970; 67: 1010-1018. doi:10.14359/7336.

[27] Smith, K. N., Vantsiotis, A. S. Shear Strength of Deep Beams. ACI Journal Proceedings, 1982; 79: 201-213.

[28] Anderson, N. S., Ramirez, J. A. Detailing of Stirrup Reinforcement. ACI Structural Journal, 1989; 86: 507-515. doi:10.14359/3005.

[29] Tan, K.-H., Kong, F.-K., Teng, S., Guan, L. High-Strength Concrete Deep Beams With Effective Span and Shear Span Variations. ACI Structural Journal, 1995; 92: 395-405. doi:10.14359/991.

[30] Oh, J.-K., Shin, S.-W. Shear Strength of Reinforced High-Strength Concrete Deep Beams. ACI Structural Journal, 2001; 98: 164-173. doi:10.14359/10184.

[31] Aguilar, G., Matamoros, A. B., Parra-Montesinos, G. J., Ramírez, J. A., Wight, J. K. Experimental Evaluation of Design Procedures for Shear Strength of Deep Reinforced Concrete Beams. ACI Structural Journal, 2002; 99: 539-548. doi:10.14359/12123.

[32] Quintero-Febres, C. G., Parra-Montesinos, G., Wight, J. K. Strength of Struts in Deep Concrete Members Designed Using Strut-and-Tie Method. ACI Structural Journal, 2006; 103: 577-586. doi:10.14359/16434.

[33] Suykens, J. A. K., De Brabanter, J., Lukas, L., Vandewalle, J. Weighted least squares support vector machines: robustness and sparse approximation. Neurocomputing, 2002; 48: 85-105. doi:10.1016/S0925-2312(01)00644-0.

[34] Li, H.-s., Lü, Z.-z., Yue, Z.-f. Support vector machine for structural reliability analysis. Applied Mathematics and Mechanics, 2006; 27: 1295-1303. doi:10.1007/s10483-006-1001-z.

[35] Widodo, A., Yang, B.-S. Wavelet support vector machine for induction machine fault diagnosis based on transient current signal. Expert Systems with Applications, 2008; 35: 307-316. doi:10.1016/j.eswa.2007.06.018.

[36] Faris, H., Hassonah, M. A., Al-Zoubi, A. M., Mirjalili, S., Aljarah, I. A multi-verse optimizer approach for feature selection and optimizing SVM parameters based on a robust system architecture. Neural Computing and Applications, 2018; 30: 2355-2369. doi:10.1007/s00521-016-2818-2.

[37] Hoang, N.-D., Pham, A.-D. Hybrid artificial intelligence approach based on metaheuristic and machine learning for slope stability assessment: A multinational data analysis. Expert Systems with Applications, 2016; 46: 60-68. doi:10.1016/j.eswa.2015.10.020.

[38] Cheng, M.-Y., Prayogo, D., Wu, Y.-W. Prediction of permanent deformation in asphalt pavements using a novel symbiotic organisms search–least squares support vector regression. Neural Computing and Applications, 2019; 31: 6261-6273. doi:10.1007/s00521-018-3426-0.

[39] Prayogo, H. Prediction of Concrete Compressive Strength from Early Age Test Result Using an Advanced Metaheuristic-Based Machine Learning Technique. In: Proceedings of the 34th International Symposium on Automation and Robotics in Construction (ISARC); 2017 July 1-3; Taipei, Taiwan. p. 856-863. doi:10.22260/ISARC2017/0120.

Civil Engineering and Applied Solutions, 2026; 2(1): 12–21

Civil Engineering and Applied Solutions

Research Article

journal homepage: ceas.journals.umz.ac.ir

CEAS Civil Engineering and Applied Solutions

Balancing Cost and Seismic Performance: Rectangular vs. T-shaped Shear Walls in Steel Frame Tall Buildings

Mehran Rahimi [a], Khosrow Bargi [a*], Moein Rezapour [a]

[a] *School of Civil Engineering, College of Engineering, University of Tehran, Tehran, Iran*

ARTICLE INFO

Keywords:
Tall building
T-shaped shear wall
Seismic behavior
Dual system
Structural efficiency

Article history:
Received 19 September 2025
Accepted 01 October 2025
Available online 01 January 2026

ABSTRACT

The economic importance of tall buildings makes the selection of lateral load-resisting systems a critical challenge, as these systems must also be cost-effective. One widely adopted option for such structures is the steel moment frame combined with reinforced concrete shear walls. In many tall buildings around the world, reinforced concrete shear walls are recognized as an efficient lateral system. Improving the performance of these structures through the optimal placement of shear walls in the building plan can result in significant cost savings. A common practice is to modify conventional rectangular shear walls into T, L, or I-shaped configurations. Due to their three-dimensional efficiency, T-shaped shear walls can provide seismic resistance in both principal directions of a building. In this study, an economic comparison was conducted between rectangular and T-shaped reinforced concrete shear walls in steel-frame tall buildings. The results showed that T-shaped shear walls are economically superior to rectangular ones, as they require less material while achieving smaller deformations. Moreover, T-shaped walls do not impose significant architectural or construction challenges, as their geometry facilitates the integration of functional elements such as elevator shafts.

1. Introduction

Rapid urbanization, population growth, and economic demands have driven the construction of tall buildings worldwide [1-3]. Designing these structures requires balancing safety, performance, and cost-effectiveness [4, 5]. Selecting efficient lateral load-resisting systems is crucial to control wind and seismic forces while minimizing construction and maintenance costs [6, 7]. Dual systems combining steel moment frames and reinforced concrete shear walls are widely used. Steel frames offer high strength-to-weight ratios and ductility, while concrete shear walls provide significant lateral stiffness, controlling displacements and enhancing stability [8, 9]. Hybrid frame–shear wall systems leverage both advantages, enabling resilient and economical designs for buildings typically ranging from 20 to 60 stories [10-12]. Shear wall layout critically affects structural performance. Transforming conventional rectangular walls into T, L, or I-shaped configurations improves lateral and torsional stiffness. T-shaped walls, in particular, exhibit superior three-dimensional performance, reduce lateral displacements, and allow for more economical designs by better force distribution and reduced steel requirements [13, 14].

In recent years, significant attention has been paid to the seismic behavior of T-shaped shear walls. Lefas et al. tested thirty full-scale walls under combined axial and lateral loads, examining the effects of parameters such as height-to-width ratio, axial load, concrete strength, and horizontal reinforcement. Their results indicated that wall strength largely depends on concrete in compression zones, while these zones enhance load-carrying capacity [15, 16]. Thompsen and Wallace observed that when the wall flange is under compression, the ductility is significantly higher, whereas tensioned flanges exhibit a more brittle behavior [17]. Brueggen's tests on two steel–concrete composite walls showed lower displacement capacity in T-shaped walls compared to rectangular or symmetrically flanged walls, emphasizing careful free-edge design [18]. Pin-Le and Qing-ning identified the web

---

* Corresponding author.
E-mail addresses: kbargi@ut.ac.ir (K. Bargi).

https://doi.org/10.22080/ceas.2025.30091.1043

How to cite this article: Rahimi, M., Bargi, K., Rezapour, M. Balancing Cost and Seismic Performance: Rectangular vs. T-shaped Shear Walls in Steel Frame Tall Buildings. Civil Engineering and Applied Solutions. 2026; 2(1): 12–21. doi:10.22080/ceas.2025.30091.1043.

region as the main weak point, with failures resulting from concrete crushing and steel yielding under cyclic loading [19]. Lu and Yang reported flexural failures at the free-edge web of narrow steel–concrete walls and emphasized the need for adequate confinement under increasing axial loads [20]. Ji et al. compared Chinese and American design codes, revealing that GB 50011-2010 underestimates boundary element lengths without flanges, potentially causing premature failure [21]. Lan et al. demonstrated that T-shaped composite walls perform well under 45° angled loading; while higher axial loads increase strength, they limit ductility [22]. Building on the findings of the aforementioned studies, more recent research has focused on innovative arrangements and complex loading patterns. Brueggen et al. suggested that uniform distribution of longitudinal reinforcement across the flange, rather than concentrating it in boundary elements, reduces shear lag, crack width, and overall damage in T-shaped reinforced concrete walls under multiaxial loading [23].

Recent advances have emphasized the crucial role of shear wall configuration in the seismic performance of tall buildings. Rahimi and Bargi [24] performed a comparative study on tall buildings with rectangular and T-shaped reinforced concrete shear walls within dual systems. Their results indicated that optimal performance occurs when shear walls are placed in intermediate frames, as this configuration minimizes displacements in both principal directions and achieves a more balanced stiffness distribution. Furthermore, T-shaped walls consistently outperformed rectangular walls in both linear and nonlinear analyses, exhibiting reduced roof displacements and inter-story drifts. This improvement was attributed to the higher moment of inertia of T-shaped walls in the plan layout, which provides greater stiffness and seismic resilience. These findings suggest that T-shaped shear walls can offer a more efficient lateral load-resisting system in high seismic zones, motivating further investigations into their application and potential optimization in tall building design.

In the present study, an economic comparison was conducted between rectangular and T-shaped reinforced concrete shear walls in steel frame tall buildings with 10, 20, and 30 story heights. The analysis was performed for two seismic zones with design base acceleration ratios of A = 0.35 and A = 0.5 to evaluate the effect of varying seismic hazard on the selection and optimization of lateral load-resisting systems. Buildings with 10, 20, and 30 stories represent typical tall structures in the country. The inclusion of A = 0.5 alongside A = 0.35 is motivated by the presence of areas that are located near active faults and thus experience higher seismic risk. Moreover, the critical importance of tall buildings necessitates a more detailed assessment under severe seismic conditions.

2. Methodology

2.1. Geometrical properties of buildings

Figs. 1 to 3 illustrate the three-dimensional view and floor plan of the 10, 20, and 30-story buildings. Each building consists of five bays with a span length of 6 m in both longitudinal and transverse directions. The height of all buildings is 3.5 m. The structural modeling was carried out in three dimensions.

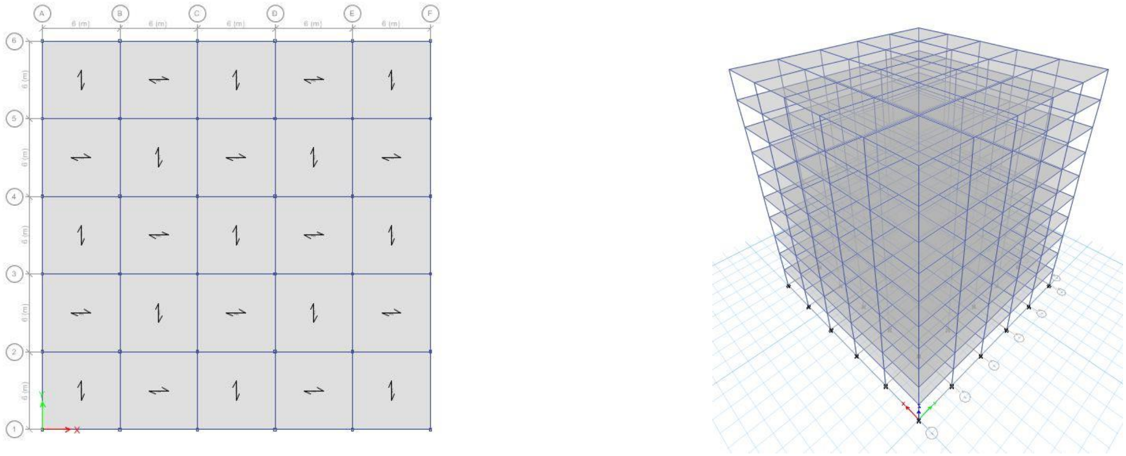

Fig. 1. Three-dimensional view and floor plan of the 10-story building frame.

2.2. Assumptions and modeling details

Three-dimensional modeling and response spectrum dynamic analysis serve as powerful tools for predicting the seismic performance of structures and comparing different design alternatives. In this study, the modeling and design of the buildings were carried out using ETABS v16. The response spectrum dynamic analysis was also conducted using the same software to evaluate the structural behavior under the earthquake response spectrum. By incorporating both the seismic characteristics of each region and the structural properties, this analysis enables the estimation of maximum displacements, forces, and shear demands, thereby providing a basis for the economic and performance comparison of the two shear wall systems. In addition to the use of software, a set of modeling assumptions and code-based standards was considered. These assumptions included the selection of material behavior, connection modeling, bracing conditions, and detailing of walls and frames. Furthermore, economic and performance indicators such as structural weight, steel and concrete consumption, lateral stiffness, inter-story drift, and base shear were employed for comparison and evaluation.

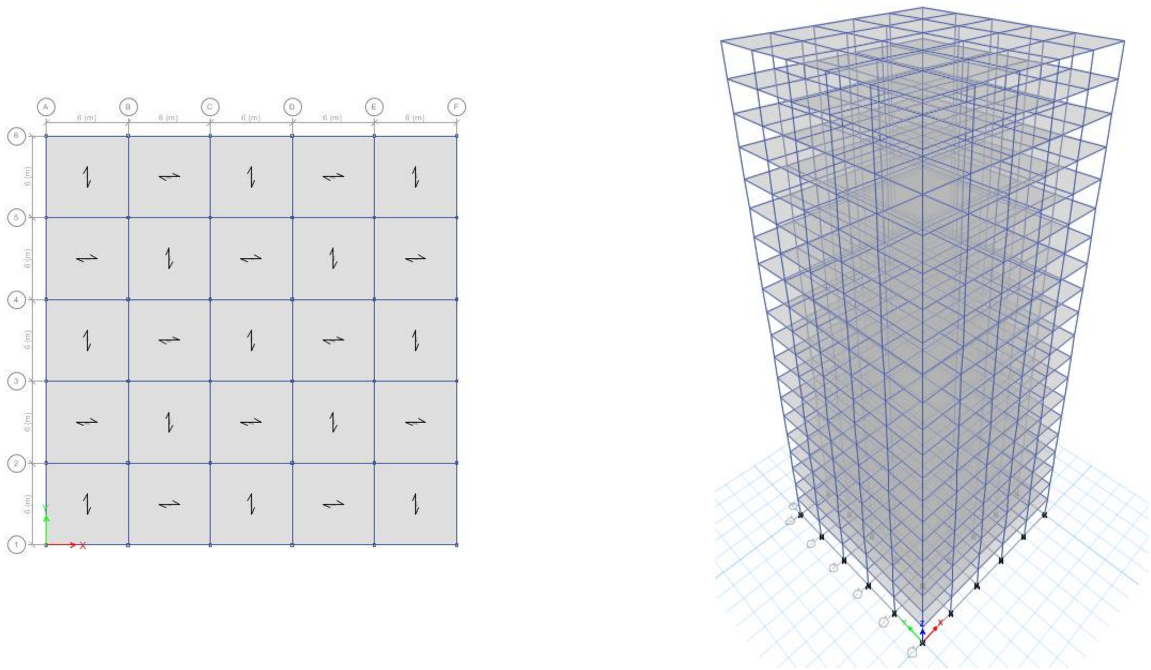

Fig. 2. Three-dimensional view and floor plan of the 20-story building frame.

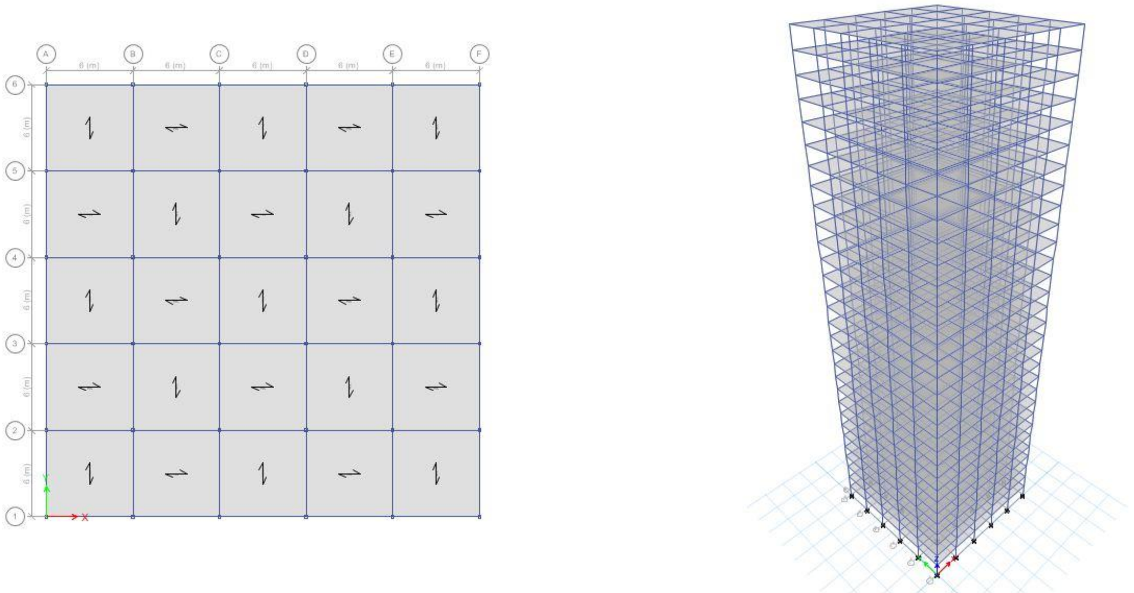

Fig. 3. Three-dimensional view and floor plan of the 30-story building frame.

This comprehensive approach allows for an accurate and scientific assessment of the advantages and limitations of each shear wall type and can serve as a guideline for selecting an optimal lateral load-resisting system in the design of tall buildings.

2.3. Loading conditions

The gravity loads considered for the 10-, 20-, and 30-story buildings are summarized in Table 1.

Table 1. Gravity loads for typical floors and roofs.

Floor type	Dead load (kg/m²)	Live load (kg/m²)	Partition load (kg/m²)	Perimeter wall load (kg/m)
Typical floor	500	200	100	600
Roof	500	150	-	300

The lateral load-resisting system of the 10 and 20-story buildings was designed as a dual system consisting of intermediate steel moment-resisting frames (IMRFs) combined with special reinforced concrete shear walls (S-RCWs). For the 30-story building, the system was designed as a dual system with special steel moment-resisting frames (SMRFs) and special reinforced concrete shear walls (S-RCWs). In all cases, the moment-resisting frames were designed to resist at least 25% of the total seismic base shear, as required by code provisions. Seismic analysis was performed using the response spectrum method based on the Iranian Seismic Code (Standard 2800, 4th edition), ensuring that the dynamic base shear was not less than the corresponding equivalent static base shear. The buildings were assumed to have residential occupancy. The beams of the steel frames were modeled as I-shaped rolled sections, while the columns were modeled as box sections. Structural steel was assumed to be ST37 with a yield strength of 2400 kg/cm² and ultimate strength of 3700 kg/cm². The compressive strength of concrete in the shear walls was taken as 25 MPa, and the reinforcement was modeled using AIII-grade steel. P–Delta effects were also incorporated in the analysis. The following codes and standards were used for loading, linear analysis, checking, and design of the studied structures:

1. Iranian National Building Code, Part 6: Loads (2019 edition)
2. Iranian Seismic Code, Standard No. 2800, 4th edition
3. ACI 318-19: Building Code Requirements for Structural Concrete
4. AISC 360-16: Specification for Structural Steel Buildings
5. Consideration of wall cracking effects in shear wall design

3. Results and discussion

3.1. Placement of rectangular and T-shaped shear walls in the plan

The placement of rectangular and T-shaped shear walls in the 10, 20, and 30-story buildings is illustrated in Figs. 4 to 6. In a recent study by Rahimi and Bargi [24], which was also mentioned in the introduction, various arrangements of both rectangular and T-shaped shear walls were selected based on practical considerations and common structural design practices to cover a wide range of possible placements within the building plan. These arrangements included locations near the perimeter, at the center, and within intermediate frames, allowing for a comprehensive evaluation of the influence of wall placement on the seismic response of the structure. The results revealed that the optimal configuration for both rectangular and T-shaped shear walls in steel frames occurred when the walls were positioned in intermediate frames, rather than being close to the center or placed at the farthest distance from it. The primary criterion for identifying the optimal configurations was minimizing roof displacement, as this parameter directly reflects the overall lateral stiffness and seismic performance of the structure. After performing linear response spectrum analyses for all configurations, the two arrangements with the lowest roof displacements were identified as optimal and subsequently subjected to nonlinear time-history analyses for further evaluation. In both linear dynamic spectrum and nonlinear time-history analyses, the intermediate placement was confirmed as the most effective configuration. In the present study, the economic comparison of rectangular and T-shaped shear walls is conducted based on the optimal configuration identified in the referenced work.

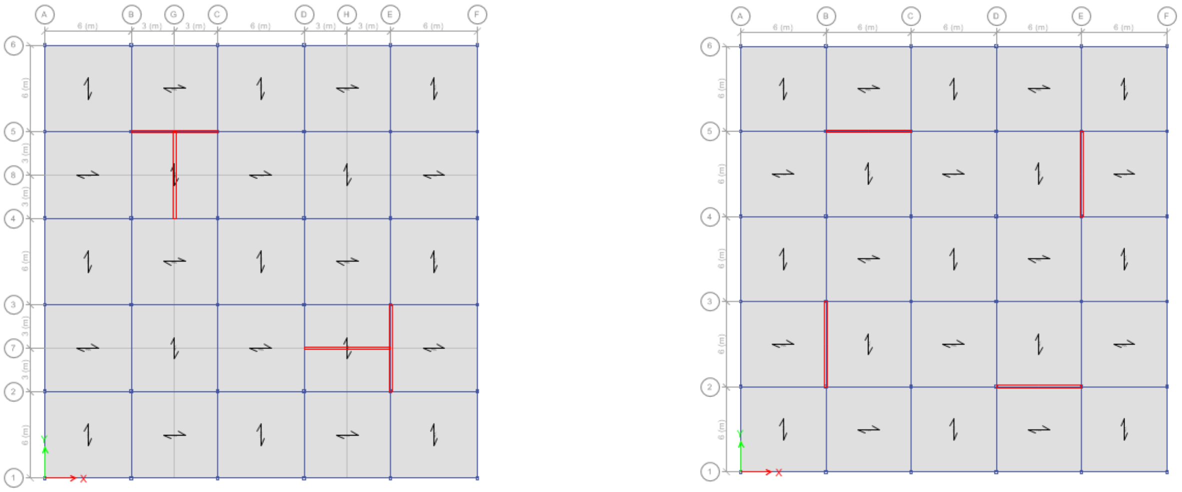

Fig. 4. Placement of rectangular and T-shaped shear walls in the plan of a 10-story building.

3.2. Economic comparison

In this section, an economic comparison between rectangular and T-shaped shear walls in tall buildings is presented. For this purpose, steel buildings with heights of 10, 20, and 30 stories were analyzed and designed in ETABS v16, considering two cases of rectangular and T-shaped shear walls with equal wall areas in plan. Since the wall areas in plan are identical, the amount of consumed concrete is the same in both cases, thereby minimizing the influence of wall geometry on the total concrete volume in the economic comparison. The concrete weight for the designed buildings in both seismic zones, with design base acceleration ratios of $A = 0.35$ and $A = 0.5$, is 525 tons for the 10-story building, 2,450 tons for the 20-story building, and 5,040 tons for the 30-story building. The steel frames in both seismic zones were designed in accordance with the AISC 360-16 provisions. For the selection of beam and column sections, 50 different beam profiles and 50 different column profiles were considered, enabling the automatic design of the steel frame in ETABS.

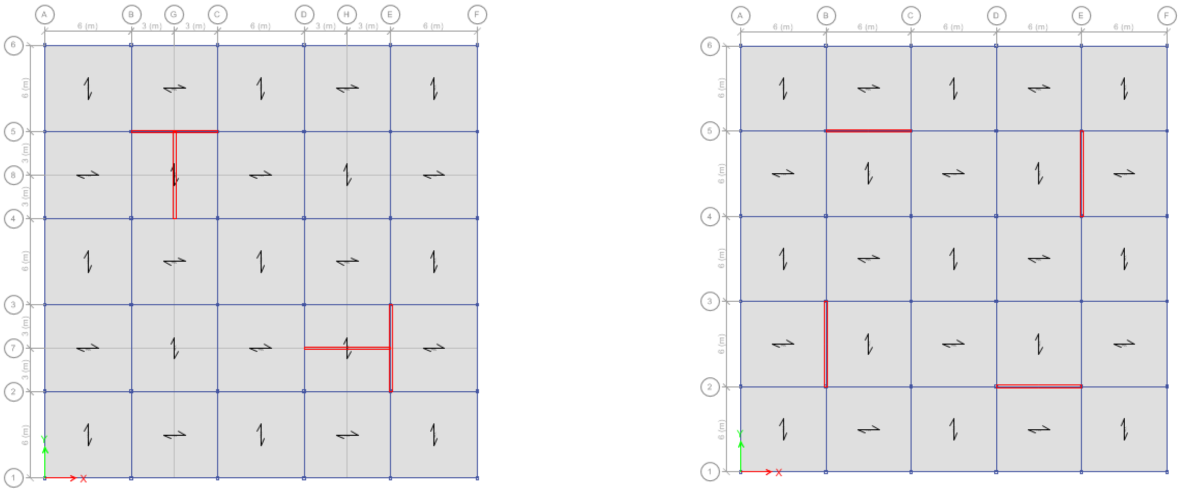

Fig. 5. Placement of rectangular and T-shaped shear walls in the plan of a 20-story building.

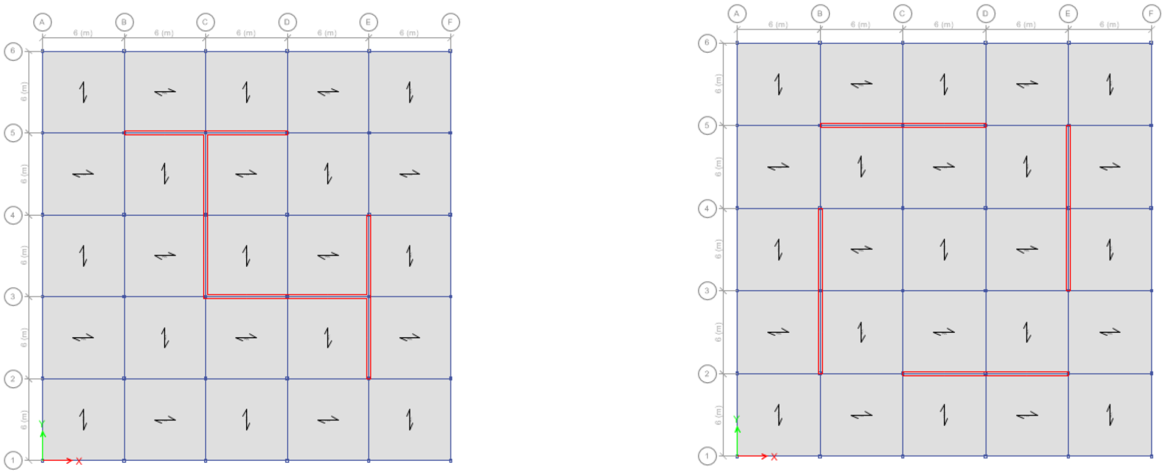

Fig. 6. Placement of rectangular and T-shaped shear walls in the plan of a 30-story building.

This methodology ensures that the most efficient combination of sections is selected for each building height, based on both seismic performance and economic criteria. In addition, the adequacy of the designed members was verified using a MATLAB code, confirming that the ratio of the applied stresses to the member capacities remained within the acceptable range, specifically not less than 0.95. Figs. 7 and 8 present the steel weight used in the design of the frames for the 10, 20, and 30-story buildings. These figures illustrate the economic differences in steel usage between rectangular and T-shaped shear wall systems and provide the basis for the economic analysis of the project.

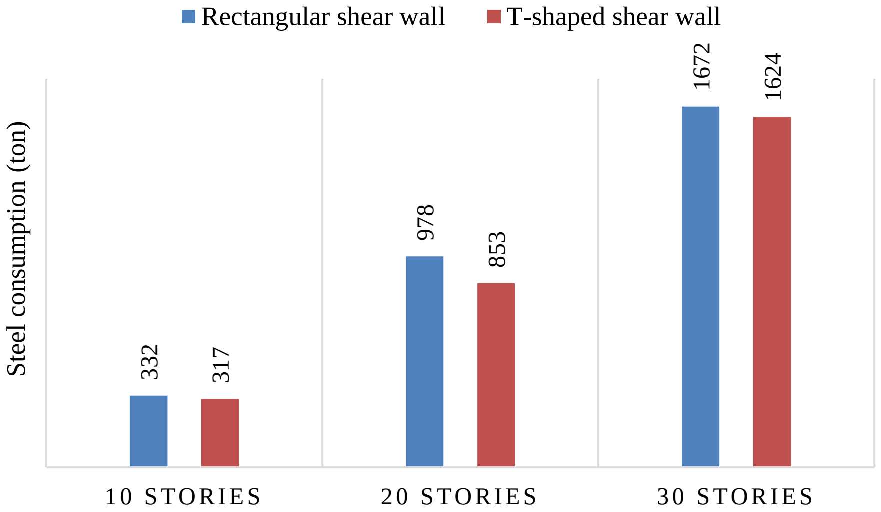

Fig. 7. Steel consumption in frame design for the seismic zone with a design base acceleration ratio of *A* = 0.35.

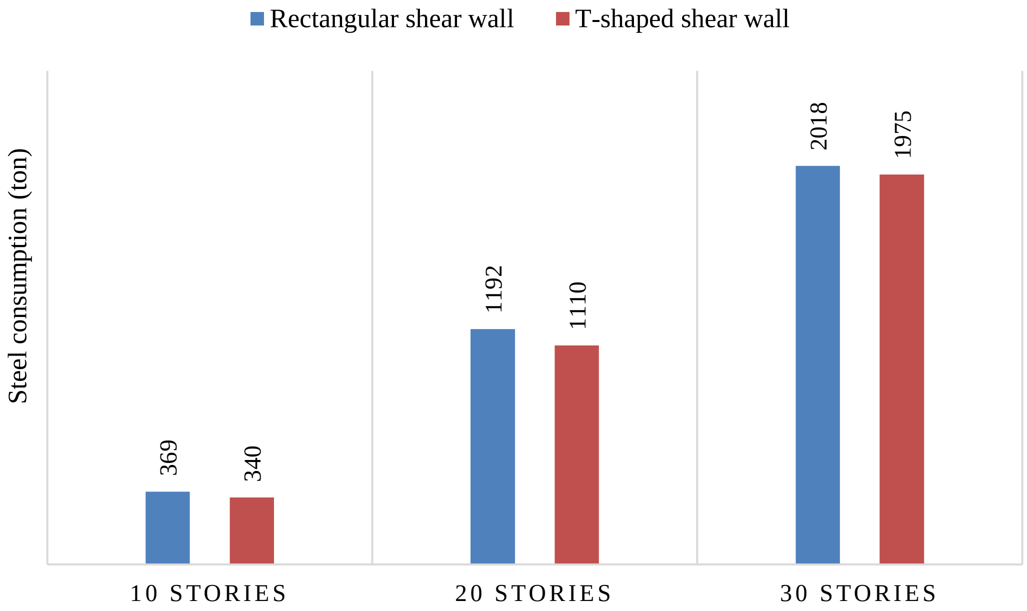

Fig. 8. Steel consumption in frame design for the seismic zone with a design base acceleration ratio of *A* = 0.5.

Furthermore, in Figs. 9 to 14, the roof displacements of the designed buildings in the two seismic zones with design base acceleration ratios of *A* = 0.35 and *A* = 0.5 are compared for both rectangular and T-shaped shear walls. This comparison enables the assessment of seismic behavior and lateral stiffness of the structures and demonstrates that the shear wall geometry has a direct effect on reducing or increasing roof displacements.

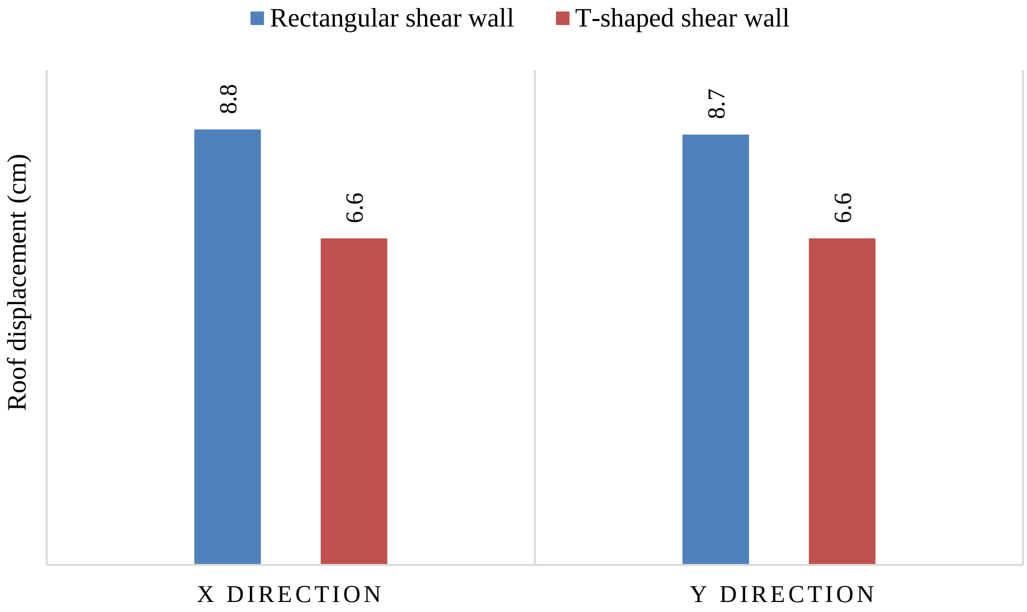

Fig. 9. Roof displacement of 10-story buildings designed with rectangular and T-shaped shear walls in the seismic zone with a design base acceleration ratio of *A* = 0.35.

As observed, frames with T-shaped shear walls not only exhibit smaller displacements in both X and Y directions compared to rectangular walls, but also require less steel for beams and columns. This is because the stiffness of a shear wall is related to its moment of inertia in plan, and the moment of inertia of a composite wall, such as a T-shaped wall, is higher than that of a rectangular wall. By converting rectangular shear walls into a T-shaped configuration, the resulting composite section has an increased moment of inertia, which leads to greater stiffness and reduces the forces transmitted to the frame. Consequently, the member forces in the frame decrease, allowing for smaller cross-sections and ultimately lower material consumption. This trend is consistent across the 10-, 20-, and 30-story buildings in both seismic zones with design base acceleration ratios of *A* = 0.35 and *A* = 0.5.

The results of this section provide valuable guidance for the optimal selection of lateral load-resisting systems in tall building design and highlight their significant role in achieving an efficient balance between structural performance and material economy, particularly regarding the use of concrete and steel sections.

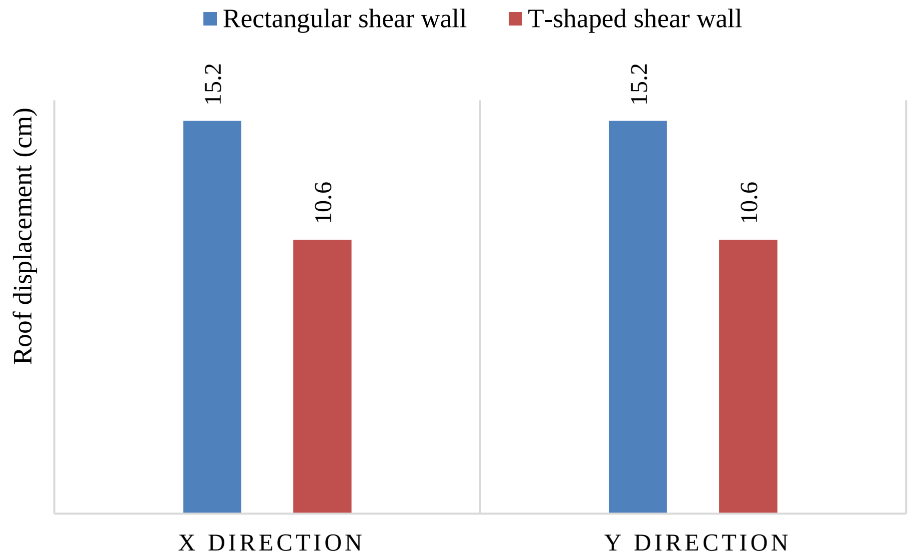

Fig. 10. Roof displacement of 20-story buildings designed with rectangular and T-shaped shear walls in the seismic zone with a design base acceleration ratio of *A* = 0.35.

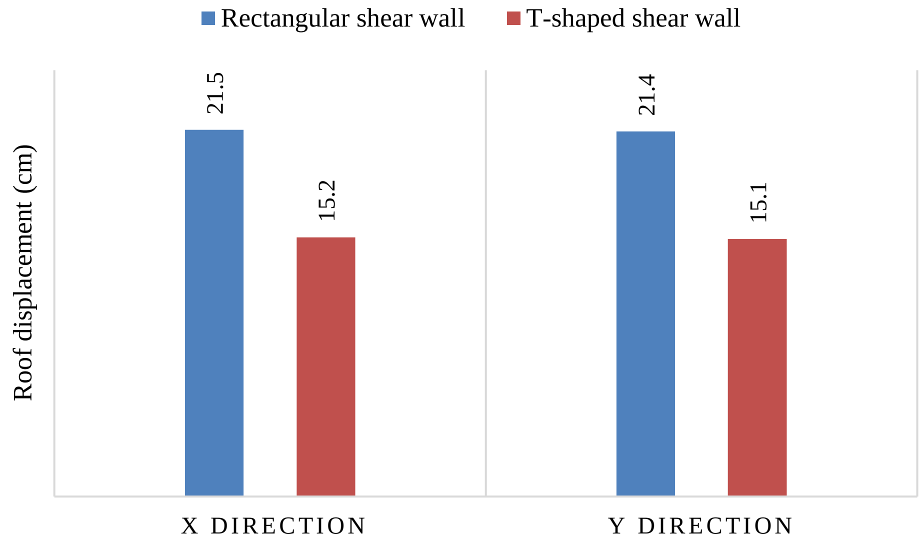

Fig. 11. Roof displacement of 30-story buildings designed with rectangular and T-shaped shear walls in the seismic zone with a design base acceleration ratio of *A* = 0.35.

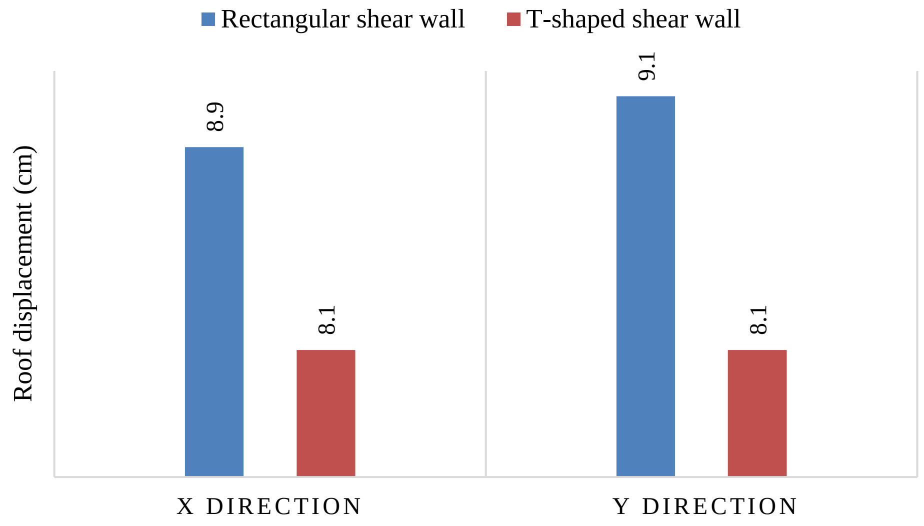

Fig. 12. Roof displacement of 10-story buildings designed with rectangular and T-shaped shear walls in the seismic zone with a design base acceleration ratio of *A* = 0.5.

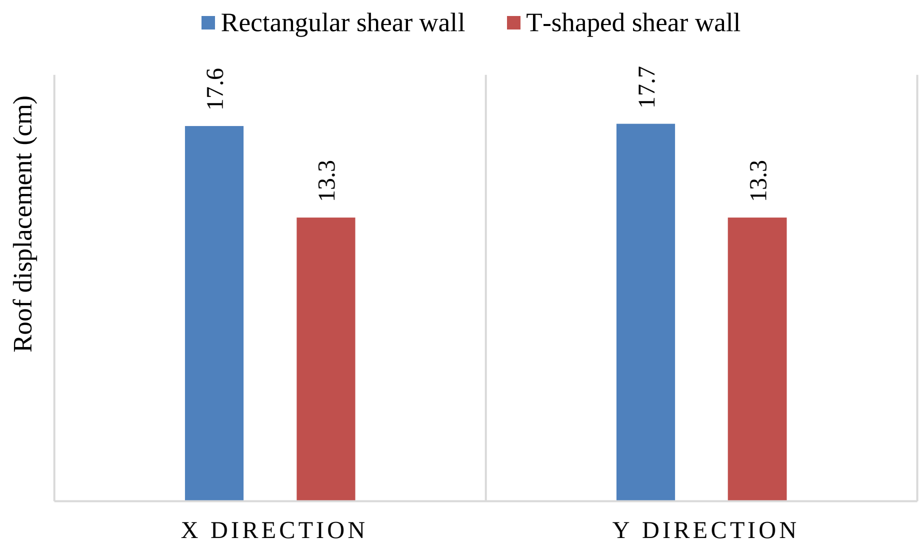

Fig. 13. Roof displacement of 20-story buildings designed with rectangular and T-shaped shear walls in the seismic zone with a design base acceleration ratio of *A* = 0.5.

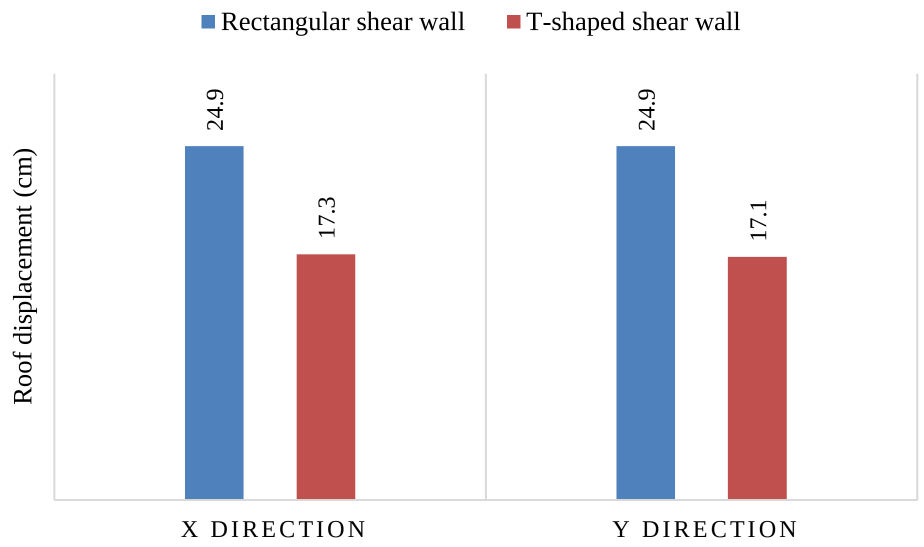

Fig. 14. Roof displacement of 30-story buildings designed with rectangular and T-shaped shear walls in the seismic zone with a design base acceleration ratio of *A* = 0.5.

4. Conclusion

In this study, an economic comparison was conducted between rectangular and T-shaped reinforced concrete shear walls in steel-frame tall buildings. The main findings are as follows:

1. As observed, in all studied buildings, frames with T-shaped shear walls not only exhibited lower roof displacements compared to rectangular walls but also required less steel for beams and columns. This is because the lateral stiffness of a shear wall is related to its moment of inertia in plan, and a T-shaped wall has a higher moment of inertia than a rectangular one. Consequently, greater stiffness results in lower forces transmitted to the frame, leading to smaller member sections and reduced material consumption. These results were consistent across all building heights and seismic zones considered.
2. T-shaped shear walls provide both superior seismic and economic performance without significant architectural or construction challenges, as their geometry allows easy accommodation of architectural elements such as elevator shafts.
3. A hybrid layout combining T-shaped and rectangular shear walls can offer a promising strategy to balance cost and structural performance. While T-shaped walls provide higher stiffness and seismic resistance, rectangular walls are generally simpler and more economical to construct. By strategically combining these wall types based on location and performance requirements, designers can optimize both economic efficiency and seismic performance in tall buildings.

Statements & Declarations

Author contributions

Mehran Rahimi: Investigation, Formal analysis, Validation, Resources, Writing - Original Draft, Writing - Review & Editing.

Khosrow Bargi: Conceptualization, Methodology, Project administration, Supervision, Writing - Review & Editing.

Moein Rezapour: Investigation,Writing - Review & Editing.

Funding

The authors received no financial support for the research, authorship, and/or publication of this article.

Data availability

The data presented in this study will be available on interested request from the corresponding author.

Declarations

The authors declare no conflict of interest.

References

[1] Rahimi, M., Davoodi, M.-R., Nematzadeh, M., Yousefpour, H. The effect of type of mechanical anchors on bond behavior of ribbed-surface GFRP bars embedded in concrete. Journal of Building Engineering, 2024; 82: 108307. doi:10.1016/j.jobe.2023.108307.

[2] Rahimi, M., Davoodi, M.-R., Nematzadeh, M., Yousefpour, H. Bond performance of GFRP bars with mechanical steel anchors using RILEM beam bond tests: Experimental and theoretical study. Engineering Structures, 2024; 304: 117615. doi:10.1016/j.engstruct.2024.117615.

[3] Das, A., Konar, T. Asymmetric nonlinear compliant deep tank dampers-inerter for mitigating response of tall buildings under near-fault ground motions. Structures, 2025; 76: 108970. doi:10.1016/j.istruc.2025.108970.

[4] Rahimi, M., Davoodi, M.-R., Nematzadeh, M., Yousefpour, H., Azarbera, M., Fattahi, Z. A comparative study between beam and pull-out tests on bond behavior of ribbed GFRP bar in concrete conforming to RILEM standards. Archives of Civil and Mechanical Engineering, 2024; 25: doi:10.1007/s43452-024-01095-1.

[5] Elnimeiri, M. M., Hwang, Y. Towards Sustainable Structure of Tall Buildings by Significantly Reducing the Embodied Carbon. Sustainability, 2025; 17: 2754. doi:10.3390/su17062754.

[6] Razavi, M., Rahimi, M., Tichi, A. H., Nematzadeh, M. Synergistic effects of recycled nylon granules and bacterial nano-cellulose in lightweight concrete: Experiments and predictions. Construction and Building Materials, 2025; 493: 143124. doi:10.1016/j.conbuildmat.2025.143124.

[7] Emad, S., Aboulnaga, M., Wanas, A., Abouaiana, A. The Role of Artificial Intelligence in Developing the Tall Buildings of Tomorrow. Buildings (2075-5309), 2025; 15: doi:10.3390/buildings15050749.

[8] Kamarudin, M. A. A., Ahmad, S. W., Alsakkaf, H. A., Mustopha, S. I. S., Shafiq, O. The Assessment of Tall Building Structure Performance Due to Seismic Effect in Malaysia. Journal of Advanced Research Design, 2025; 129: 112-129. doi:10.37934/ard.129.1.112129.

[9] Rezapour, M., Ghassemieh, M. Macroscopic modelling of coupled concrete shear wall. Engineering Structures, 2018; 169: 37-54. doi:10.1016/j.engstruct.2018.04.088.

[10] Tiwari, N. D., Sarkar, P. P. Prediction of dynamic loads and responses of a tall building in tornado wind: Numerical analysis and experimental validation. Engineering Structures, 2025; 326: 119510. doi:10.1016/j.engstruct.2024.119510.

[11] Khorasani, M., Mostofinejad, D., Muciaccia, G., Kheyroddin, A. Enhancing RC shear wall performance against shear failure modes using fiber-reinforced polymer (FRP) composites: A comprehensive review. In: Structures; 2025; p. 108162. doi:10.1016/j.istruc.2024.108162.

[12] Rezapour, M., Ghassemieh, M. Macroscopic Modelling of the Concrete Shearwall with Asymmetrical Openings. Modares Civil Engineering journal, 2023; 23: 35-49. doi:10.22034/23.5.4.

[13] Wang, J., Cao, S., Tim, K., Li, S., Fung, J. C., Li, Y. A novel life-cycle analysis framework to assess the performances of tall buildings considering the climate change. Engineering Structures, 2025; 323: 119258. doi:10.1016/j.engstruct.2024.119258.

[14] Sun, P., Nie, P., Liang, K., Wang, D. The performance analysis of shear walls with opening based on quantitative identification method of vibration modes. Alexandria Engineering Journal, 2025; 120: 637-647. doi:10.1016/j.aej.2025.02.074.

[15] Lefas, I., Kotsovos, M. NLFE analysis of RC structural walls and design implications. Journal of Structural Engineering, 1990; 116: 146-164. doi:10.1061/(ASCE)0733-9445(1990)116:1(146).

[16] Lefas, I. D., Kotsovos, M. D., Ambraseys, N. N. Behavior of reinforced concrete structural walls: strength, deformation characteristics, and failure mechanism. ACI Structural Journal, 1990; 87: 23-31. doi:10.14359/2911.

[17] Thomsen IV, J. H., Wallace, J. W. Displacement-based design of slender reinforced concrete structural walls—experimental verification. Journal of Structural Engineering, 2004; 130: 618-630. doi:10.1061/(ASCE)0733-9445(2004)130:4(618).

[18] Brueggen, B. L. Performance of T-shaped reinforced concrete structural walls under multi-directional loading, (PhD Thesis). Minneapolis (MN): University of Minnesota; 2009.

[19] Pin-Le, Z., Qing-ning, L. Cyclic loading test of T-shaped mid-rise shear wall. The structural design of tall and special buildings, 2013; 22: 759-769. doi:10.1002/tal.723.

[20] Lu, X., Yang, J. Seismic behavior of T-shaped steel reinforced concrete shear walls in tall buildings under cyclic loading. The structural design of tall and special buildings, 2015; 24: 141-157. doi:10.1002/tal.1158.

[21] Ji, X., Liu, D., Qian, J. Improved design of special boundary elements for T-shaped reinforced concrete walls. Earthquake Engineering and Engineering Vibration, 2017; 16: 83-95. doi:10.1007/s11803-017-0370-4.

[22] Lan, W., Zhang, Z., Li, B. Seismic performance of T-shaped steel-concrete composite structural walls subjected to loadings from different directions. Journal of Constructional Steel Research, 2017; 128: 7-18. doi:10.1016/j.jcsr.2016.08.007.

[23] Brueggen, B. L., French, C. E., Sritharan, S. T-shaped RC structural walls subjected to multidirectional loading: test results and design recommendations. Journal of Structural Engineering, 2017; 143: 04017040. doi:10.1061/(ASCE)ST.1943-541X.0001719.

[24] Rahimi, M., Bargi, K. Comparative Evaluation of Seismic Behavior of T-Shaped versus Rectangular Concrete Shear Walls in High-Rise Buildings. Civil Engineering and Applied Solutions, 2025; 1: 16-26. doi:10.22080/ceas.2025.29715.1029.

Civil Engineering and Applied Solutions, 2026; 2(1): 22-32

Civil Engineering and Applied Solutions

Research Article

journal homepage: ceas.journals.umz.ac.ir

Determination of Moment Parameters of Rectangular Stress Block for High-Strength Prestressed Concrete

Shahram Maghsodian [a*]

[a] *Department of Civil Engineering, Islamic Azad University, Nour Branch, Nour, Iran*

ARTICLE INFO

Keywords:
Stress block
Structural design
Compressed concrete
High-strength concrete
Prediction

Article history:
Received 28 August 2025
Accepted 04 October 2025
Available online 01 January 2026

ABSTRACT

Various structural design codes for reinforced and prestressed concrete propose different equations and recommendations for the parameters of the rectangular stress block. However, these formulations are often valid only for a specific ultimate strain and are primarily based on concrete with a compressive strength below 50 MPa. In this study, with the aim of evaluating the accuracy and adequacy of these parameters for high-strength prestressed concrete, the stress-strain curve and equivalent stress block parameters were calculated throughout the entire loading process. To achieve this, a simplified third-degree polynomial stress-strain relationship was proposed and compared with experimental data for both compressed (high-strength) and non-compressed (normal-strength) concretes. The results demonstrated that the proposed model has acceptable accuracy in predicting the actual behavior of both compressed and non-compressed concretes, and it can be used to derive instantaneous parameters of the stress block. The obtained stress block parameters were compared with code-based relationships and previous studies, revealing that certain code assumptions require modification when applied to high-strength concrete.

Nomenclature

A_s: Area of steel under tension
b: Section width
C: Compressive force
c: Depth of neutral axis
d: Effective depth of the concrete section
F_s: Area under the stress–strain curve
f'_c: Compressive strength of concrete
f_y: Yield stress of steel
k: $\frac{\varepsilon_c}{\varepsilon_0}$
T: Tensile stress in the reinforcement
α_1, β_1: Parameters of the rectangular stress block
ε_c: Strain in concrete
ε_0: Strain at peak stress
ε_{cu}: Ultimate strain of concrete
ε_s: Steel strain
σ_c: Stress in concrete
RC: Reference concrete
CC: Compressed concrete

1. Introduction

The assumption of linear strain distribution across the depth of a flexural section leads to a compressive stress profile that resembles the uniaxial stress–strain curve of concrete. However, this curve is influenced by numerous variables, making it impractical to propose a universal stress–strain model for concrete. In reinforced concrete design, the stress distribution area and its centroid are more critical for equilibrium equations than the precise geometry of the stress profile [1-6]. Consequently, the rectangular stress block is preferred for its computational simplicity in evaluating area, centroid, and related parameters. The

---

* Corresponding author.
E-mail addresses: s_maghsodian@iaunour.ac.ir (S. Maghsodian).

https://doi.org/10.22080/ceas.2025.29949.1040

How to cite this article: Maghsodian, S. Determination of Moment Parameters of Rectangular Stress Block for High-Strength Prestressed Concrete. Civil Engineering and Applied Solutions. 2026; 2(1): 22–32. doi:10.22080/ceas.2025.29949.1040.

rectangular stress block concept, originally introduced by Whitney [7], has been widely adopted in design codes, typically calibrated for a specific maximum strain. For instance, ACI 318 [8] defines parameter $\varepsilon_{cu} = 0.003$ to represent conventional concrete strength. Whitney proposed a rectangular stress block as an alternative to the allowable stress design theory and validated it using experimental data. In his model, the width of the stress block was defined by 0.85 f'_c, while its depth varied with the reinforcement ratio of the beam. Mattock et al. [9] introduced parameters for the rectangular stress block currently used in the ALBDS code for concrete compressive strengths below 10 ksi. Their findings indicated that the stress block width remains constant at 0.85 for all compressive strengths, while the depth equals 0.85 for strengths below 4 ksi and decreases with increasing strength, but not below 0.65. Li [10] reported that the actual compressive stress distribution in high-strength concrete (HSC) resembles a triangular shape, with peak stress occurring at a strain of approximately 0.003. Conservatively, he assumed the peak stress in the triangular stress block for HSC to be f'_c, and derived equivalent rectangular block parameters $\alpha_1 = 0.75$ and $\beta_1 = 0.67$ accordingly. Oztekin et al. [11] developed a new stress–strain model for high-performance concrete (HPC) based on experimental curves, and proposed equivalent rectangular stress block parameters consistent with their model. These parameters showed good agreement with those derived from experimental stress–strain data. Ozbakkaloglu and Saatcioglu [12] introduced a new rectangular stress block applicable to a wide range of concrete strengths (20–130 MPa), and validated their model against experimental data with high accuracy. Mertol et al. [13] investigated the stress–strain behavior and stress block parameters for HSC, concluding that parameter α_1 in the ALBDS formulation requires revision for high-strength concrete, while parameters β_1 and the ultimate strain remain valid. Ho and Peng [14] proposed a strain-gradient-dependent equivalent rectangular stress block for reinforced concrete members, and based on this, developed a new flexural strength design method for normal-strength concrete (NSC) columns that incorporates strain gradient effects. Van Zijl and Mbewe [15] presented models for predicting the flexural capacity of steel fiber-reinforced concrete (SFRC) beams, with and without conventional steel reinforcement, using equivalent rectangular stress blocks for both tensile and compressive zones. Their models demonstrated satisfactory agreement with existing models and experimental results. Prachasaree et al. [16] derived stress–strain relationships, equivalent stress block parameters, and flexural strength predictions for fly ash-based geopolymer concrete members. Their proposed parameters showed good correlation with experimental data, while the nominal strength calculated using standard code parameters was approximately 1.43 times higher than that obtained using their proposed design parameters. In this study, the stress block parameters at any strain level and at ultimate strain are determined using a proposed stress–strain relationship. The parameters proposed by other researchers and design codes are also reviewed and evaluated.

The stress block is a cornerstone concept in reinforced and prestressed concrete design, forming the basis for calculating flexural strength, ductility, and safety margins in structural members. While several design codes provide equations for rectangular stress block parameters, these formulations are generally limited to concretes with compressive strengths below 50 MPa and are tied to specific assumptions about ultimate strain. With the increasing use of high-strength concrete in modern infrastructure driven by the demand for slender, efficient, and sustainable structures, there is a pressing need to re-examine the adequacy of code-based stress block parameters for this class of materials. Previous studies and existing code provisions have not sufficiently captured the nonlinear behavior of high-strength concrete under compression, especially throughout the entire loading process. This gap may lead to over-conservative or unsafe design outcomes when conventional parameters are directly applied to high-strength concrete. The present study addresses this limitation by proposing a simplified third-degree polynomial stress–strain model, which is validated against experimental results for both high-strength and normal-strength concretes. Unlike traditional formulations, the proposed approach allows the derivation of instantaneous stress block parameters, enabling a more accurate representation of the actual material response. By systematically comparing the obtained stress block parameters with those prescribed in international codes and prior research, this work highlights critical discrepancies and identifies areas where code assumptions require modification. The findings not only provide a more reliable foundation for the design of high-strength concrete structures but also contribute to the long-term evolution of design standards. Ultimately, the study bridges the gap between empirical code provisions and the actual behavior of concrete across a broader strength range, thereby advancing both structural safety and efficiency in modern engineering practice.

2. Determination of stress block parameters

The actual stress distribution of concrete in the compression zone of reinforced concrete members subjected to flexure is illustrated in Fig.1. For design simplification, an equivalent rectangular stress block, also depicted in Fig. 1, is adopted. This block is defined by two parameters: α_1 and β_1 The parameter α_1 represents the ratio of the average compressive stress in the equivalent block under flexure to the cylindrical compressive strength (f'_c) or cube strength (f_{cu}) of concrete. The parameter β_1 denotes the ratio of the depth of the equivalent rectangular compressive stress block to the distance from the extreme compression fiber to the neutral axis (c). This simplified stress block model has been endorsed by various design codes, which define the parameters α_1 and β_1 as functions of concrete strength alone, facilitating its application in ultimate limit state design.

In the present study, to obtain the parameters of the equivalent rectangular stress block, an easily integrable stress-strain relation for concrete is required. For this purpose, a third-degree polynomial that satisfies the four boundary conditions mentioned in the previous section is proposed based on Eq. 1.

$$y = mx + (3-2m)x^2 + (m-2)x^3$$
$$x = \frac{\varepsilon_c}{\varepsilon_0}, y = \frac{\sigma_c}{f'_c}, m = \frac{\varepsilon_0}{f'_c} \times \left(\frac{d\sigma_c}{d\varepsilon_c}\right)_{\varepsilon_c=0}, \tag{1}$$

To evaluate the accuracy of the proposed stress–strain relationship, the model curves were compared with experimental results.

Figs. 2 and 3 illustrate the comparison between the proposed model and experimental data for unconfined and confined concrete specimens, respectively.

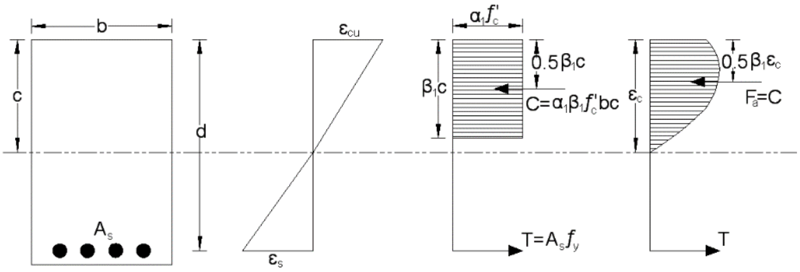

Fig. 1. Experimental and equivalent stress blocks and linear strain distribution [17].

A total of 60 experimental data points related to the research provided by Nematzadeh and Naghipour [18] were used in this study. In the nomenclature for identifying experimental specimens, the first letter represents the type of the specimen (R represents the reference concrete (uncompressed concrete), S represents the compressed concrete. The first number represents the value of the target compressive strength of the corresponding uncompressed concrete in MPa. The letter P, along with the second number in the compressed concretes, demonstrates the primary lateral pressure (expressed in terms of lateral strain) which is going to be applied to the fresh concrete in microstrain, while the two letters NP in the reference concretes indicate the lack of pressure; however, the preceding number is used to distinguish it from other reference concretes. As evident from the figures, the proposed model demonstrates strong agreement with the experimental data. Therefore, it can be reliably employed for determining the parameters of the equivalent rectangular stress block.

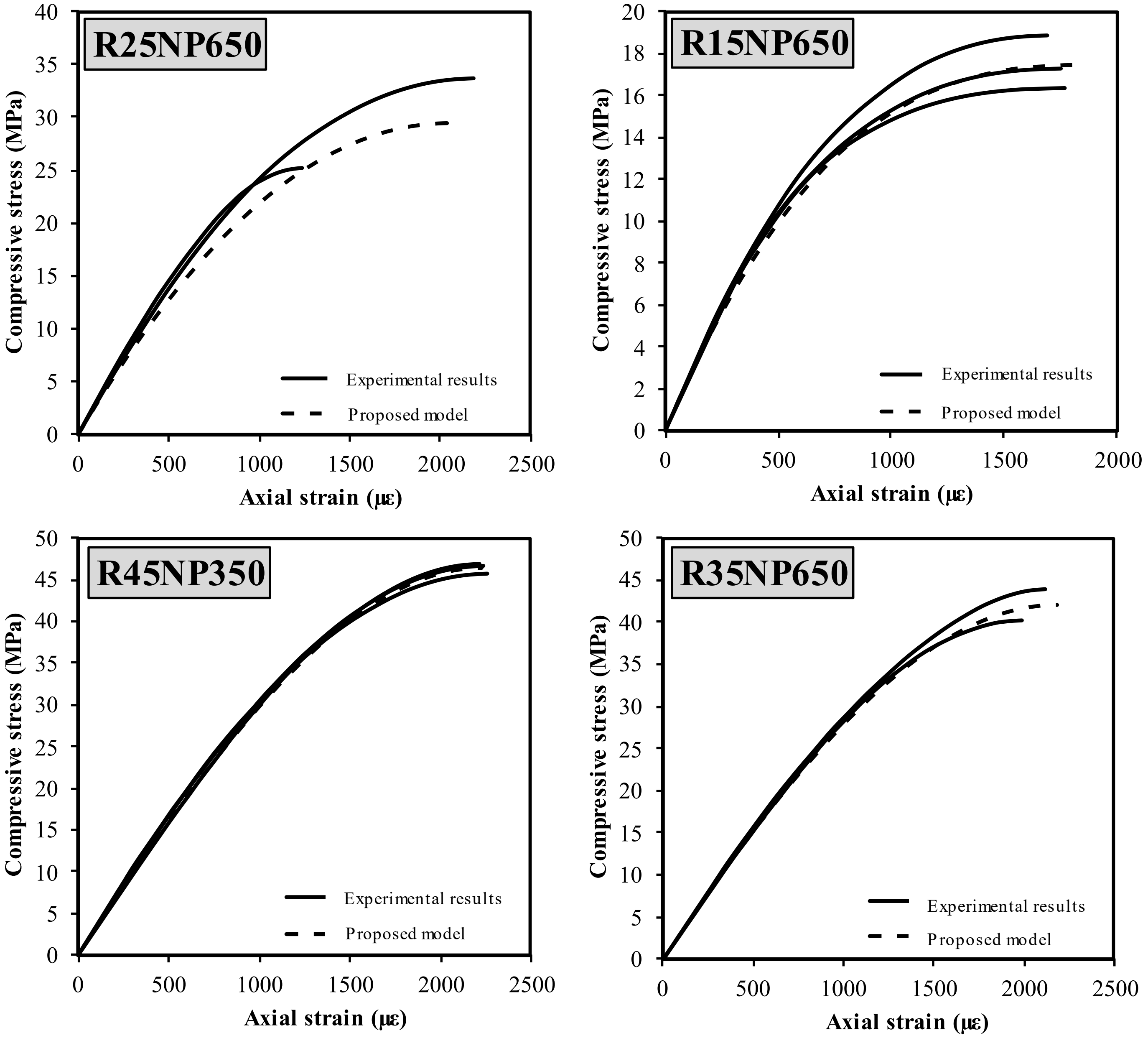

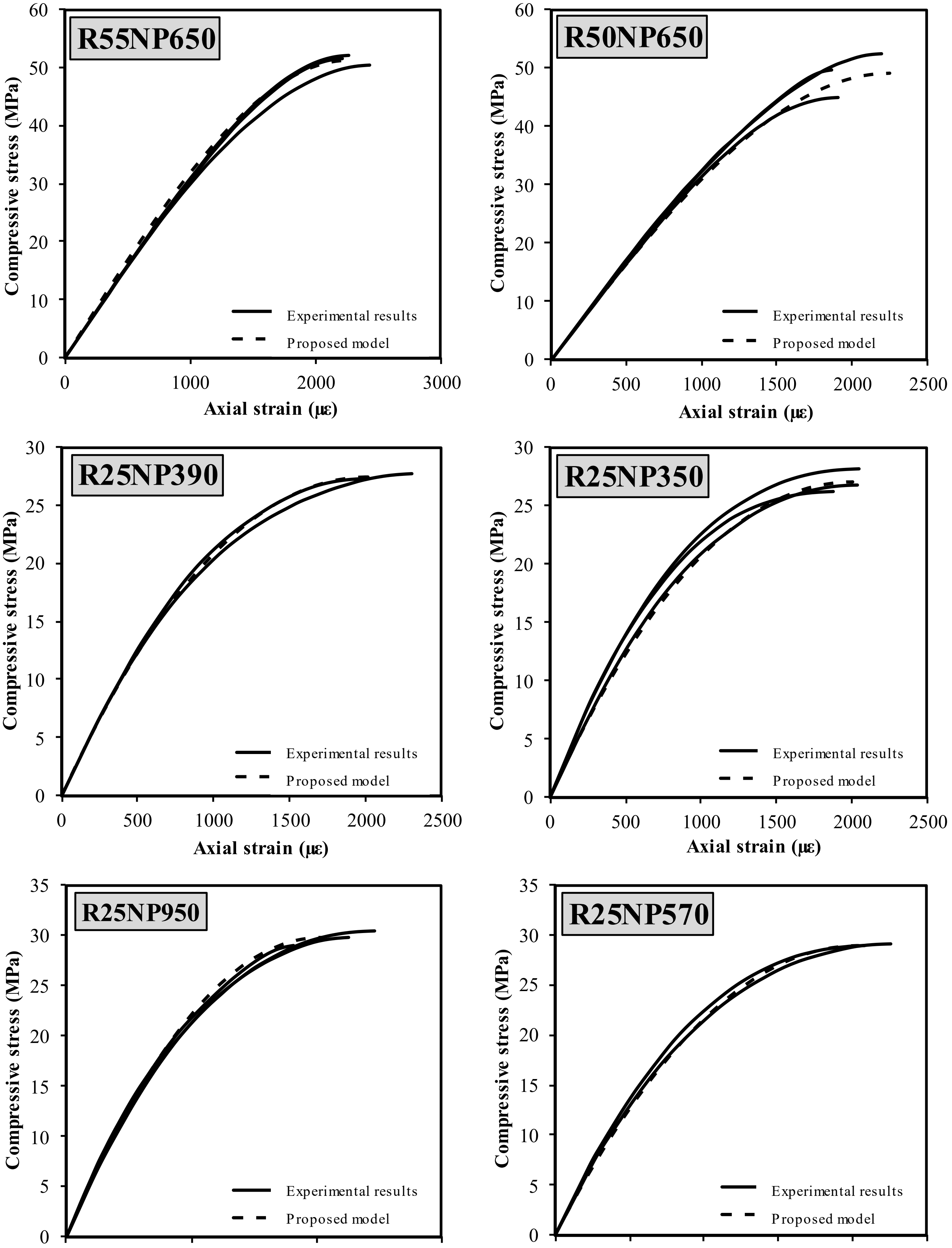

Fig. 2. Experimental stress-strain curve and proposed model for non-compressed specimens.

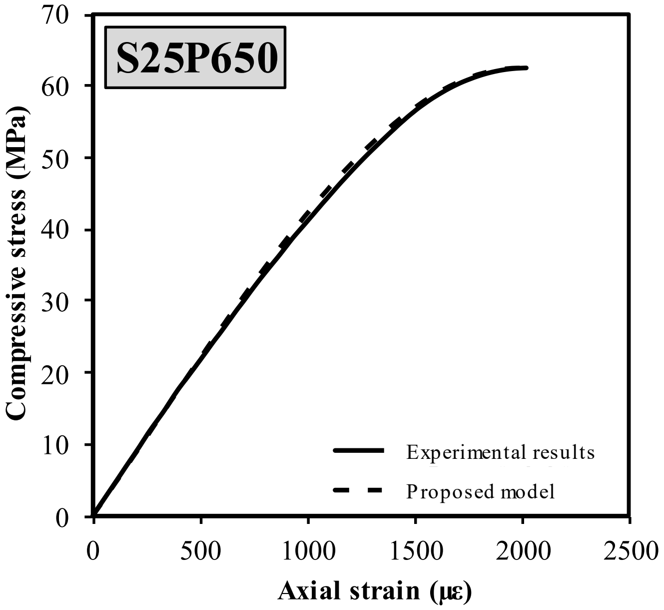
S25P650
Compressive stress (MPa)
0
10
20
30
40
50
60
70
0
500
1000
1500
2000
2500
Axial strain (με)
Experimental results
Proposed model

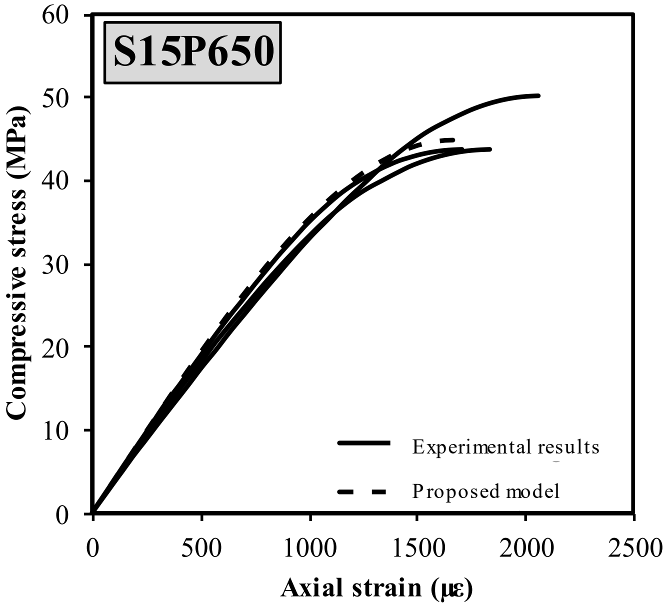
S15P650
Compressive stress (MPa)
0
10
20
30
40
50
60
0
500
1000
1500
2000
2500
Axial strain (με)
Experimental results
Proposed model

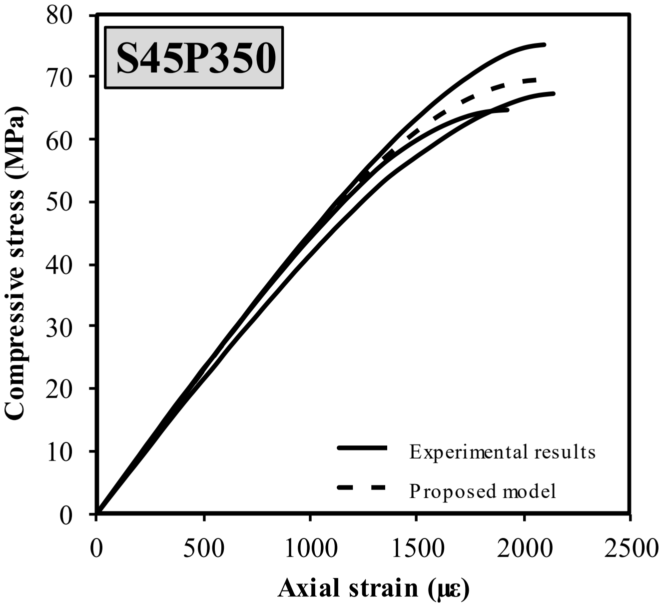
S45P350
Compressive stress (MPa)
0
10
20
30
40
50
60
70
80
0
500
1000
1500
2000
2500
Axial strain (με)
Experimental results
Proposed model

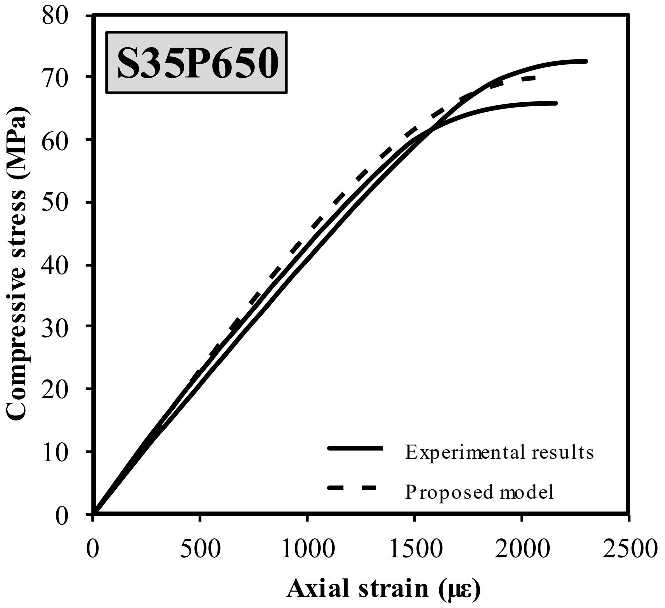
S35P650
Compressive stress (MPa)
0
10
20
30
40
50
60
70
80
0
500
1000
1500
2000
2500
Axial strain (με)
Experimental results
Proposed model

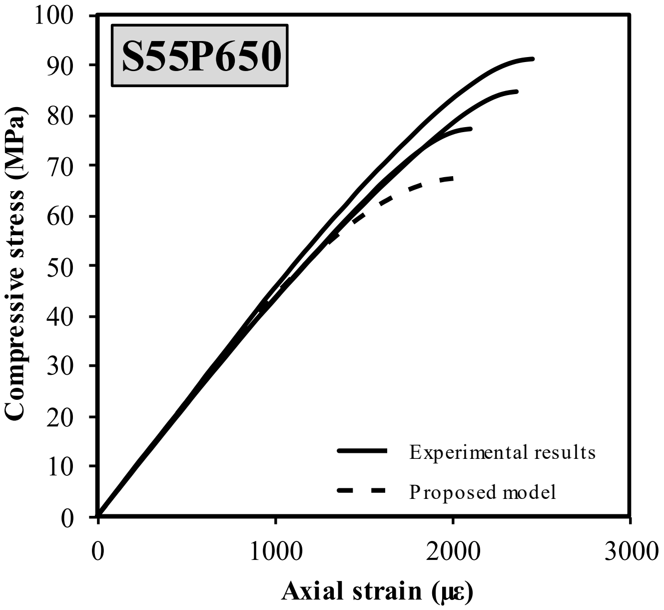
S55P650
Compressive stress (MPa)
0
10
20
30
40
50
60
70
80
90
100
0
1000
2000
3000
Axial strain (με)
Experimental results
Proposed model

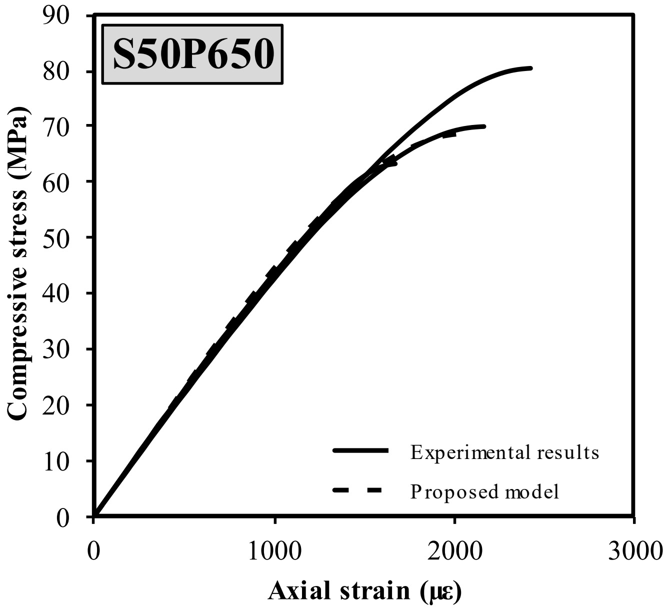
S50P650
Compressive stress (MPa)
0
10
20
30
40
50
60
70
80
90
0
1000
2000
3000
Axial strain (με)
Experimental results
Proposed model

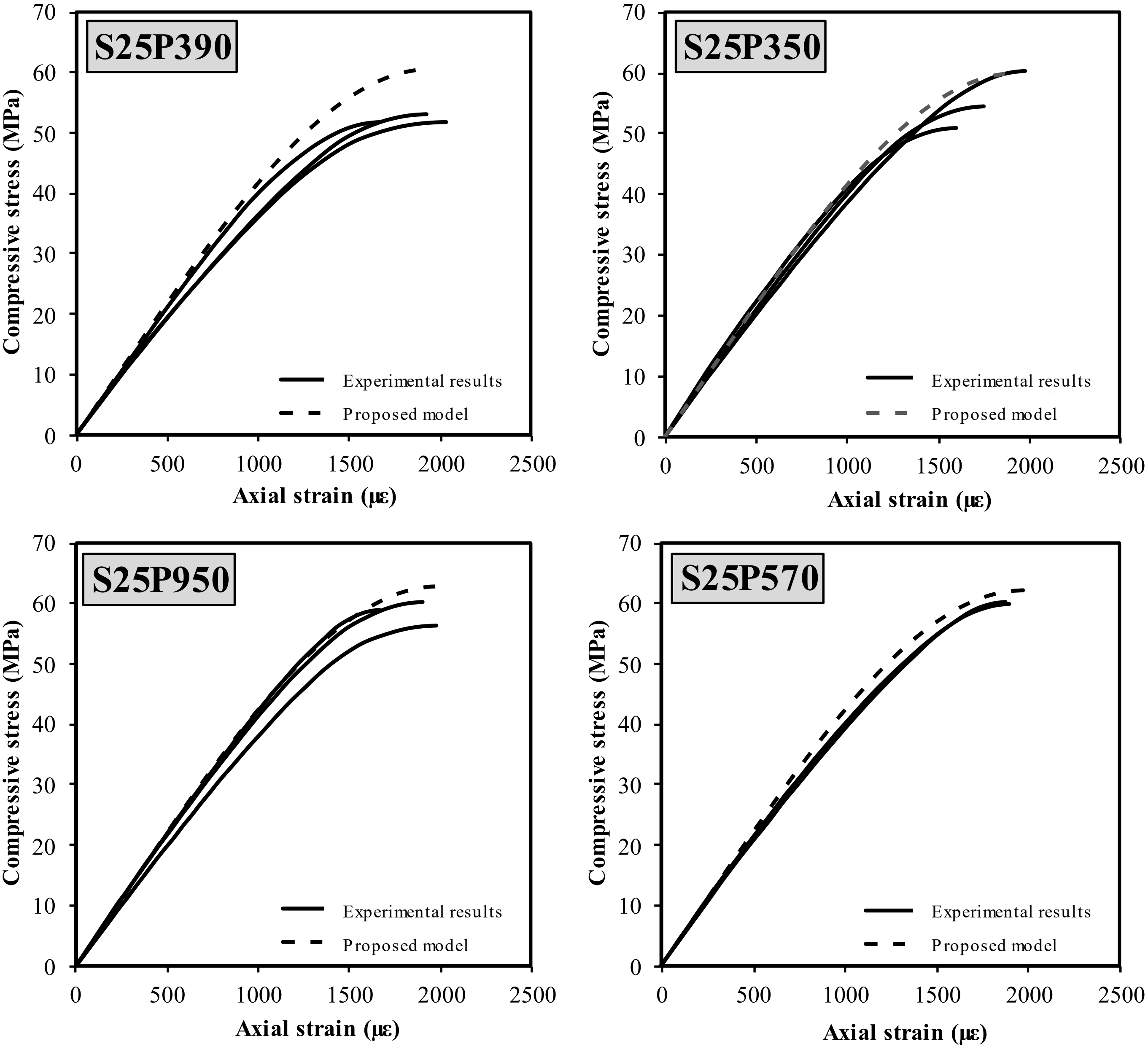

Fig. 3. Experimental stress-strain curve and proposed model for compressed specimens.

The parameters of the stress block can be readily determined using Eq. 1. For a given strain level, the internal force in the concrete can be expressed in terms of the equivalent stress block parameters α_1 and C, where $C = \alpha_1 f'_c \beta_1 c\ b$ denotes the depth of the neutral axis measured from the extreme compression fiber, and b represents the width of the cross-section. The stress block parameters can be derived from the first and second moments of area based on the stress–strain relationships, leading to the following results:

$$\alpha_1\beta_1 = \frac{\int_0^{\varepsilon_c} \sigma_c \, d\varepsilon_c}{f'_c \varepsilon_c} \tag{2}$$

$$\beta_1 = 2 - 2\frac{\int_0^{\varepsilon_c} \sigma_c \, \varepsilon_c \, d\varepsilon_c}{\varepsilon_c \int_0^{\varepsilon_c} \sigma_c \, d\varepsilon_c} \tag{3}$$

3. Results and discussion

By integrating Eqs. 2 and 3 and using stress-strain Eq. 1, the stress block equations at any instant will be as follows:

$$\alpha_1\beta_1 = \frac{mk}{2} + \frac{(3-2m)\,k^2}{3} + \frac{(m-2)\,k^3}{4} \tag{4}$$

$$\beta_1 = \frac{20\,mk^3 + 10\,(3-2m)k^4 + 6(m-2)k^5}{30\,mk^3 + 20\,(3-2m)k^4 + 15(m-2)k^5} \tag{5}$$

In the above equations, $k = \varepsilon_c/\varepsilon_0$, while ε_0 and ε_c represent, respectively, the strain at maximum stress and the strain of concrete at any arbitrary point along the stress–strain curve.

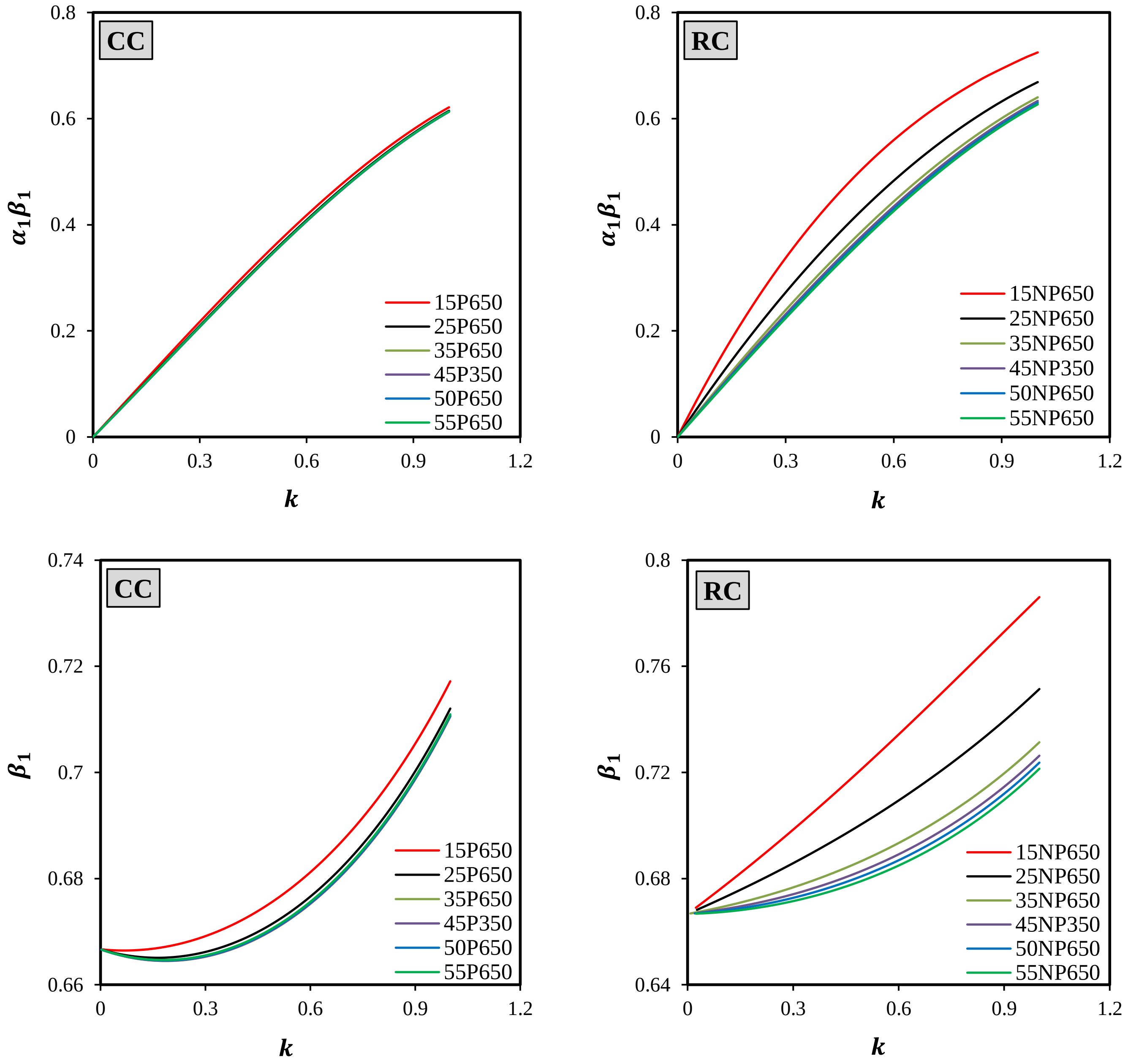

Fig. 4. Stress block parameters for RC and CC.

The stress block parameters at each instant for both compressed and non-compressed specimens are illustrated in Fig. 4. This figure shows the effect of β_1 and $\alpha_1\beta_1$ on k. As evident from the figure, the stress block parameters decrease with increasing compressive strength of the specimens. If, in Eqs. 4 and 5, the value of k is replaced with 1, then the stress block parameters at the peak point can be obtained as follows:

$$\alpha_1\beta_1 = \frac{m+6}{12} \tag{6}$$

$$\beta_1 = \frac{6m+18}{5m+30} \tag{7}$$

Table 1 presents the rectangular stress block parameters proposed by various design codes and researchers. Fig. 5 illustrates a comparative analysis between the rectangular stress block parameters proposed in this study and those suggested by other researchers. In the present investigation, at the ultimate strain level, the parameter α_1 for RC and CC specimens was found to range between 0.86 to 0.93 and 0.86 to 0.87, respectively. Similarly, the parameter β_1 for these specimens was obtained in the range of 0.72 to 0.80 for RC and 0.71 to 0.72 for CC.

4. Conclusions

In this study, the adequacy and accuracy of rectangular stress block parameters for high-strength prestressed (freshly compressed) concrete were investigated through analytical modeling and experimental comparison. A simplified third-degree polynomial stress–strain relationship was proposed to represent the entire loading process, and its predictions were validated against experimental data for both non-compressed and compressed concretes. The findings of this research can be summarized as follows.

Table 1. Rectangular stress block parameters.

Reference	α_1	β_1
ACI-318 [8]	0.85	$1.09 - 0.008f'_c$, $(0.85 \geq \beta_1 \geq 0.65)$
Eurocode-2 [19]	0.85	$0.9 - f'_c/500$
CSA-94 [20]	$0.85 - 0.0015f'_c \geq 0.67$	$0.97 - 0.0025f'_c \geq 0.67$
NZS-95 [21]	$1.07 - 0.004f'_c$, $(0.85 \geq \alpha_1 \geq 0.75)$	$1.09 - 0.008f'_c$, $(0.85 \geq \beta_1 \geq 0.65)$
Attard and Stewart [22]	$0.6470f'^{0.0324}_c \geq 0.58$	$0.948f'^{-0.091}_c \geq 0.67$
Ibrahim and MacGregor [23]	$0.85 - f'_c/800 \geq 0.725$	$0.95 - f'_c/4000 \geq 0.7$
Li et al. [24]	$0.85 - 0.004\,(f'_c - 55) \geq 0.75)$	$1.09 - 0.008f'_c$, $(0.85 \geq \beta_1 \geq 0.65)$
Azizinamini et al. [25]	$0.85 - 0.0073\,(f'_c - 69) \geq 0.6)$	$1.09 - 0.008f'_c$, $(0.85 \geq \beta_1 \geq 0.65)$
Oztekin et al. [11]	$0.964 - 0.002f'_c$	$0.805 - 0.0012f'_c$

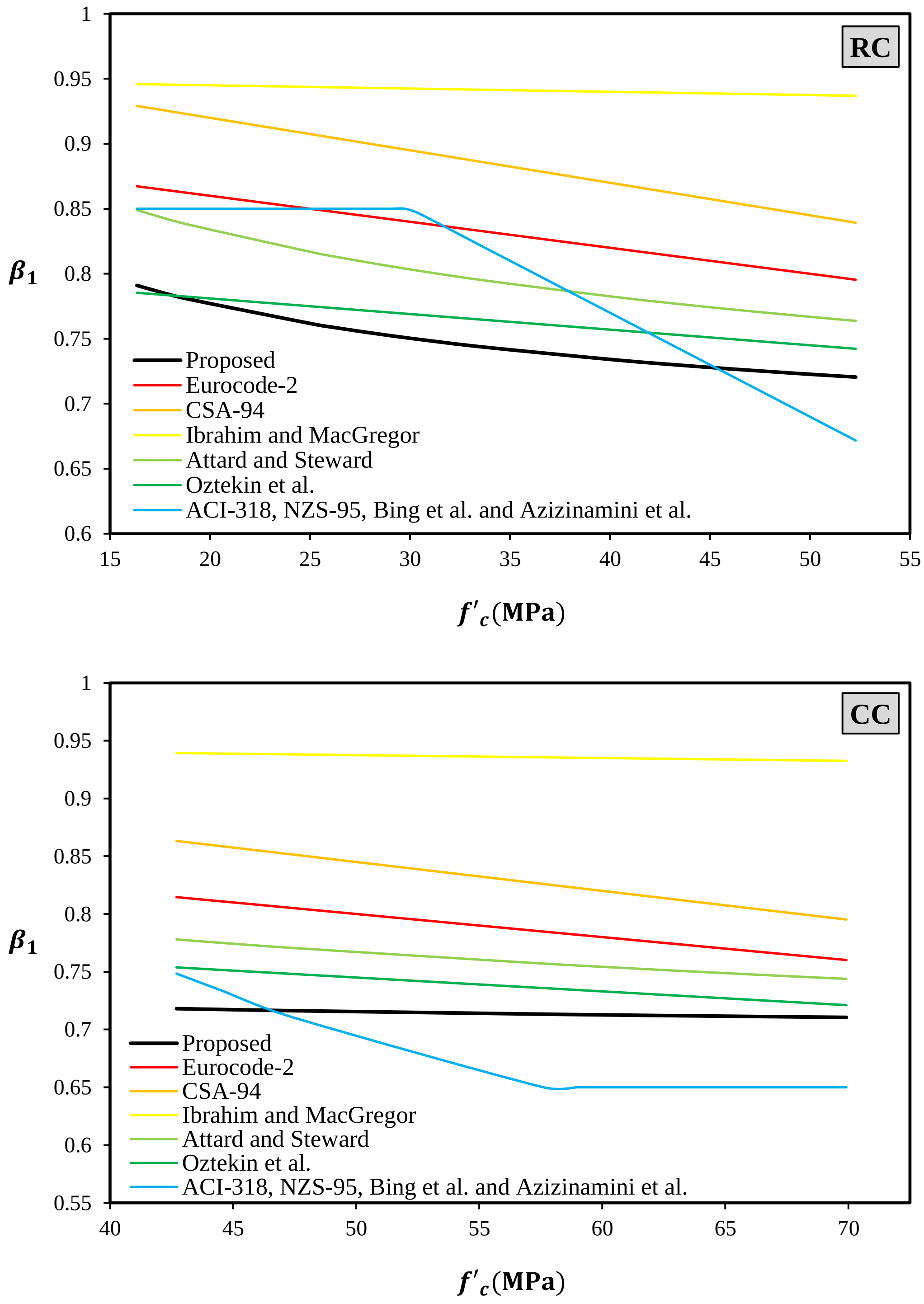

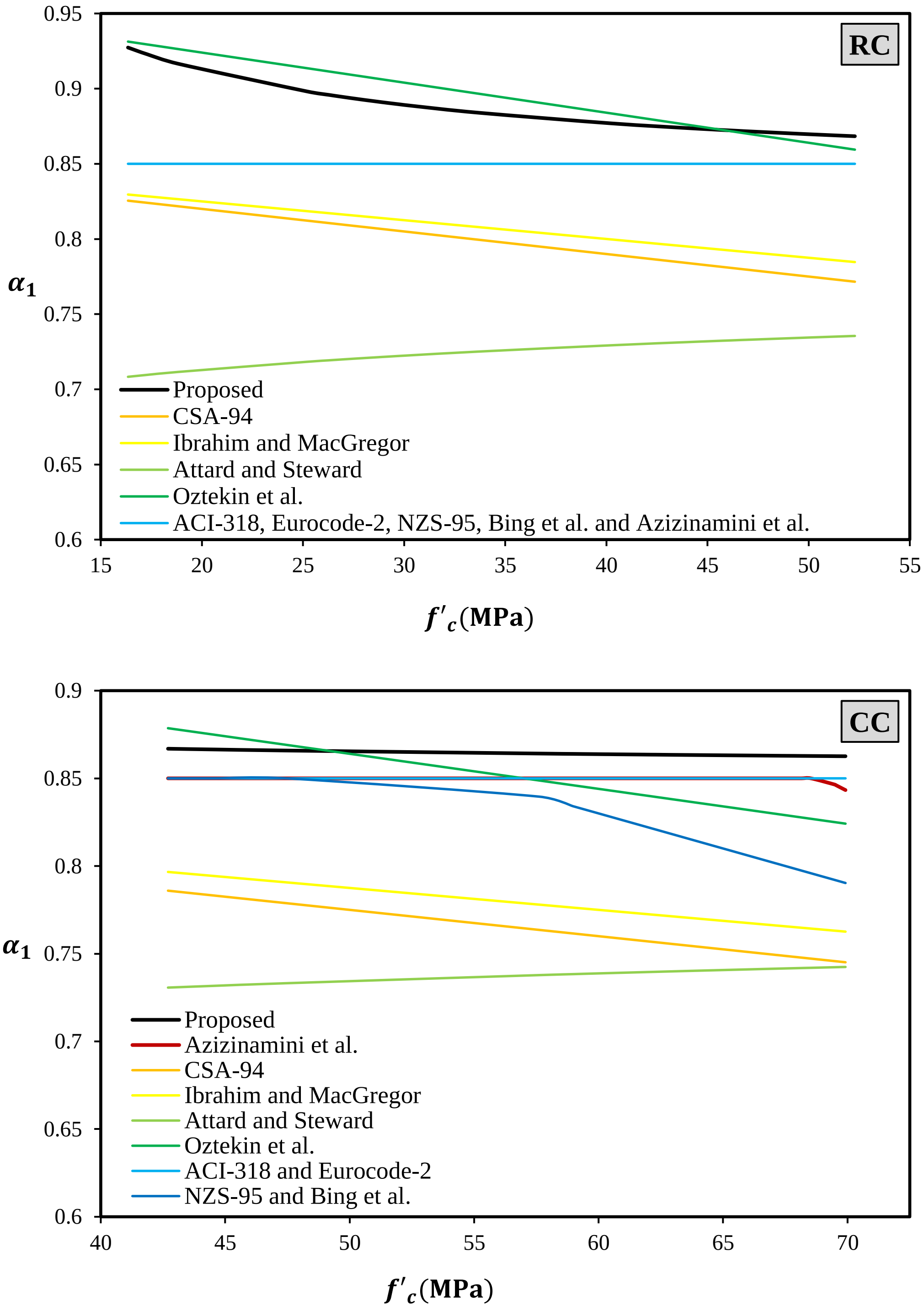

Fig. 5. Relationships between stress block parameters and concrete strength.

- Developed model satisfies four critical boundary conditions, including the stress and strain values at key points along the curve, and was benchmarked against validated experimental data for both compressed and non-compressed concrete specimens. The results demonstrated that the proposed model predicts the actual behavior of concrete with a satisfactory level of accuracy and is suitable for analyzing the parameters of the rectangular stress block.
- The primary parameters of the rectangular stress block, namely α (the ratio of equivalent compressive stress to the concrete compressive strength) and β (the ratio of stress block height to the depth of the neutral axis), were evaluated throughout the loading process, particularly at the ultimate strain level. Analytical results indicated that both α and β decrease with increasing concrete compressive strength, and this reduction can significantly influence the flexural capacity of structural members as well as the prediction of their failure modes. In particular, for high-strength prestressed concrete, conventional code-based models may lack sufficient accuracy, and their direct application could lead to non-conservative or overly conservative outcomes.
- A comparison between the results of this study and the stress block parameters presented in various design codes and by other researchers indicates that current code-based formulations require revision, particularly when applied to concrete with

compressive strengths exceeding 60 MPa. The instantaneous parameters proposed in this research may serve as a foundation for the development of more accurate and safer design methodologies for reinforced concrete members.

- Overall, the implementation of the proposed stress–strain model and its derived parameters offers a reliable approach for enhancing the accuracy of engineering design and performance analysis of structural members, particularly in high-strength prestressed concrete structures. These findings may serve as a foundation for revising existing design codes and advancing innovative design methodologies in future practice.

Statements & declarations

Author contributions

Shahram Maghsodian: Conceptualization, Investigation, Methodology, Formal analysis, Resources, Writing - Original Draft, Writing - Review & Editing.

Funding

The authors received no financial support for the research, authorship, and/or publication of this article.

Data availability

The data presented in this study will be available on interested request from the corresponding author.

Declarations

The authors declare no conflict of interest.

References

[1] Gusella, F. Effect of the plastic rotation randomness on the moment redistribution in reinforced concrete structures. Engineering Structures, 2022; 252: 113652. doi:10.1016/j.engstruct.2021.113652.

[2] Nemati, M., Aminian, A., Rahimi, S., Nematzadeh, M., Jafarzadeh-Taleshi, M., Thai, H.-T. Compressive behavior of prestressed SFRCFST stub columns after heating: Effect of fresh concrete compression technique. Case Studies in Construction Materials, 2025; 23: e04968. doi:10.1016/j.cscm.2025.e04968.

[3] Nazari, A., Toufigh, V. Effects of elevated temperatures and re-curing on concrete containing rice husk ash. Construction and Building Materials, 2024; 439: 137277. doi:10.1016/j.conbuildmat.2024.137277.

[4] Razavi, M., Rahimi, M., Hasanpoor Tichi, A., Nematzadeh, M. Synergistic effects of recycled nylon granules and bacterial nano-cellulose in lightweight concrete: Experiments and predictions. Construction and Building Materials, 2025; 493: 143124. doi:10.1016/j.conbuildmat.2025.143124.

[5] Tarkhan, M., Hosseini-Poul, S.-A., Nematzadeh, M., Shokrollah-Hefzabad, A. Evaluation of post-heating flexural behavior of concrete incorporating ceramic waste and electric arc furnace slag: Experimental and predictive study, and carbon footprint assessment. Construction and Building Materials, 2025; 494: 143207. doi:10.1016/j.conbuildmat.2025.143207.

[6] Nematzadeh, M., Nazari, A., Tayebi, M. Post-fire impact behavior and durability of steel fiber-reinforced concrete containing blended cement–zeolite and recycled nylon granules as partial aggregate replacement. Archives of Civil and Mechanical Engineering, 2021; 22: 5. doi:10.1007/s43452-021-00324-1.

[7] Whitney, C. S. Design of reinforced concrete members under flexure or combined flexure and direct compression. ACI Journal Proceedings, 1937; 33: 483-498. doi:10.14359/8429.

[8] American Concrete Institute (ACI). ACI 318-25: Building Code for Structural Concrete—Code Requirements and Commentary. Farmington Hills (MI): ACI; 2025.

[9] Mattock, A. H., Kriz, L. B., Hognestad, E. Rectangular concrete stress distribution in ultimate strength design. ACI Journal Proceedings, 1961; 57: 875-928. doi:10.14359/8051.

[10] Li, B. Strength and Ductility of Reinforced Concrete Members and Frames Constructed Using High Strength Concrete(PhD Thesis). Christchurch (NZ): University of Canterbury; 1993.

[11] Oztekin, E., Pul, S., Husem, M. Determination of rectangular stress block parameters for high performance concrete. Engineering Structures, 2003; 25: 371-376. doi:10.1016/S0141-0296(02)00172-4.

[12] Ozbakkaloglu, T., Saatcioglu, M. Rectangular stress block for high-strength concrete. ACI Structural Journal, 2004; 101: 475-483. doi:10.14359/13333.

[13] Mertol, H. C., Rizkalla, S., Zia, P., Mirmiran, A. Flexural Design using High-Strength Concrete up to 20 KSI. In: HPC: Build Fast, Build to Last. The 2006 Concrete Bridge Conference; 2006 May 7-10; Nevada, United States. p. 1-18.

[14] Ho, J., Peng, J. Strain gradient effects on flexural strength design of normal-strength concrete columns. Engineering Structures, 2011; 33: 18-31. doi:10.1016/j.engstruct.2010.09.014.

[15] Van Zijl, G., Mbewe, P. Flexural modelling of steel fibre-reinforced concrete beams with and without steel bars. Engineering Structures, 2013; 53: 52-62. doi:10.1016/j.engstruct.2013.03.036.

[16] Prachasaree, W., Limkatanyu, S., Hawa, A., Samakrattakit, A. Development of equivalent stress block parameters for fly-ash-based geopolymer concrete. Arabian journal for science and engineering, 2014; 39: 8549-8558. doi:10.1007/s13369-014-1447-2.

[17] Maruyama, I., Sasano, H. Strain and crack distribution in concrete during drying. Materials and Structures, 2014; 47: 517-532. doi:10.1617/s11527-013-0076-7.

[18] Nematzadeh, M., Naghipour, M. Compressive strength and modulus of elasticity of freshly compressed concrete. Construction and Building Materials, 2012; 34: 476-485. doi:10.1016/j.conbuildmat.2012.02.055.

[19] British Standards Institution. EN 1992-1-2: Eurocode 2: Design of concrete structures. Ispra (IT): EN; 2004.

[20] Canadian Standards Association (CSA). CSA A23.3:19: Design of Concrete Structures. Longueuil (QC): CSA; 2019.

[21] New Zealand Standards Association. NZS 3101.1: Concrete structures standard - The design of concrete structures. Wellington (NZ): NZS; 2006.

[22] Attard, M. M., Stewart, M. G. A two parameter stress block for high-strength concrete. ACI Structural Journal, 1998; 95: 305-317. doi:10.14359/548.

[23] Ibrahim, H. H. H., MacGregor, J. G. Modification of the ACI rectangular stress block for high-strength concrete. ACI Structural Journal, 1997; 94: 40-48. doi:10.14359/459.

[24] Li, B., Park, R., Tanaka, H. Effect of confinement on the behaviour of high strength concrete columns under seismic loading. In: Proceedings, Pacific conference on earthquake engineering; 1991 Nov 20-23; Auckland, New Zealand. p. 67-78.

[25] Azizinamini, A., Baum Kuska, S. S., Brungardt, P., Hatfield, E. Seismic behavior of square high-strength concrete columns. ACI Structural Journal, 1994; 91: 336-345. doi:10.14359/4362.

Civil Engineering and Applied Solutions, 2026; 2(1): 33–45

Civil Engineering and Applied Solutions

Research Article

journal homepage: ceas.journals.umz.ac.ir

Finite Element Modeling of SMA-Confined Concrete: Influence of Winding Pitch and Temperature on Strength and Energy Dissipation

Moein Rezapour [a], Mehdi Ghassemieh [a*]

[a] *College of Engineering, School of Civil Engineering, University of Tehran, Tehran, Iran*

ARTICLE INFO

Keywords:
Shape memory alloy
Concrete confinement
Finite element modeling
Energy dissipation

Article history:
Received 14 September 2025
Accepted 11 October 2025
Available online 01 January 2026

ABSTRACT

This study presents a detailed finite element investigation of concrete cylinders confined with shape memory alloy (SMA) windings, focusing on the combined effects of winding pitch and temperature. The main objective is to evaluate how geometric configuration and thermal activation influence the compressive strength, ductility, and energy dissipation of confined concrete. The nonlinear response was modeled in ABAQUS using the Concrete Damaged Plasticity (CDP) framework for the concrete core and a user-defined FORTRAN subroutine to simulate the reversible austenite–martensite transformation of the SMA. The numerical model was validated against laboratory data, showing strong agreement between simulated and experimental stress–strain curves. Parametric analyses were performed for winding pitches of 5.3, 9, and 16 mm under temperatures of 30, 50, 70, and 90 °C. The results demonstrate that decreasing the winding pitch substantially enhances post-peak stability and energy absorption, while higher SMA temperatures improve confinement efficiency at large strains without significantly altering peak strength. The study confirms that tighter and thermally activated SMA windings provide more uniform stress distribution and superior energy dissipation. These findings highlight the potential of SMA-based active confinement as a reliable and adaptive strategy for seismic retrofitting and impact-resistant design of concrete structures.

1. Introduction

Ensuring the long-term durability and safety of concrete structures under lateral loads and variable environmental conditions has remained a central challenge in structural engineering. Enhancing the compressive strength and ductility of concrete is particularly critical in seismic and harsh exposure scenarios. Conventional confinement methods, such as steel hoops or fiber-reinforced polymers, have demonstrated reasonable effectiveness but exhibit notable limitations when subjected to temperature fluctuations and cyclic loading. Shape memory alloys (SMAs), owing to their unique properties including superelastic behavior, strain recovery, and mechanical stability over a wide temperature range, have emerged as a new generation of smart materials for concrete strengthening. Recent studies indicate that incorporating SMA wires or strips as active or passive wraps can substantially improve energy dissipation capacity and mitigate damage in concrete members. Nevertheless, the influence of key parameters, such as wrap pitch, temperature, and pre-tension level, on the overall response of SMA-confined concrete remains insufficiently clarified.

Enhancing the compressive capacity and ductility of concrete under axial and seismic loading remains a fundamental concern in structural engineering. Ordinary concrete, due to its inherent brittleness and limited post-peak strain capacity, is highly vulnerable to cyclic loading and large deformations. Traditional confinement techniques, such as steel stirrups and fiber-reinforced polymers (FRP), can improve strength and strain capacity, yet they exhibit notable shortcomings when exposed to temperature variations, cyclic fatigue, and progressive degradation of bond performance [1].

The advent of smart materials, particularly shape memory alloys (SMA), has opened new avenues for both active and passive

---

* Corresponding author.
E-mail addresses: m.ghassemieh@ut.ac.ir (M. Ghassemieh).

https://doi.org/10.22080/ceas.2025.30055.1042
ISSN: 3092-7749/© 2026 The Author(s). Published by University of Mazandaran.

How to cite this article: Rezapour, M., Ghassemieh, M. Finite Element Modeling of SMA-Confined Concrete: Influence of Winding Pitch and Temperature on Strength and Energy Dissipation. Civil Engineering and Applied Solutions. 2026; 2(1): 33–45. doi:10.22080/ceas.2025.30055.1042.

strengthening of concrete members. Unique characteristics such as the shape-memory effect, superelastic behavior, high energy dissipation capacity, and the ability to induce intrinsic prestressing in SMA wires or strips have positioned these alloys as a promising alternative in structural engineering over the past two decades [2, 3]. Early reviews, including the seminal work by DesRoches et al. (2004), outlined the potential applications of SMA in seismic control and ductility enhancement while highlighting key research gaps that remain to be addressed [4].

The first experimental investigations focused on SMA-based confinement of concrete were conducted by Choi et al. By wrapping NiTi wires around concrete cylinders, they demonstrated marked improvements in compressive strength, ultimate strain, and energy dissipation compared with control specimens [5]. Subsequently, Shin and Andrawes introduced the concept of active confinement, wherein SMA wires, once heated and allowed to return to their original length, generate a stable confining pressure. Their findings indicated that this approach not only enhances strength but also promotes recentering and reduces residual deformation after unloading [6]. Building on this concept, Andrawes and et al. have conducted multiple studies validating the superior cyclic stability of SMA-confined columns relative to those reinforced with conventional transverse steel [7].

Gholampour and Ozbakkaloglu conducted a comprehensive study on both normal-strength and high-strength concrete, examining parameters such as SMA volumetric ratio and the austenitic/martensitic phase state [8, 9]. Their results showed that SMA confinement can increase compressive strength and ultimate strain by several multiples compared with control specimens, while producing a smoother stress–strain response that is highly favorable for seismic performance. Comparable findings have been reported in several other studies, including Park et al. who compared SMA wrapping with steel jacketing and observed a pronounced improvement in ductility [10].

The high cost of NiTi alloys and the manufacturing limits on wire diameter have, in recent years, shifted growing attention toward iron-based alloys (Fe-SMA). These materials retain the shape-memory effect and prestressing capability while being substantially more cost-effective and easier to install. Lee et al. in a laboratory investigation on circular reinforced-concrete columns under cyclic loading, reported significant gains in strength, ductility, and deformation stability through the application of Fe-SMA strips [11]. Similarly, Tran et al. demonstrated that using Fe-SMA wires in an active configuration markedly enhances the energy dissipation capacity of cylindrical specimens [12]. Recent studies combining Fe-SMA with FRP have further revealed a pronounced synergistic improvement in compressive capacity and post-peak softening behavior [13].

From a modeling perspective, the Concrete Damaged Plasticity (CDP) framework in ABAQUS has become the predominant approach for simulating the behavior of confined concrete. The model proposed by Lee and Fenves (1998) serves as the basis for many calibrations, providing robust capability to reproduce stress–strain curves in both compression and tension [14]. Seminal contributions by Martinez-Rueda and Elnashai and Dolce and Cardone (2001) formulated constitutive relationships for confined concrete and SMA under cyclic loading [15-17]. More recent numerical studies have advanced predictive stress–strain models for SMA-confined columns, offering valuable insights for the future of seismic design [18, 19].

Beyond full wrapping, SMA applications have also expanded into other domains such as beam–column connections, energy dissipation devices, and re-centering systems. Ocel et al. (2004) investigated beam–column joints equipped with SMA bolts and reported markedly higher re-centering capacity compared to conventional connections [20].

Despite the growing body of literature on SMA confinement, the combined effects of winding pitch and thermal activation remain insufficiently understood. This study therefore aims to quantify their influence on the strength, ductility, and energy dissipation of SMA-confined concrete through finite element simulations. Despite notable progress, future research must address issues such as behavior under eccentric loading, long-term durability, cyclic fatigue effects, and large-scale model calibration to establish the industrial viability of this technology. In the present study, numerical modeling in ABAQUS employing the Concrete Damaged Plasticity framework is used to examine the influence of wrap pitch and thermal conditions on the compressive strength and energy dissipation capacity of SMA-confined concrete specimens, aiming to advance the seismic and functional applications of this technology in concrete structures.

2. Shape memory alloys

Shape memory alloys (SMA) are a class of smart metallic materials capable of returning to their original configuration after experiencing substantial deformation. This unique behavior arises from a reversible phase transformation between two crystal structures: austenite and martensite (Fig. 1). Above the transformation temperature, the austenitic phase—characterized by a stable cubic lattice—exhibits high stiffness and elastic properties typical of conventional metals. Upon cooling or the application of stress, the crystal arrangement shifts to the martensitic phase, which has a monoclinic structure, is comparatively softer, and contains multiple variants that can easily reorient under stress, enabling large recoverable strains without permanent lattice slip [21]. The austenite-to-martensite transformation is shear-dominated and diffusionless; therefore, when the stimulus (heat or stress) is removed, the lattice promptly reverts to its original configuration.

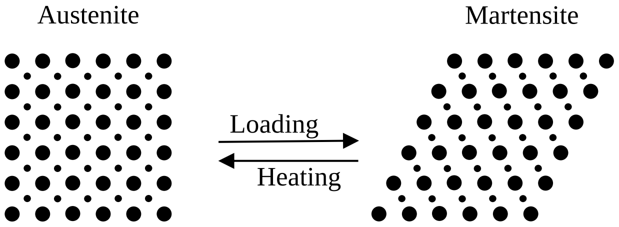

Fig. 1. Phase transformation of the SMA [19].

When an SMA deforms in the martensitic state, the apparent elongation results from the reorientation of martensitic variants rather than irreversible lattice changes. Reheating the alloy restores the austenitic structure, allowing complete shape recovery—commonly referred to as the shape memory effect. At temperatures above the austenite finish point, applied stress can induce stress-driven martensite, which reverts to austenite upon unloading, producing a closed stress–strain loop with significant hysteresis known as superelasticity [22, 23]. Chemical composition and heat treatment govern the transformation temperatures, enabling the design of alloys tailored to specific service environments. Together with their energy dissipation capacity and inherent re-centering capability, these characteristics make SMAs attractive for seismic retrofitting, active prestressing, and ductility enhancement of concrete members.

Prestressing in SMAs stems from the recovery strain during the martensite-to-austenite transformation. A wire or strip of SMA is first elongated or helically wound around a concrete member in the martensitic phase. Heating the material above its transformation temperature triggers the phase shift to austenite and induces a tendency to return to its pre-deformed length. Because the SMA is restrained by the surrounding concrete, this contraction manifests as a permanent circumferential compressive stress on the member, effectively providing an active confining pressure. This method eliminates the need for hydraulic jacks or mechanical anchors while ensuring a stable and uniform confinement from the onset of service. The resulting compressive hoop stress increases axial strength, delays crack initiation, and improves ductility and energy dissipation under cyclic loading. Consequently, SMA-based active prestressing offers an efficient strategy for enhancing the seismic performance of columns and other compression-dominated structural elements.

3. FEM modeling

In this study, the confinement behavior of concrete is modeled using the ABAQUS finite element software. Although ABAQUS provides a wide range of built-in material models—such as isotropic nonlinear behavior, concrete damaged plasticity, smeared crack approaches, Mohr–Coulomb and Drucker–Prager models for soils, and others—it does not natively include the constitutive behavior of shape memory alloys (SMAs). One of the advantages of ABAQUS, however, is its ability to incorporate user-defined material subroutines written in FORTRAN, allowing the introduction of new constitutive models. Therefore, the behavior of SMAs must first be coded in this environment and then linked to ABAQUS. Lagoudas, in his research at the University of Texas, developed such a subroutine for SMAs and performed the necessary verifications. Accordingly, in the present study, Lagoudas's user material subroutine is employed to model the SMA behavior [2].

The specimen modeled in this research was experimentally investigated by Hashemivand [24]. The concrete sample, with a compressive strength of 25 MPa and dimensions of 120 × 60 mm, was subjected to axial compression (Fig. 2). As shown in the figure, two steel rings, each 1 mm thick and 20 mm in height, were placed at the top and bottom of the specimen, and a 1-mm diameter Nitinol wire was wound around the specimen for ten turns.

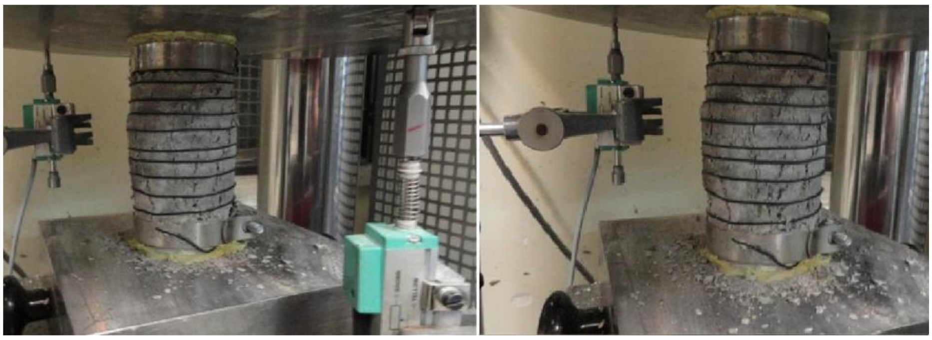

Fig. 2. Concrete specimen confined in the laboratory [24].

The nitinol tested in this study has mechanical properties as shown in Table 1. Numerical modeling of the behavior of concrete confined with a shape memory alloy was performed in the ABAQUS finite element environment to enable accurate simulation of the nonlinear response under axial loading. Concrete was defined using the Concrete Damaged Plasticity (CDP) model, which is among the most comprehensive approaches available for predicting compressive and tensile behavior as well as post-peak energy dissipation. This model accounts for strain softening, modulus degradation, and the gradual reduction of load-carrying capacity due to microcracking, and it has been widely applied for analyzing the quasi-brittle response of concrete in both compression and tension.

Table 1. Mechanical properties of the shape memory alloy at 30 °C.

Elastic modulus	7.5×10^4 MPa
Start stress for austenite-to-martensite transformation	385 MPa
Finish stress for austenite-to-martensite transformation	516 MPa
Start stress for martensite-to-austenite transformation	356 MPa
Finish stress for martensite-to-austenite transformation	202 MPa
Superelastic strain range	6.25 %
Density	65 kN/m^3

Key parameters, including the internal friction angle, dilation ratio, initial elastic modulus, hardening coefficients, and damage factors, were determined according to the software guidelines and available experimental data. The compressive stress–strain curve was calibrated based on the cylindrical compressive strength and empirical coefficients; in the pre-peak region, the response was assumed to be nearly linear, while beyond the peak an exponential softening function was adopted to reproduce the gradual strength decay. In tension, a progressive damage law governed by fracture energy was implemented to realistically capture the transition from elastic behavior to microcracking and failure. This framework enabled prediction of modulus reduction and stiffness degradation due to cumulative damage, and the load–strain curves obtained from the model showed good agreement with trends reported in experimental studies.

In the concrete damaged plasticity (CDP) model implemented in ABAQUS, two key parameters are defined to represent the degradation of material capacity: dc (damage in compression) and dt (damage in tension). These coefficients describe the fraction of effective stiffness lost due to microcracking and softening, varying from zero (undamaged) to one (fully damaged).

Under compression, once strain exceeds the peak point, progressive microcracking and particle crushing reduce the effective modulus. This process is represented by the dc–εc curve, where dc begins to increase after the peak strain, producing a linear or exponential reduction in concrete stiffness. The curve shape is typically calibrated against the compressive fracture energy (Gc) and uniaxial test results to ensure that the area under the curve matches the dissipated energy. In tension, concrete exhibits predominantly brittle behavior accompanied by crack opening. Beyond the peak tensile stress, a rapid loss of capacity occurs, and softening is captured through the dt parameter. The dt–εt relationship is commonly specified as linear or exponential so that the area under the tensile stress–strain curve corresponds to the tensile fracture energy (Gt). During the analysis, ABAQUS computes the effective stiffness of each element as (1−d).E, where d represents dc or dt depending on the loading mode. This mechanism allows the model to reproduce both strength degradation and modulus reduction during cyclic or post-peak loading (Fig. 3).

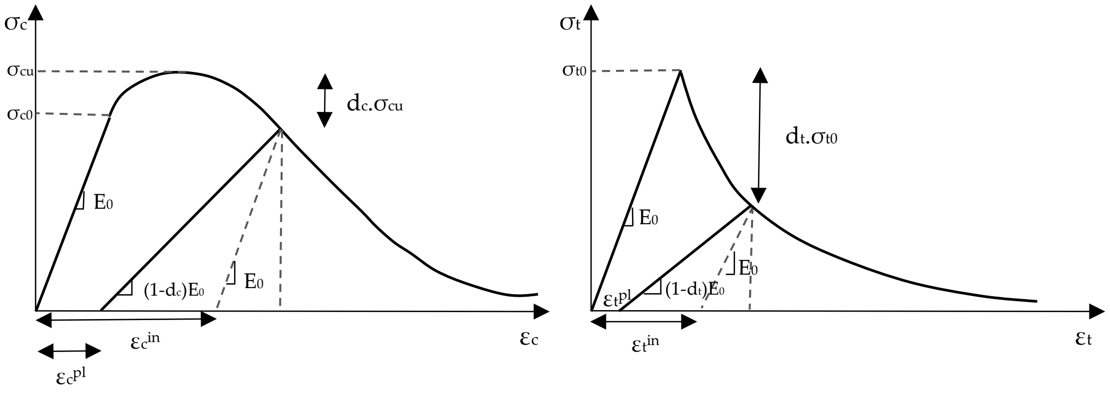

(a) **(b)**

Fig. 3. Dependence σ-ε for CDP model (a) in compression (b) in tension.

By accurately defining the dc and dt curves based on experimental data, numerical simulations can realistically represent microcrack initiation, gradual stiffness loss, and energy absorption capacity of concrete under both compression and tension, enabling reliable prediction of the nonlinear response of SMA-confined members. Since the loading in this study is predominantly monotonic, these two parameters were adopted accordingly.

The behavior of the shape memory alloy (SMA) was implemented through a user-defined subroutine (FORTRAN code) to reproduce the reversible austenite–martensite transformation and the associated mechanical hysteresis in the software. Within this code, transformation temperatures elastic moduli of the two phases, maximum recoverable strain, and temperature-dependent stress–strain curves were specified as input parameters. Stress-induced transformation and the shape-memory effect were formulated using thermodynamically based lattice-shear equations within an iterative algorithm to capture the pseudoelastic response and energy dissipation due to the hysteresis loop.

To simulate active prestressing, the initial length of the SMA element was modified in the martensitic state, and during a thermal analysis step the temperature was raised above Af, triggering length recovery and inducing circumferential compressive stress in the concrete member. This approach enables incorporation of both nonlinear behavior and the intrinsic prestressing effect of the SMA under axial loading, producing results consistent with experimental trends.

For accurate transfer of confining stress, the interaction between the SMA winding and the outer concrete surface was modeled as surface-to-surface contact: normal behavior was defined as hard contact, while a tangential friction coefficient of 0.3 was assigned to allow limited but realistic slip between wire and concrete. This formulation ensures that the compressive stress generated by SMA recovery is fully transmitted to the concrete wall, providing a realistic representation of active confinement. The interfaces between concrete and the loading platens were modeled using a tie constraint to apply uniform axial stress.

As observed in the experimental model, the concrete specimen consists of three main components: the concrete core, the steel restraining rings, and the winding. These components were modeled in the ABAQUS finite element environment as illustrated in Fig. 4. According to these figures, the elements used for the concrete core and the winding are eight-node solid brick elements (C3D8), while for ease of computation, the restraining rings were modeled using four-node shell elements (S4).

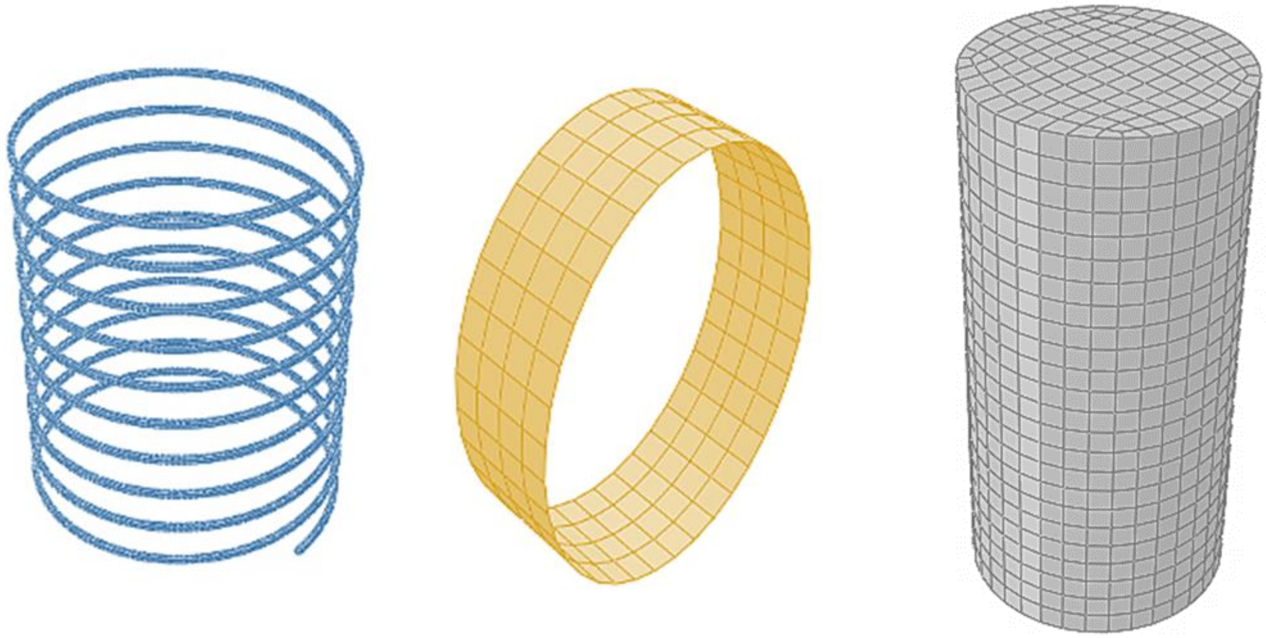

Fig. 4. Meshing of the concrete core, steel restraining rings, and shape memory alloy winding.

To connect these components, a tie interaction was defined. This interaction constrains the connected parts as if they were bonded, preventing any relative displacement between corresponding nodes. Fig. 5. Final finite element model and deformed shape, showing correct performance of the defined interactions.

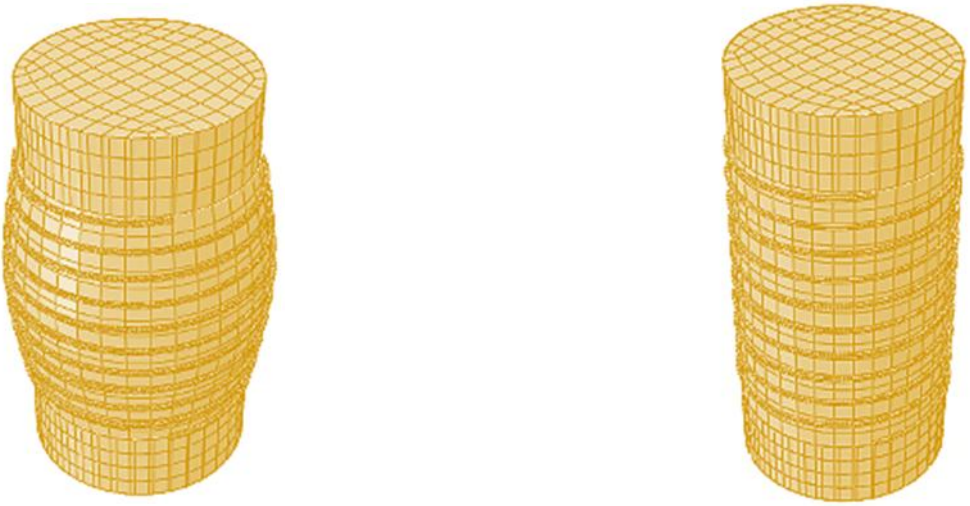

Fig. 5. Final finite element model and deformed configuration.

Fig. 6. Comparison of stress–strain curves for the experimental and numerical models. The figure demonstrates that the numerical model closely captures the nonlinear behavior observed in the laboratory specimen, including both the pre-peak stiffness and post-peak softening, validating the accuracy of the finite element modeling approach.

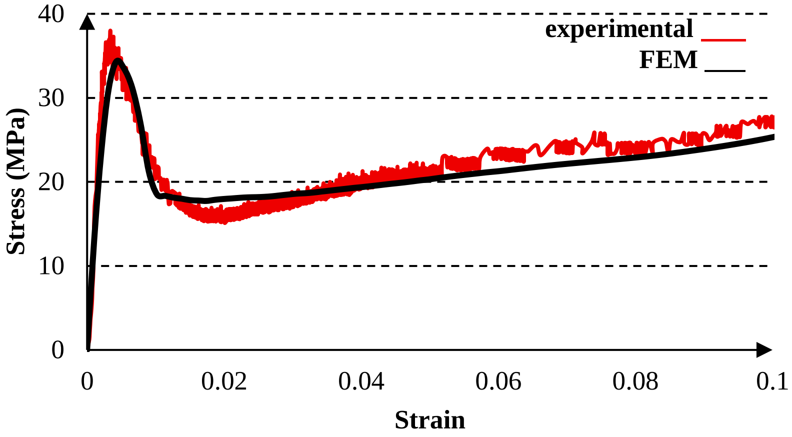

Fig. 6. Validation between experimental and numerical models.

What has been presented so far as the basis of the study primarily consisted of explanations regarding concrete confinement and its behavior under both active and passive conditions. In Chapter 4, the methodology for modeling confinement in ABAQUS was described, and a laboratory specimen was used to validate the numerical approach. In this chapter, to investigate more precisely the effect of shape memory alloys on the confinement of concrete, various configurations of the smart winding at different temperatures are examined. To evaluate these behaviors, several parameters including strength, energy dissipation, and others are considered.

4. Results

4.1. Effect of Winding Pitch

The winding pitch, defined as the center-to-center distance between adjacent turns, determines the effective number of SMA windings per specimen height. The first parameter investigated in this study is the winding pitch in concrete confinement (here, the pitch refers to the center-to-center distance of one complete turn). To examine this effect, three models with different pitches (16 mm, 9 mm, and 5.3 mm) were considered, with confinement provided by Nitinol wires (Fig. 7).

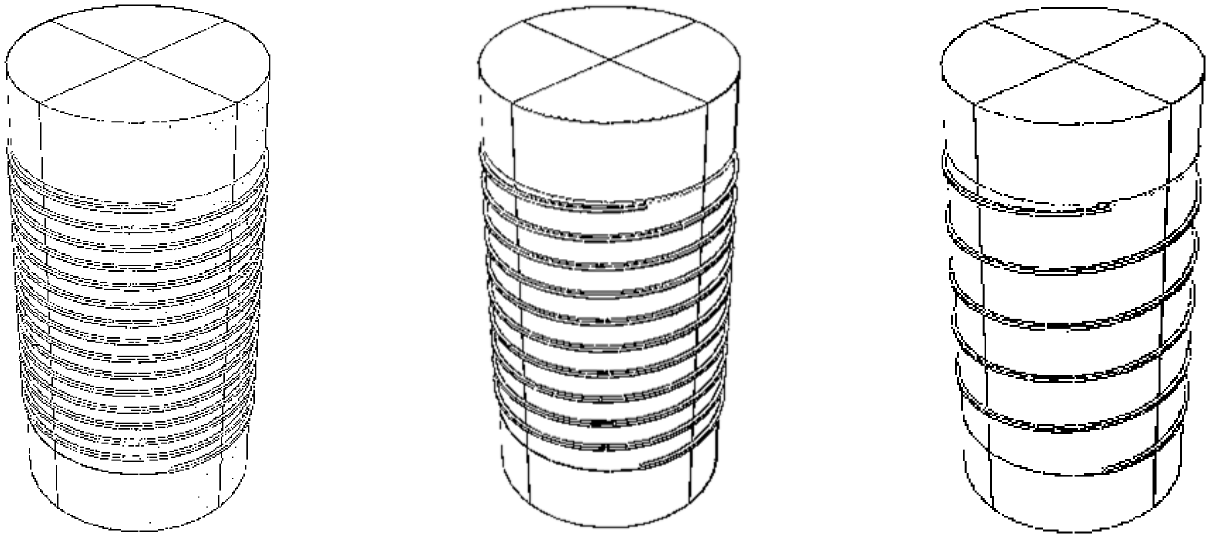

(a) **(b)** **(c)**

Fig. 7. Models with different winding pitches: (a) 5.3 mm pitch, (b) 9 mm pitch, (c) 16 mm pitch.

The models shown in Fig. 7 were subjected to axial compression applied from the top. This loading was applied until the specimens failed, causing significant lateral expansion in the concrete cores. With this expansion, the surrounding shape memory alloy (SMA) windings become active, inducing confinement in the specimen.

To investigate the effect of the number of SMA windings on the overall confinement of the system, the three specimens were analyzed under compressive loading. Fig. 8 presents the stress–strain curves for these systems at 30 °C. As expected, increasing the winding density enhances the strength of the specimens. Moreover, because SMAs exhibit strain-hardening behavior at large deformations, higher winding density leads to greater confinement capacity at elevated strains. While an increased number of windings slightly raises the peak compressive strength, its effect becomes more pronounced in the post-peak, large-strain region.

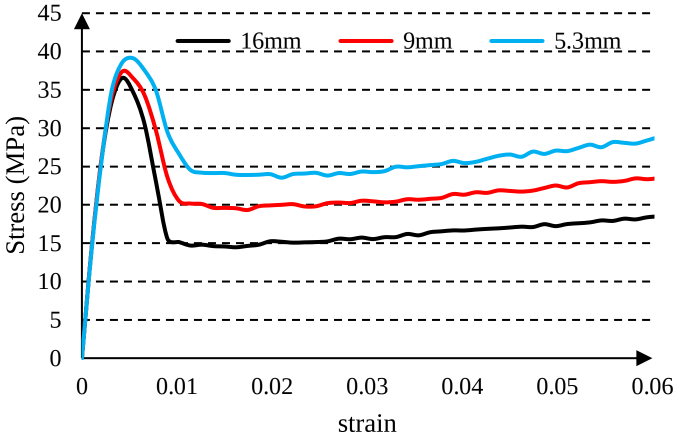

Fig. 8. Compressive stress–strain curves of specimens with different winding densities at 30 °C.

As illustrated in Fig. 8, reducing the winding pitch significantly increases the energy dissipation capacity of the concrete specimens. This effect occurs because closer windings engage the shape memory alloy more effectively during lateral expansion, providing stronger confinement and enhanced post-peak performance. At 30 °C, the total energy dissipated by the specimens with winding pitches of 16 mm, 9 mm, and 5.3 mm is 699 J, 902 J, and 1091 J, respectively, demonstrating a clear trend of improved energy absorption with increasing winding density. This indicates that optimizing the winding configuration can play a crucial role in enhancing both strength and ductility of SMA-confined concrete members.

Fig. 9 illustrates the distribution of von Mises stress within the components and at different cross-sections of the concrete specimens. These images correspond to the moment when the longitudinal strain of the concrete specimens reaches 0.12. Focusing on the stress distribution within the concrete core, it is evident that the winding pitch significantly influences the stress profile. As shown, specimens with shorter winding pitches, or, in other words, more closely spaced windings, can sustain higher stresses at elevated strains. For instance, at a longitudinal strain of 0.12, the maximum stress in the concrete cores for specimens with winding pitches of 16 mm, 9 mm, and 5.3 mm is 37.3, 48.4, and 59.1 MPa, respectively.

Examining a cross-section of the concrete core reveals that the stress near the top and bottom circumferences is close to zero. Similarly, stress near the mid-height of the concrete core is approximately zero. As noted, the primary parameter responsible for these variations in stress distribution is the configuration of the SMA winding. The stress distribution within the windings themselves also varies. Because the mid-height of the concrete cylinder experiences the largest radial strain, the corresponding strain in the SMA is greatest there. However, when the winding pitch is short, i.e., the windings are densely arranged, the radial strain is reduced. Consequently, in specimens with a 5.3 mm winding pitch, both the radial strain and the induced stress in the SMA are lower compared to the other models.

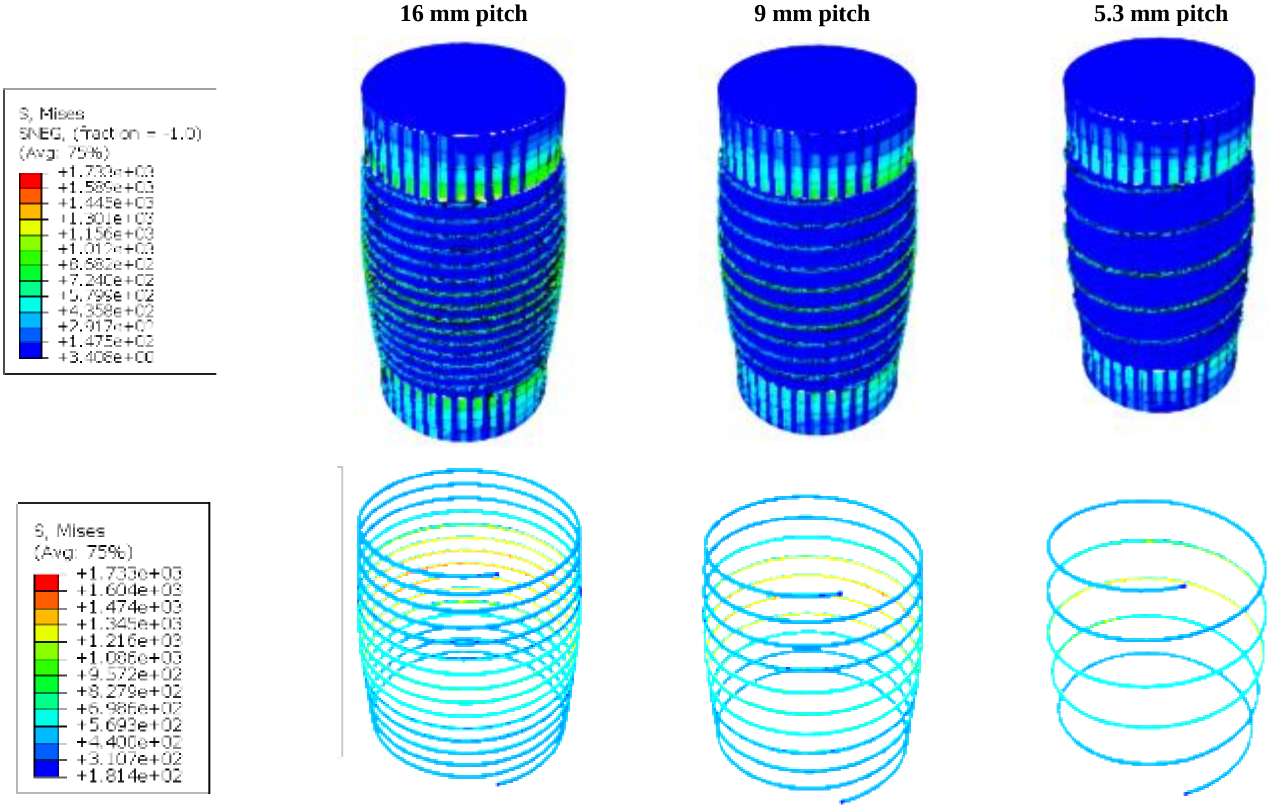

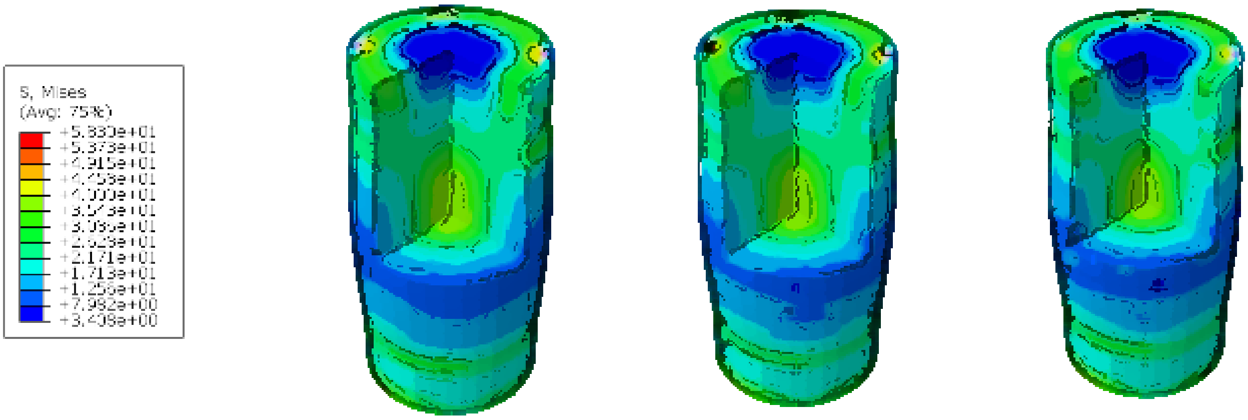

Fig. 9. Concrete specimens with winding pitches of 5.3 mm, 9 mm, and 16 mm at 30 °C.

4.1. Effect of temperature

The behavior of shape memory alloys (SMAs) is directly dependent on temperature. Upon heating, these alloys transform into the austenite phase, which increases their confinement capacity. The models studied in this research involve SMAs with an activation temperature of 30 °C. According to the numerical stress–temperature behavior of the SMAs, the phase transformation is dependent on both stress and temperature.

To investigate the effect of SMA temperature on the winding and overall confinement, in addition to 30 °C, the models were also analyzed at 50 °C, 70 °C, and 90 °C. At these elevated temperatures, the confinement capacity of the SMAs is increased. Fig. 10 illustrates the effect of temperature on confinement for models with winding pitches of 16 mm, 9 mm, and 5.3 mm. As shown, higher SMA temperatures result in greater strength of the concrete specimens at large deformations. On the other hand, the peak compressive strength of the specimens is only minimally affected by temperature, indicating that the peak strength primarily depends on the winding configuration and pitch.

An important observation regarding SMA confinement is that it significantly enhances the concrete's capacity at high strains. Consistent with the results, the stronger the confinement, the greater the increase in strength at elevated strains. This trend can substantially improve the energy absorption capacity of the specimens.

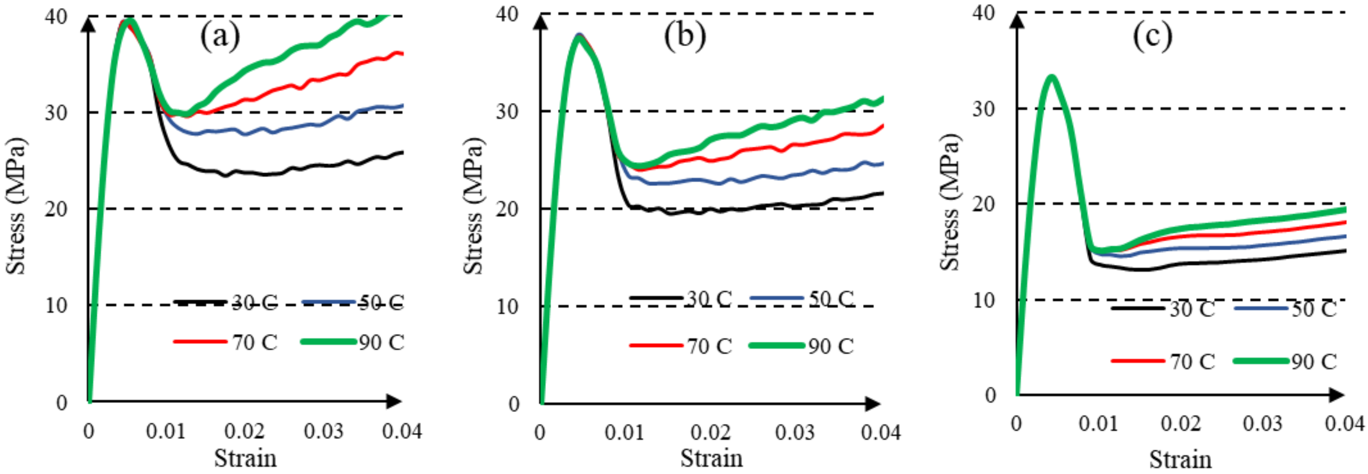

Fig. 10. Compressive stress–strain curves of SMA-confined concrete specimens with winding pitches of (a) 5.3 mm, (b) 9 mm, and (c) 16 mm at different temperatures.

According to Table 2, the energy dissipation capacities of the specimens at different temperatures are presented. Comparison of these data indicates that, as the temperature of the shape memory alloy (SMA) increases, the system's ability to absorb and dissipate energy grows in an approximately linear manner. The corresponding plots for all three concrete models exhibit an upward trend, reflecting the more effective activation of the confining wraps at higher temperatures.

It is noteworthy that the slope of energy growth is not identical across specimens; the degree of wrapping density has a direct influence on this slope. The denser the winding, the greater the rate of increase in energy dissipation with temperature. Specifically, the slopes for specimens with winding pitches of 5.3, 9, and 16 mm are approximately 7.97, 5.46, and 2.85, respectively. This demonstrates that specimens containing a larger volume of SMA exhibit higher sensitivity to temperature changes and greater energy absorption capacity. Such behavior underscores the importance of selecting an appropriate winding pitch when designing systems intended to withstand cyclic and impact loading.

Table 2. Energy absorbed at different temperatures and steps.

winding pitches	30ºC	50ºC	70ºC	90ºC
5.3 mm	1120 J	1272 J	1425 J	1578 J
9 mm	923 J	1025 J	1135 J	1240 J
16 mm	720 J	781 J	828 J	883 J

In Figs. 11 to 13, the stress distribution for specimens with a 16 mm winding pitch at different temperatures is illustrated. These plots clearly indicate that at higher temperatures, the confined concrete specimens sustain greater stress. For instance, at a longitudinal strain of 0.12, the maximum stress reaches about 43 MPa at 90 °C, compared with roughly 37 MPa at 30 °C. From the presented figures, it can be inferred that elevated temperature exerts a direct influence on the stress distribution within the confined concrete, with the most pronounced effects observed in the concrete core itself. As the SMA strength rises with temperature, the lateral expansion of the concrete is reduced. Limiting lateral dilation is critical for confinement effectiveness because uncontrolled expansion accelerates loss of strength and crushing. Consequently, in specimens where the SMA temperature is higher, the alloy delays premature dilation, allowing the core to carry greater stress, as clearly reflected in the figures.

Another notable point is that, in specimens with lower SMA temperatures, the stress at the mid-height of the concrete tends to drop toward zero. This indicates increased local crushing in that region, primarily due to greater lateral strain. As the SMA temperature increases and restrains dilation, stress at mid-height remains farther from zero, signifying improved confinement. Moreover, in models where the winding pitch is tighter, the stress in the core is less prone to drop toward zero, since a greater SMA volume contributes to enhanced thermal sensitivity. For example, in a specimen with a 5.3 mm pitch at 90 °C, the mid-core stress almost never approaches zero.

Stress distribution within the SMA itself also varies. Across all specimens, the SMA segments located near the mid-height experience the highest strain and stress, while those near the top and bottom surfaces are subjected to almost negligible stress. Overall, specimens with denser windings exhibit lower SMA stress under identical strain levels because the load is shared among more wraps. However, with increasing temperature, the trend shifts: specimens at 90 °C display higher stress in the SMA. This is because the elevated temperature enhances the alloy's stiffness; for two identical SMA elements subjected to the same strain, the one at a higher temperature develops greater stress. Since the applied loading is displacement-controlled, all specimens undergo the same axial strain, and radial strain differences remain minor. Consequently, under higher temperatures, the SMA exhibits higher stress, even though radial expansion is slightly reduced, reflecting the thermally enhanced mechanical response.

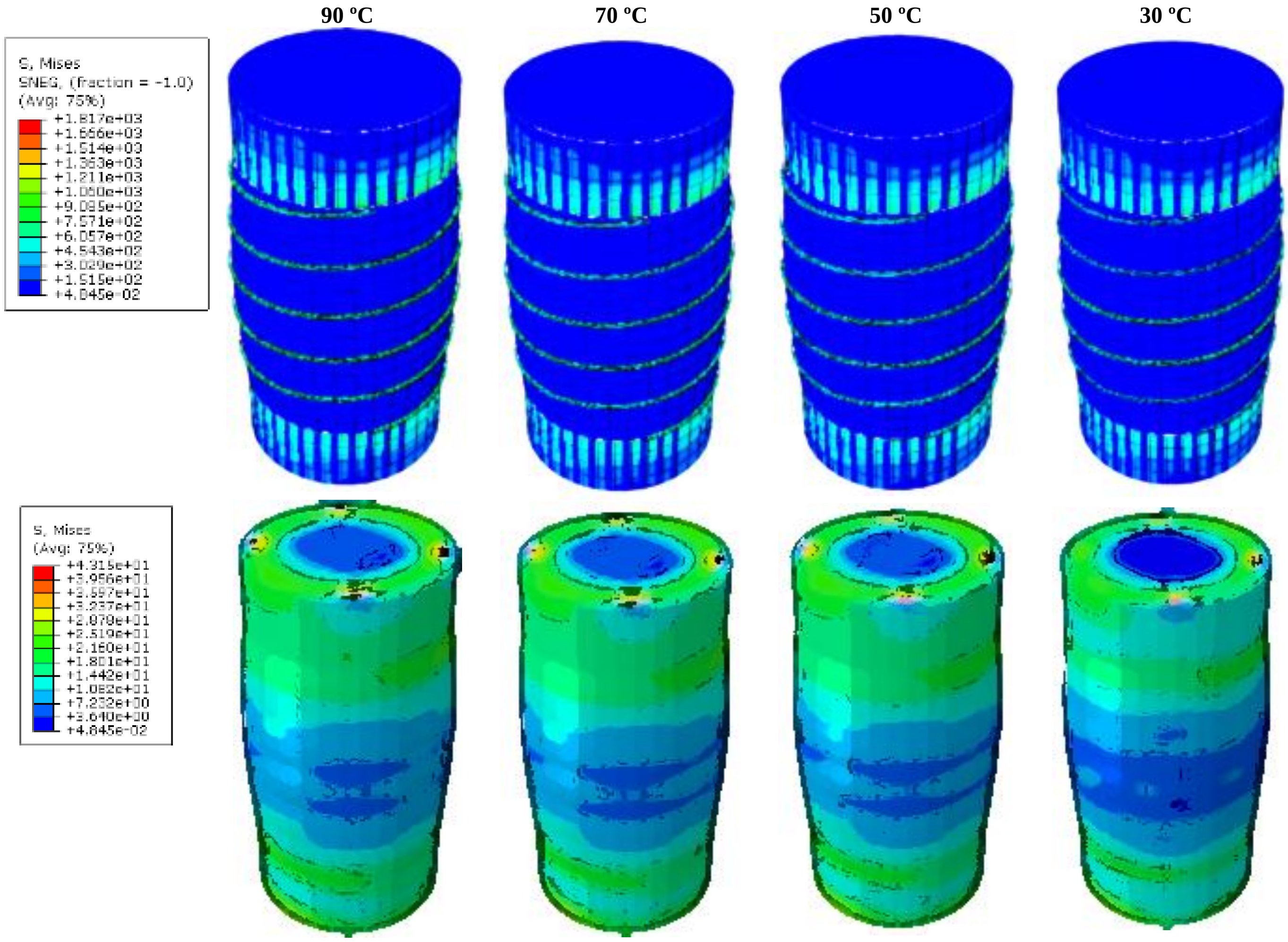

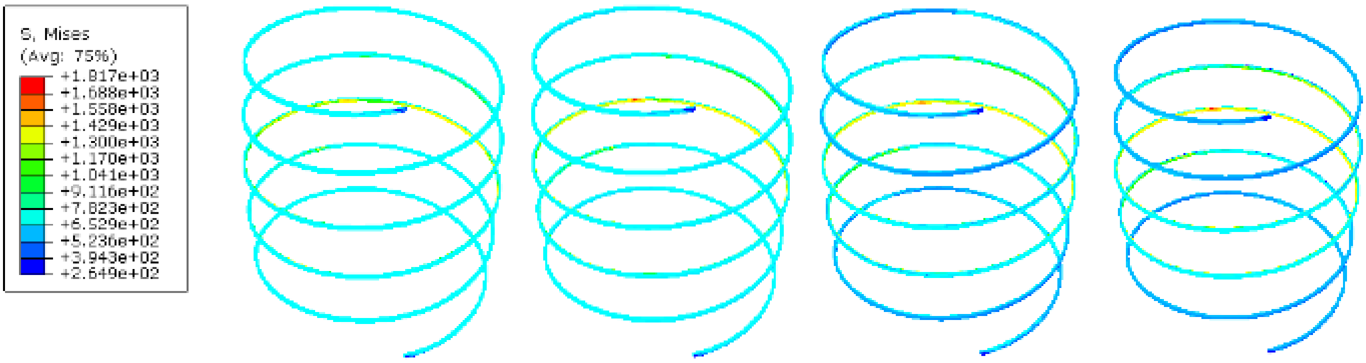

Fig. 11. 16 mm pitch concrete specimens at different temperatures

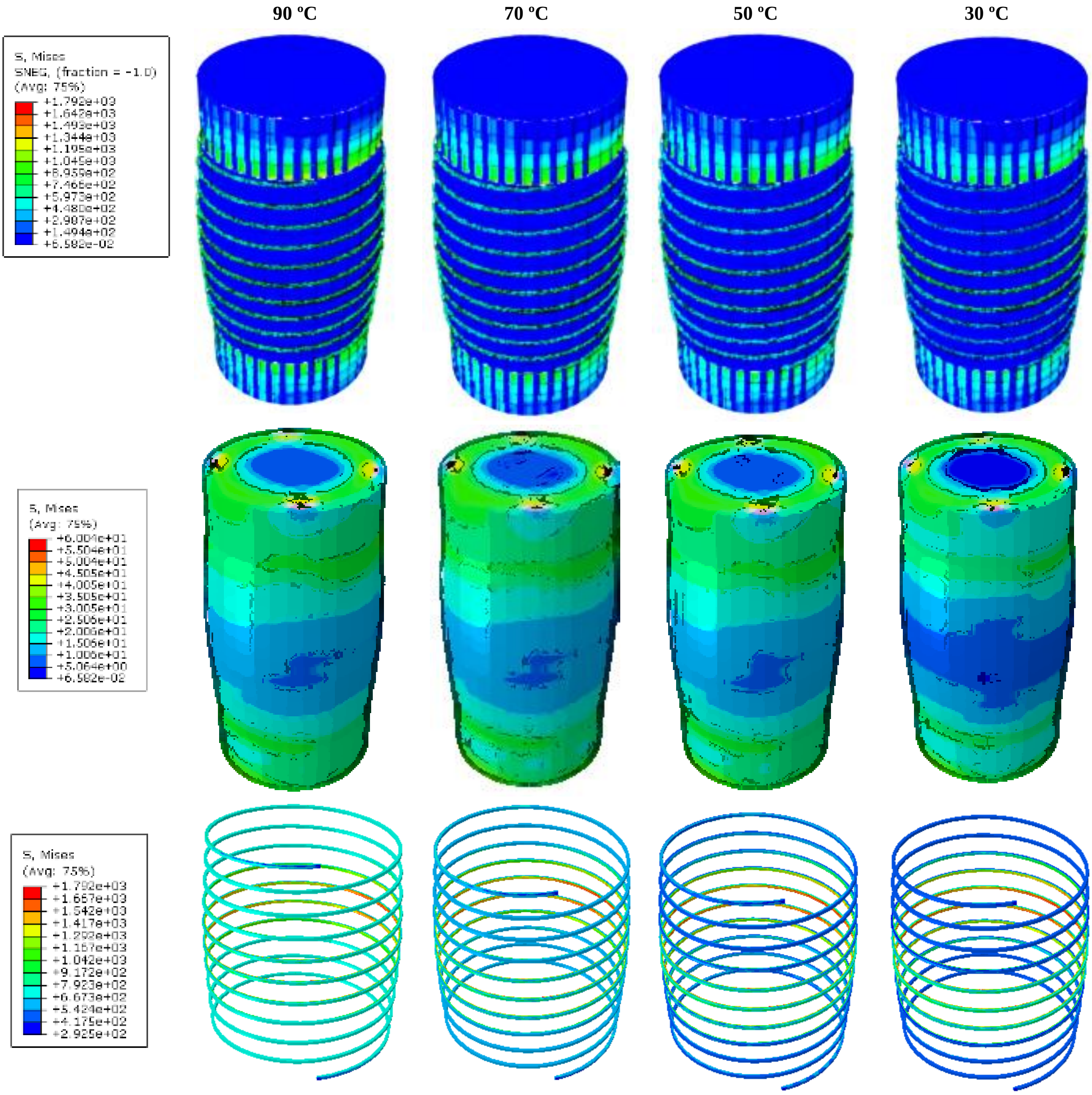

Fig. 12. 9 mm pitch concrete specimens at different temperatures.

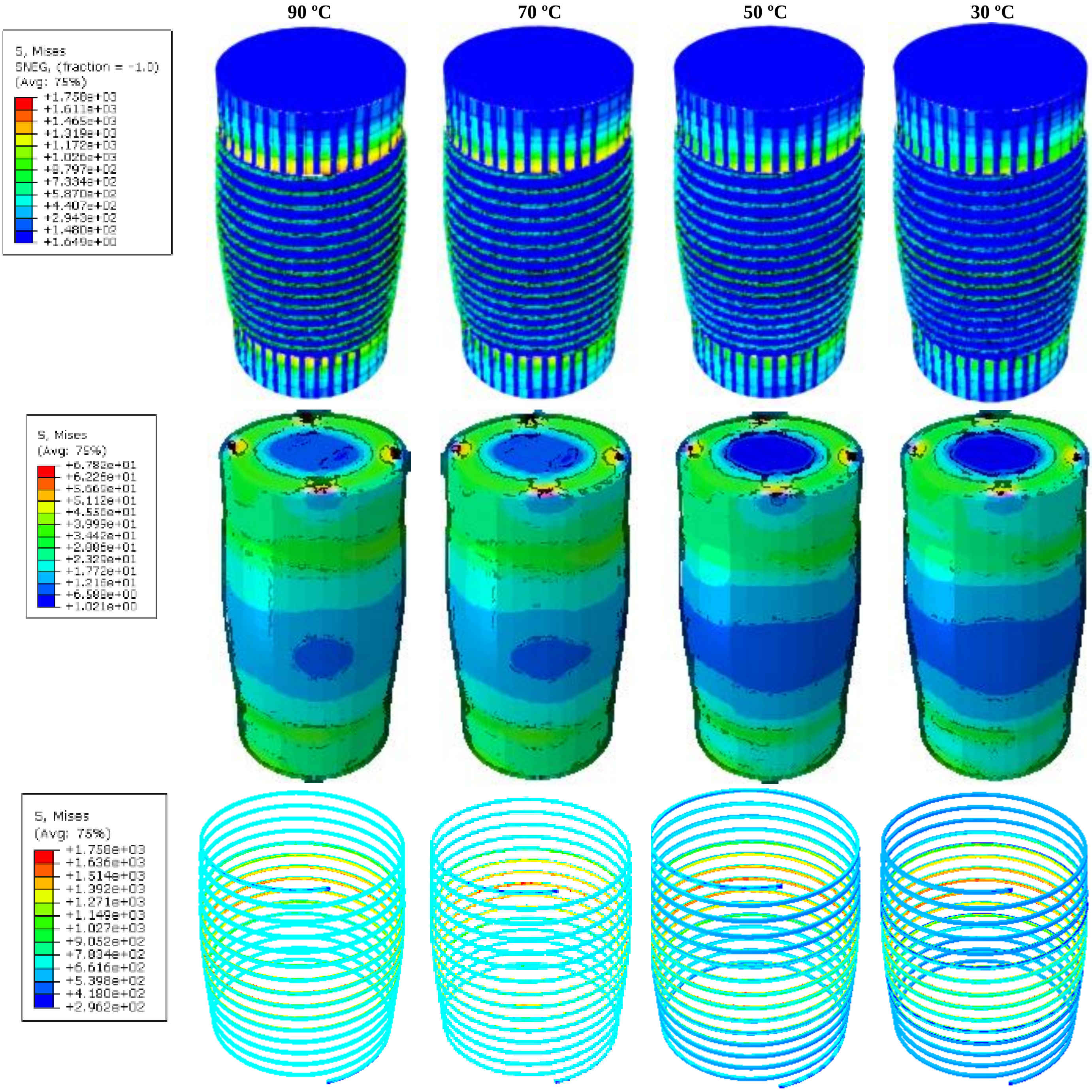

Fig. 13. 5.3 mm pitch concrete specimens at different temperatures.

5. Conclusion

This study numerically investigated the axial behavior of concrete specimens confined with shape memory alloy (SMA) windings using the Concrete Damaged Plasticity (CDP) model in ABAQUS. The main findings are summarized as follows:

1. Model validation:

The proposed FE model, incorporating a user-defined SMA subroutine, accurately reproduced the experimental stress–strain response, including pre-peak stiffness, peak strength, and gradual post-peak softening.

2. Effect of winding pitch:

Decreasing the winding pitch (increasing SMA density) significantly enhanced both the axial strength and the energy dissipation capacity of the confined concrete. At 30 °C, specimens with pitches of 5.3, 9, and 16 mm dissipated 1091 J, 902 J, and 699 J, respectively.

3. Effect of temperature:

Increasing the SMA temperature improved confinement effectiveness at large strains while exerting minimal influence on the peak strength. Elevated temperatures delayed lateral dilation, resulting in higher stress retention and ductility.

4. Stress distribution:

Stress field analysis revealed that denser windings produced more uniform stress profiles across the concrete core and minimized mid-height stress loss, indicating improved confinement uniformity.

5. Thermal sensitivity:

The slope of energy growth with temperature depended on winding density; specimens with greater SMA volume exhibited steeper increases in dissipated energy, confirming the strong thermal responsiveness of tight windings.

6. Practical implications:

SMA-based confinement provides a self-stabilizing and temperature-responsive confinement mechanism that can markedly improve seismic resilience and impact resistance in concrete members.

Future research should address cyclic and fatigue loading, durability under environmental exposure, and scaling effects for large structural elements. Further validation using hybrid SMA–FRP confinement and full-scale column testing is also recommended.

Statements & Declarations

Author contributions

Moein Rezapour: Investigation, Formal analysis, Validation, Resources, Writing - Original Draft, Writing - Review & Editing.

Mehdi Ghassemieh: Conceptualization, Methodology, Project administration, Supervision, Writing - Review & Editing.

Funding

The authors received no financial support for the research, authorship, and/or publication of this article.

Data availability

The data presented in this study will be available on interested request from the corresponding author.

Declarations

The authors declare no conflict of interest.

References

[1] Song, G., Ma, N., Li, H.-N. Applications of shape memory alloys in civil structures. Engineering structures, 2006; 28: 1266-1274. doi:10.1016/j.engstruct.2005.12.010.

[2] Lagoudas, D. C. Shape Memory Alloys. 1st ed. New York (NY): Springer New York; 2008. doi:10.1007/978-0-387-47685-8.

[3] Yamauchi, K., Ohkata, I., Tsuchiya, K., Miyazaki, S. Shape Memory and Superelastic Alloys: Applications and Technologies. 1st ed. Amsterdam (NL): Elsevier; 2011. doi:10.1533/9780857092625.

[4] Rashed, G. Seismic vibration control of frame structure using shape memory alloy, (PhD Thesis). Dhaka (BD): Bangladesh University of Engineering and Technology; 2013.

[5] Choi, E., Nam, T.-h., Cho, S.-C., Chung, Y.-S., Park, T. The behavior of concrete cylinders confined by shape memory alloy wires. Smart Materials and Structures, 2008; 17: 065032. doi:10.1088/0964-1726/17/6/065032.

[6] Shin, M., Andrawes, B. Lateral Cyclic Behavior of Reinforced Concrete Columns Retrofitted with Shape Memory Spirals and FRP Wraps. Journal of Structural Engineering, 2011; 137: 1282-1290. doi:10.1061/(ASCE)ST.1943-541X.0000364.

[7] Andrawes, B., Shin, M., Wierschem, N. Active Confinement of Reinforced Concrete Bridge Columns Using Shape Memory Alloys. Journal of Bridge Engineering, 2010; 15: 81-89. doi:10.1061/(ASCE)BE.1943-5592.000003.

[8] Gholampour, A., Ozbakkaloglu, T. Shape memory alloy (SMA)-confined normal-and high-strength concrete. In: 20th International Conference on Composite Structures: proceedings; 2017; Bologna, Italy. p. 114.

[9] Gholampour, A., Ozbakkaloglu, T. Understanding the compressive behavior of shape memory alloy (SMA)-confined normal-and high-strength concrete. Composite Structures, 2018; 202: 943-953. doi:10.1016/j.compstruct.2018.05.008.

[10] Park, J., Choi, E., Park, K., Kim, H.-T. Comparing the cyclic behavior of concrete cylinders confined by shape memory alloy wireor steel jackets. Smart Materials and Structures, 2011; 20: 094008. doi:10.1088/0964-1726/20/9/094008.

[11] Lee, T., Jeong, S., Woo, U., Choi, H., Jung, D. Experimental Evaluation of Shape Memory Alloy Retrofitting Effect for Circular Concrete Column Using Ultrasonic Pulse Velocity. International Journal of Concrete Structures and Materials, 2023; 17: 13. doi:10.1186/s40069-022-00574-0.

[12] Tran, H., Balandraud, X., Destrebecq, J. Improvement of the mechanical performances of concrete cylinders confined actively or passively by means of SMA wires. Archives of Civil and Mechanical Engineering, 2015; 15: 292-299. doi:10.1016/j.acme.2014.04.009.

[13] Miłek, T. Experimental Determination of Material Boundary Conditions for Computer Simulation of Sheet Metal Deep Drawing Processes. Advances in Science and Technology. Research Journal, 2023; 17: 360-373. doi:10.12913/22998624/172364.

[14] Lee, J., Fenves, G. L. Plastic-Damage Model for Cyclic Loading of Concrete Structures. Journal of engineering mechanics, 1998; 124: 892-900. doi:10.1061/(ASCE)0733-9399(1998)124:8(892.

[15] Martínez-Rueda, J. E., Elnashai, A. S. Confined concrete model under cyclic load. Materials and structures, 1997; 30: 139-147. doi:10.1007/BF02486385.

[16] Dolce, M., Cardone, D. Mechanical behaviour of shape memory alloys for seismic applications 2. Austenite NiTi wires subjected to tension. International journal of mechanical sciences, 2001; 43: 2657-2677. doi:10.1016/S0020-7403(01)00050-9.

[17] Dolce, M., Cardone, D. Mechanical behaviour of shape memory alloys for seismic applications 1. Martensite and austenite NiTi bars subjected to torsion. International journal of mechanical sciences, 2001; 43: 2631-2656. doi:10.1016/S0020-7403(01)00049-2.

[18] Rezapour, M., Ghassemieh, M., Motavalli, M., Shahverdi, M. Numerical Modeling of Unreinforced Masonry Walls Strengthened with Fe-Based Shape Memory Alloy Strips. Materials, 2021; 14: 2961. doi:10.3390/ma14112961.

[19] Ghassemieh, M., Rezapour, M., Sadeghi, V. Effectiveness of the shape memory alloy reinforcement in concrete coupled shear walls. Journal of Intelligent Material Systems and Structures, 2017; 28: 640-652. doi:10.1177/1045389X16657200.

[20] Ocel, J., DesRoches, R., Leon, R. T., Hess, W. G., Krumme, R., Hayes, J. R., Sweeney, S. Steel Beam-Column Connections Using Shape Memory Alloys. Journal of Structural Engineering, 2004; 130: 732-740. doi:10.1061/(ASCE)0733-9445(2004)130:5(73).

[21] Rezapour, M., Ghassemieh, M. Numerical Investigation of Fe-SMA Strengthened Masonry Walls under Lateral Loading. Civil Engineering and Applied Solutions, 2025; 1: 1-15. doi:10.22080/ceas.2025.29594.1022.

[22] Rezapour, M., Ghassemieh, M. Investigating the influence of superelastic dampers on the behavior of double-sided knee braces. Journal of Steel & Structure, 2024; 18: 69-85.

[23] Banihashem, S. M., Rezapour, M., Attarnejad, R., Sanei, M. Evaluating the Effectiveness of a New Self-Centering Damper on a Knee Braced Frame. Shock and Vibration, 2023; 2023: 6335011. doi:10.1155/2023/6335011.

[24] Hashemvand, A. Investigation of Composite Compressive Properties of Concrete Confined with Shape Memory Alloys, (PhD Thesis). Tehran (IR): Tehran university; 2015.

Civil Engineering and Applied Solutions
Research Article
journal homepage: ceas.journals.umz.ac.ir

Investigation of Crack Growth Behavior in Heterogeneous Asphalt Concrete Using FEM Modeling Based on Random Aggregate Generation and Distribution Algorithms

Majid Jebalbarezi Sarbijan [a*], Bahram Shirini [b], Hamed Rooholamini [c]

[a] *Department of Civil Engineering, University of Jiroft, Jiroft, Iran*
[b] *Department of Civil Engineering, University of Bonab, Bonab, Iran*
[c] *Department of Civil Engineering, Hormozgan University, Hormozgan, Iran*

ARTICLE INFO

Keywords:
Mixed-mode I/II stress intensity factors
Two-phase aggregate/mastic asphalt mixtures
Mechanical property effects
SENB specimen

Article history:
Received 21 June 2025
Accepted 03 August 2025
Available online 01 January 2026

ABSTRACT

This study investigates the fracture behavior of asphalt concrete by modeling it as a multiphase material composed of aggregates and mastic. A series of two-dimensional finite element models was developed using a random aggregate generation and distribution algorithm to simulate the heterogeneous microstructure of asphalt mixtures. The generated specimens were analyzed in ABAQUS software, focusing on the evaluation of Mode I and Mode II stress intensity factors (SIFs) and stress distribution in single-edge notched beam (SENB) configurations. The simulation results demonstrate that the spatial distribution of aggregates plays a significant role in determining both the mode and magnitude of SIFs. While the Poisson ratios of the constituents had a negligible effect, their elastic moduli showed a considerable influence on fracture response. As the crack length increased, the stress field became more localized, indicating a shift from distributed elastic deformation to concentrated fracture. Additionally, regions with lower stiffness acted as stress amplifiers, guiding the crack path through weaker zones and intensifying local stress concentrations. These findings underscore the importance of accounting for microstructural heterogeneity in the fracture analysis and design of asphalt mixtures.

1. Introduction

Cracking is a major distress mechanism in asphalt pavements that compromises structural integrity and shortens service life. One critical form of cracking occurs under vehicle loading at low temperatures, where asphalt mixtures exhibit increased stiffness and reduced ductility. Under these conditions, the pavement becomes more brittle and is prone to load-induced cracking, even under standard traffic loads [1-4].

At low temperatures, the ability of the asphalt binder to dissipate energy decreases, leading to the accumulation of tensile and shear stresses under repeated loading. This makes the pavement more susceptible to crack initiation and propagation. To effectively analyze and predict this type of damage, fracture mechanics provides a robust framework. In particular, stress intensity factors (SIFs) offer a means to characterize the stress field at the tip of a crack and assess its potential to grow under given loading conditions.

Asphalt concrete is a heterogeneous material composed of mineral aggregates and asphalt binder. The fracture behavior of such mixtures is influenced by the distribution, size, and mechanical properties of aggregates, as well as the temperature-sensitive behavior of the binder. Consequently, the values of stress intensity factors, and thus the fracture resistance, depend heavily on the microstructural characteristics of the mixture. This highlights the importance of accounting for material heterogeneity when

---

* Corresponding author.
E-mail addresses: m.Jebalbarezi@gmail.com (M. Jebalbarezi Sarbijan).

https://doi.org/10.22080/ceas.2025.29529.1020
ISSN: 3092-7749/© 2026 The Author(s). Published by University of Mazandaran.

How to cite this article: Jebalbarezi Sarbijan, M., Shirini, B., Rooholamini, H. Investigation of Crack Growth Behavior in Heterogeneous Asphalt Concrete Using FEM Modeling Based on Random Aggregate Generation and Distribution Algorithms. Civil Engineering and Applied Solutions. 2026; 2(1): 46–57. doi:10.22080/ceas.2025.29529.1020.

evaluating the low-temperature fracture performance of asphalt pavements under traffic loading.

Numerous studies have been carried out to investigate the fracture behavior of asphalt mixtures using heterogeneous modeling approaches. These studies aim to more accurately capture the effects of microstructural features such as aggregate distribution, shape, and the mechanical properties of both aggregates and mastic. By explicitly representing the heterogeneous nature of asphalt concrete, these models provide deeper insights into crack initiation and propagation mechanisms. In the following, several key studies in this area are briefly reviewed.

Teng et al. [5] performed finite element simulations of single-edge notched asphalt concrete beams using a novel random heterogeneous model calibrated with the Kalman filter. Results showed that lower temperatures led to more vertically inclined cracks, decreased mode I fracture proportion, and increased crack propagation speed in the mastic.

Chen et al. [6] developed a CZM-based finite element model using 3D image-aided heterogeneous structures to investigate asphalt concrete fracture behavior. The model was validated through SCB tests and used to study the effects of temperature, loading rate, aggregate geometry, and fracture properties. Results showed that lower temperatures and angular aggregates increase damage, while higher fracture energy improves load capacity and crack resistance.

Shi et al. [7] developed discrete element models based on 3D-scanned aggregate contours to analyze the meso-mechanical behavior of recycled asphalt mixtures. Their findings showed that RAP content had little effect on skeleton contact points but significantly impacted interfacial stresses and crack development. Shear cracks occurred mainly at RAP interfaces, while tensile cracks dominated in asphalt mortar and aggregate contacts, with higher RAP content reducing rutting resistance.

Zhang et al. [8] investigated the cracking behavior of Semi-Flexible Pavement (SFP) using three-point bending tests and finite element simulations based on a meso-scale heterogeneous model. The study found that increasing the tensile strength of asphalt mortar and asphalt–aggregate interfaces enhanced load capacity but accelerated crack propagation. Higher fracture energy delayed crack growth with diminishing effect, and optimal parameter ranges were recommended to improve SFP crack resistance.

Chen et al. [9] developed a high-resolution 2D finite element model using X-ray CT data and Cohesive Zone Modeling (CZM) to simulate fracture behavior in asphalt mixtures. The model embedded zero-thickness cohesive elements in both asphalt mastic and aggregate interfaces, and accurately predicted crack initiation and growth under fatigue loading. Results showed that crack behavior depends on temperature and material heterogeneity, with cracks initiating in the mastic at 25 °C and at binder–aggregate interfaces at 5 °C.

Lu et al. [10] developed a discrete element method (DEM) model with a novel contact law to simulate the rate- and time-dependent behavior of asphalt concrete. The model integrates viscoelastic and elastoplastic damage mechanisms and naturally captures crack initiation and growth. It was validated against experimental tests such as creep, relaxation, and SCB. The approach offers new insights into the transition from diffuse to localized failure under complex loading.

In another study by Wu et al. [11] the effects of moisture damage on asphalt mixtures were investigated using pull-off tests, SCB tests, and finite element modeling with cohesive zone models. Results showed that water immersion significantly reduced adhesion strength and fracture resistance, leading to earlier crack initiation and increased damage at binder–aggregate interfaces. The combined lab and numerical approach effectively captured moisture-induced degradation across macro and meso scales.

Xue et al. [12] developed a heterogeneous fracture simulation approach using the Discrete Element Method (DEM) and a novel algorithm to model asphalt concrete in SCB tests. A bilinear cohesive model captured crack initiation and propagation, with simulations validated against experiments at various temperatures and NMAS levels. Results showed that aggregate strength, NMAS, and temperature significantly influence crack behavior, with tensile forces being the primary failure mechanism.

Gao et al. [13] studied mix-mode fracture in asphalt concrete using ASCB tests and meso-scale finite element simulations with random aggregates. Results showed that cracks follow paths of least energy, with higher shear proportions increasing strength but reducing crack connectivity. The study revealed detailed meso-scale crack evolution and quantified tensile and shear failure contributions.

Du et al. [14] developed a multiscale finite element model integrating asphalt mixture microstructure and pavement macrostructure to investigate cohesive and adhesive damage in asphalt pavements. The study revealed that heterogeneity causes stress concentrations leading to cracking, and lower adhesive strength at binder-aggregate interfaces significantly contributes to surface-initiated “top-down” cracks.

In another study by Sun et al. [15] developed a microstructure-based multiscale finite element method to analyze the impact of temperature fields on damage initiation in asphalt pavements under traffic loading. Incorporating thermal radiation, convection, and conduction, the model links global pavement and local mixture scales using digital image processing and cohesive zone modeling. Results highlight the critical role of temperature variation in pavement damage and demonstrate the method’s potential for improving performance prediction and pavement design.

Although several previous studies have modeled the fracture behavior of asphalt concrete, many have relied on homogenized or idealized representations of the material microstructure. These approaches often overlook the influence of aggregate morphology, spatial distribution, and localized interactions near the crack tip. The present study addresses this gap by employing a random aggregate generation algorithm to construct heterogeneous SENB specimens and analyze their fracture behavior through finite element modeling. The novelty of this work lies in its systematic investigation of the combined effects of aggregate distribution, crack location, and constituent material properties, particularly under low-temperature conditions, on both Mode I and Mode II stress intensity factors. By explicitly modeling microstructural heterogeneity, this research provides new insights into the fracture resistance mechanisms of asphalt mixtures, offering a more realistic basis for performance prediction and material design.

2. Methodology

Although aggregates are irregularly shaped polygons in reality, modeling and meshing these complex geometries is highly challenging. To overcome this issue, the aggregates in this study were assumed to be circular in shape to simplify the meshing process and reduce computational complexity.

Table 1 presents the gradation of the aggregates used in the asphalt concrete specimens. While the weight percentage of fine aggregates is lower than that of coarse aggregates, the number of fine particles is significantly higher. Therefore, modeling all individual fine aggregates is impractical. To address this, many researchers have modeled only the coarse aggregates explicitly, while representing the fine aggregates, binder, and air voids as a homogeneous mastic phase. For example, Kim et al. [16-18] considered particles larger than 2.36 mm as coarse aggregates. Similarly, Li and Metcalf John [19] defined particles smaller than 4.75 mm as fine aggregates. In this study, aggregates larger than 2.36 mm were considered coarse and were explicitly modeled, while finer particles were included within the mastic matrix. This approach provides a reasonable balance between modeling accuracy and computational efficiency.

MATLAB software was used for the generation and distribution of aggregates. Fig. 1 illustrates the algorithm developed for the random generation and placement of aggregates. In this algorithm, each gradation range from the aggregate gradation table is defined as a separate group. Based on the custom-written MATLAB code, the algorithm first generates a circular aggregate with a random radius according to the specified gradation limits. Then, the generated particle is checked to ensure that it does not overlap with previously placed aggregates and is fully located within the SENB specimen boundaries.

Table 1. Aggregate gradation for asphalt mixture.

Percent passing	Sieve size (mm)
100	19
100-90	12.5
77-44	4.75
58-28	2.36
21-5	0.3
10-2	0.075

3. Geometry

The geometry of the SENB specimen consists of a rectangular asphalt concrete beam with a single notch introduced on one edge. The typical dimensions of the specimen include a length L and height H. In the standard configuration, a notch of length a is centrally located on one edge of the specimen. However, to induce mixed-mode fracture conditions, the notch is shifted horizontally from the mid-span by a distance d, resulting in an asymmetric crack location.

The beam is supported on two rollers placed symmetrically at a span S, and a vertical load is applied at the top surface of the specimen. Due to the eccentric notch, the crack tip experiences both normal (tensile) and tangential (shear) stresses, facilitating the study of combined Mode I/II fracture behavior. The degree of mode mixity is controlled by the notch eccentricity d, notch length a, and the overall dimensions of the specimen.

This geometric modification allows for a relatively simple yet effective experimental setup to investigate the fracture performance of asphalt mixtures under realistic service-like loading conditions. A schematic illustration of the off-center notched SENB specimen is shown in Fig. 2.

4. Modeling

To apply boundary conditions, the vertical movement of the support was constrained, and a vertical load of P = 100 N was applied to the SENB specimen. As shown in Fig. 3, the asphalt mixture was modeled as a composite of coarse aggregates embedded in a mastic matrix. The aggregates were considered to behave as linearly elastic materials, while the mechanical behavior of mastication is known to be temperature-dependent. At elevated temperatures, mastic exhibits viscoelastic behavior, and rutting becomes the dominant mode of pavement failure. Conversely, at subzero temperatures, mastic behaves predominantly as an elastic material, and cracking becomes the principal distress mechanism in asphalt mixtures.

To investigate the influence of the mechanical properties of aggregates and mastic on the crack tip fracture parameters, a two-dimensional meso-structured (two-phase) model was developed and simulated using ABAQUS software. Approximately 250,000 2D CPE8R elements were used to discretize the aggregates and mastic phases. As illustrated in Fig. 4, a refined mesh and singular elements were employed near the crack tip to accurately capture the stress field singularity.

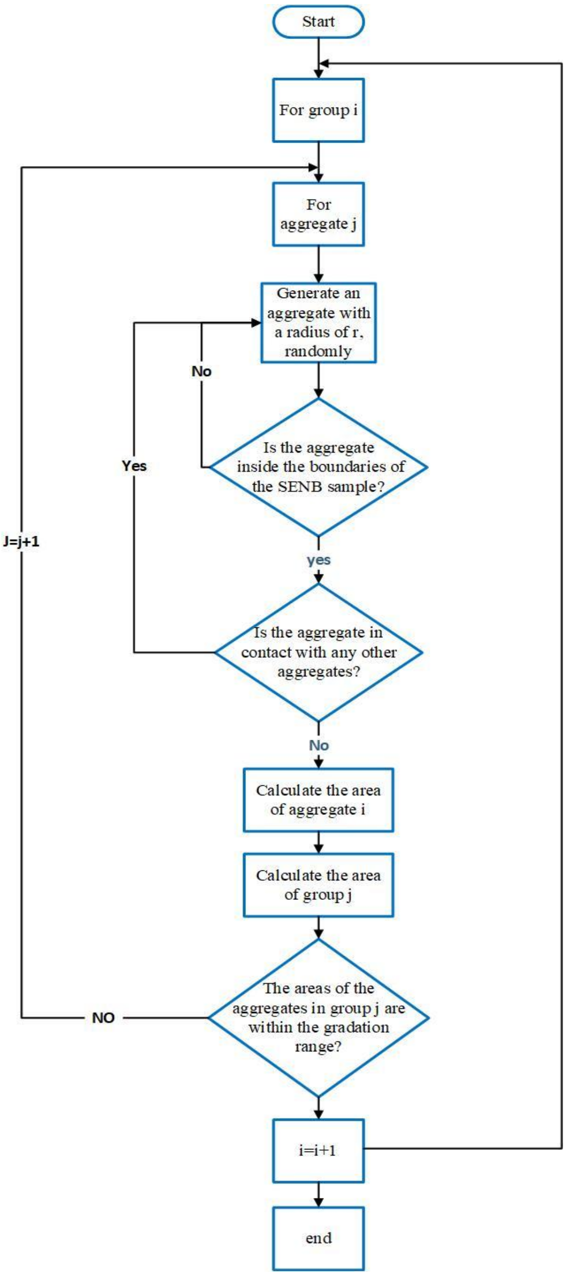

Fig. 1. Flowchart of the aggregate generation and packing algorithm used in asphalt mixture modeling.

Since the focus of this study is on the low-temperature fracture behavior of asphalt mixtures, both aggregate and mastic phases were assumed to behave as linear elastic materials. This assumption is consistent with AASHTO TP105-13 [20] and is widely used in literature for evaluating the critical stress intensity factor (KIC) of cracked asphalt specimens. The mechanical properties used for the aggregate and mastic phases in this study are presented in Table 2 [21-24]. A perfect bond between the two phases was assumed.

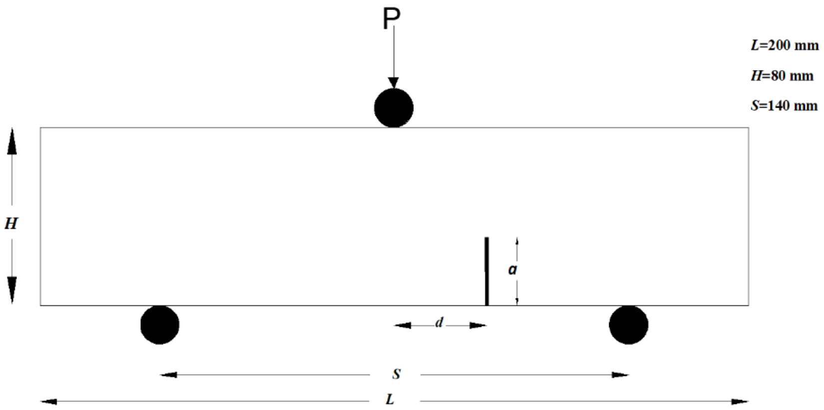

Fig. 2. Single edge notch bending (SENB) specimen subjected to three-point bending load.

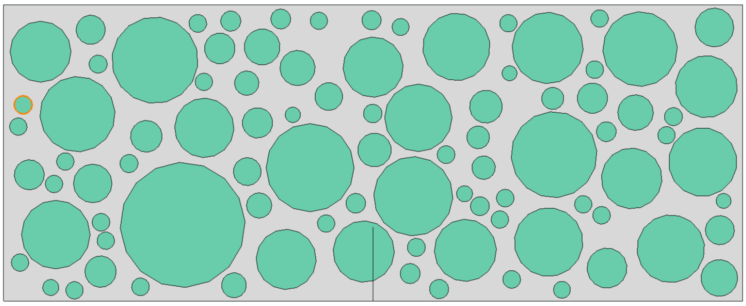

Fig. 3. The generated SENB specimen consisting of two-phase coarse aggregates (green) and mastic matrix (gray).

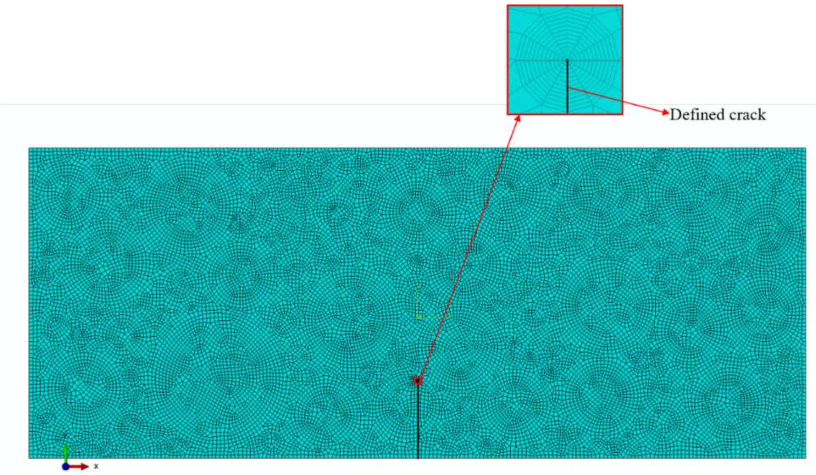

Fig. 4. Finite element representation of the SENB specimen.

Table 2. Different materials are considered as asphalt mixture components at low temperatures

Material	Young's modulus (*E*) (MPa)	Poisson's ratio (*v*)
Coarse aggregates	30000, 50000, 80000	0.05, 0.25, 0.45
Mastic	5000, 10000, 15000, 20000	0.15, 0.25, 0.35

5. Fracture parameters

Williams [25] proposed a series of equations to describe the stress field in the vicinity of a crack tip under mixed-mode loading conditions. The stress components in polar coordinates near the crack tip are expressed as follows:

$$\sigma_{rr} = \frac{1}{\sqrt{2\pi r}}\cos\frac{\theta}{2}\ [K_I\left(1+\sin^2\frac{\theta}{2}\right)+\frac{3}{2}K_{II}\sin\theta-2K_{II}\tan\frac{\theta}{2} \qquad (1)$$

$$\tau_{r\theta} = \frac{1}{2\sqrt{2\pi r}}\cos\frac{\theta}{2}\ [K_I\sin\theta+K_{II}(3cos\theta-1) \qquad (2)$$

$$\sigma_{\theta\theta} = \frac{1}{\sqrt{2\pi r}}\cos\frac{\theta}{2}\ [K_I\cos^2\frac{\theta}{2}-\frac{3}{2}K_{II}\sin\theta] \qquad (3)$$

Here, *r* and *θ* represent the radial distance and angular position relative to the crack tip, respectively. The terms *KI* and *KII* are the mode I and mode II stress intensity factors, which characterize the intensity of the stress field near the crack tip under different loading modes.

The stress distribution around the crack tip is strongly influenced by the material's elastic properties, loading conditions, and crack location. These parameters play a crucial role in predicting crack initiation and propagation directions. For a more accurate assessment of crack growth, factors such as material heterogeneity and aggregate distribution should also be considered.

6. Result

The stress intensity factors (SIFs) for Mode I (*KI*) and Mode II (*KII*) fracture modes were evaluated for several non-homogeneous asphalt specimens with a single-edge notch bending (SENB) configuration. The SIFs were calculated as a function of crack offset distance d from the center of the specimen.

Fig. 5 illustrates the variation of *KI* with respect to crack offset d. It is observed that all heterogeneous samples exhibit a significant dependency on the crack location. In general, *KI* values peak when the crack is located near the center or slightly off-center, and gradually decrease as the crack moves toward the edge of the specimen. Sample 2 shows the highest initial *KI* value, while Sample 3 presents a smoother decline. The homogeneous specimen, in contrast, displays a more consistent and linear reduction in *KI* as d increases, indicating more predictable fracture behavior.

Fig. 5 presents the corresponding *KII* values. The results show that Mode II SIFs are relatively smaller in magnitude compared to Mode I and fluctuate around zero. This suggests the presence of minor shear contributions due to material heterogeneity and crack asymmetry. Samples 1 and 2 show oscillatory trends in *KII*, with peaks and troughs that imply localized shear stress concentrations. Sample 3 maintains values closer to zero, indicating predominantly Mode I behavior. The homogeneous specimen again exhibits the most stable response, with minimal variation in *KII*.

These findings confirm that material heterogeneity significantly influences the fracture behavior of asphalt specimens, particularly affecting Mode I crack propagation. Crack positioning relative to material inhomogeneities plays a crucial role in determining the fracture path and intensity.

According to this figure, the numerical results show significant differences, ranging from 20% to 90%, between the heterogeneous and homogeneous modeling approaches, depending on the type of sample (i.e., the spatial distribution of aggregates within the SENB specimen) and the crack length (i.e., the relative distance between the crack tip and nearby aggregates).

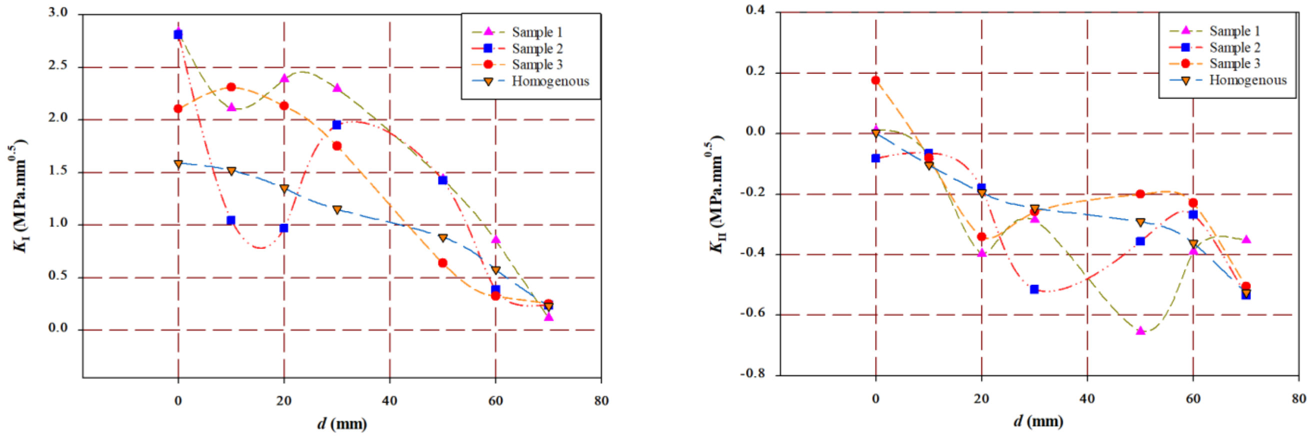

Fig. 5. Stress intensity factor variations (Mode I and Mode II) for a crack located at a distance d from the center of an SENB specimen under different aggregate distributions.

Fig. 6 shows the variation of mode I and mode II stress intensity factors for an SENB (Single Edge Notch Bending) asphalt specimen with varying elastic moduli (*E* = 30, 50, and 80 GPa) of coarse aggregates. The crack offset distance from the center of the specimen, denoted by d, is represented on the horizontal axis, while the corresponding stress intensity factor is plotted on the vertical axis.

It is evident from the figures that for non-homogeneous specimens, as the modulus of elasticity of the aggregates increases, the mode I stress intensity factor (*KI*) increases as well. This behavior is attributed to the fact that aggregates with higher stiffness generate higher stress concentrations around the crack tip. As discussed by Anderson [26] and Lawn [27], the presence of stiff inclusions in a softer matrix leads to an intensification of the stress field near the crack tip, which raises the value of *KI*. In contrast, the homogeneous specimen, which lacks such elastic discontinuities, exhibits the lowest values of *KI*, indicating a more uniform stress distribution [28].

In the case of mode II (*KII*), shown in Fig. 6, the values remain generally lower than mode I but exhibit fluctuations depending on the crack position and the modulus of the aggregates. These fluctuations are caused by mixed-mode interactions and are highly sensitive to the stiffness mismatch, which alters the local shear stress distribution. Similar observations were reported in earlier studies on fractures in heterogeneous materials.

Fig. 7 depicts the influence of Poisson's ratio of the aggregates (0.05, 0.25, and 0.45) on *KI* and *KII*. As Poisson's ratio increases, the *KI* values also increase, particularly when the crack tip is near the center of the specimen. According to Christensen [29], a higher Poisson's ratio results in greater lateral expansion under uniaxial stress, which leads to increased confinement and elevated normal stress near the crack tip, thereby increasing *KI*.

Furthermore, the observed fluctuations in *KII* values with respect to Poisson's ratio can again be linked to the induced local shear stresses and their redistribution around the crack path in a heterogeneous medium. These effects become more pronounced when the crack is located away from the symmetry axis, where asymmetric interactions between the aggregates and the surrounding matrix occur.

These results clearly demonstrate that both the elastic modulus and Poisson's ratio of aggregates significantly influence the stress intensity factors in asphalt mixtures. Therefore, accounting for such heterogeneities is critical in accurately evaluating the fracture behavior of asphaltic composites.

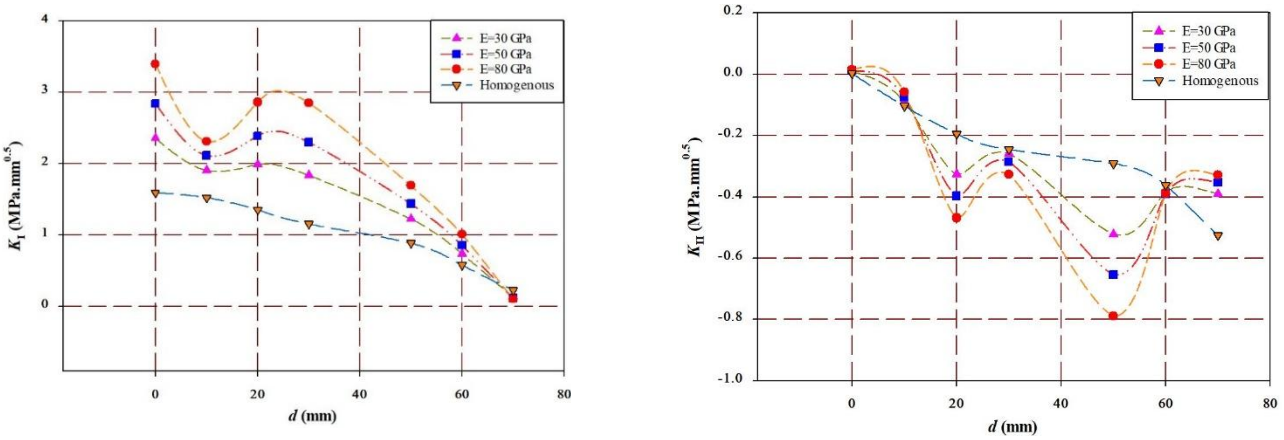

Fig. 6. Effect of aggregate elastic modulus on Mode I and Mode II stress intensity factors.

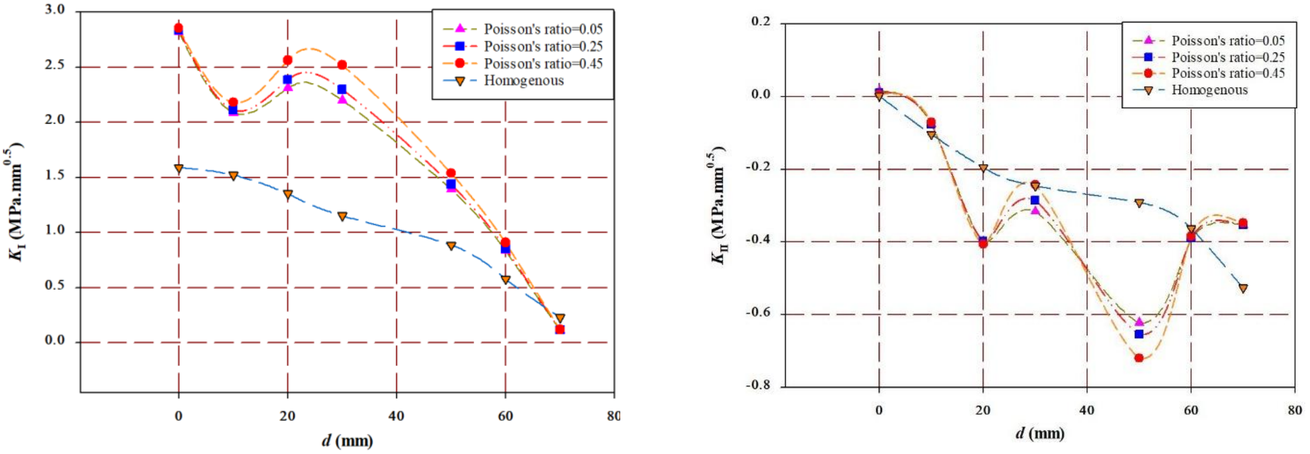

Fig. 7. Effect of Poisson's ratio of aggregates on Mode I and Mode II stress intensity factors.

Fig. 8 displays the variations of *KI* and *KII*, respectively, for mastic elastic moduli of 5, 10, 15, and 20 GPa, compared to a homogeneous model. As shown in Fig. 8, *KI* reaches its maximum near the notch (at $d = 0$) and gradually decreases with increasing distance from the crack tip. Decreasing the mastic modulus leads to a significant increase in Mode I SIF. For example, the peak *KI* for $E = 5$ GPa is approximately twice as high as that for the homogeneous case, indicating that softer mastic phases intensify tensile stress concentration at the crack tip. In contrast, as seen in Fig. 8, *KII* demonstrates an oscillatory pattern with both positive and negative values. Lower elastic modulus results in more pronounced deviations in shear stress, with increased amplitude of *KII* along the crack front. The homogeneous model exhibits a more stable and less fluctuating shear response. These results underscore the substantial role of stiffness mismatch in modulating both tensile and shear stress distributions near the crack tip.

In Fig. 9, the variation of *KI* shows that Poisson's ratio has a relatively moderate effect on Mode I SIF. Although the general trend remains similar across the three values, slightly higher ν values tend to reduce *KI* marginally in the central part of the specimen. This can be attributed to the enhanced lateral contraction resistance in mastics with higher Poisson's ratios.

Fig. 9 reveals that Mode II SIFs are more sensitive to changes in ν. Increasing Poisson's ratio leads to larger fluctuations in *KII*, especially at intermediate distances from the notch. This behavior reflects the impact of transverse strain on shear stress development, indicating that mastic with higher ν values amplifies the nonuniform shear field near the crack tip.

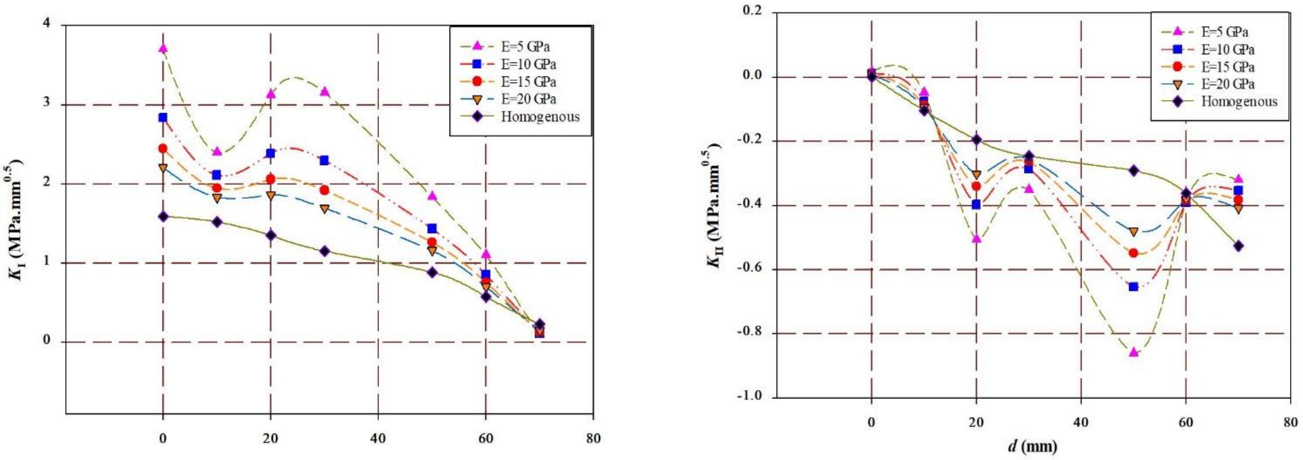

Fig. 8. Effect of mastic elastic modulus on Mode I and Mode II stress intensity factors.

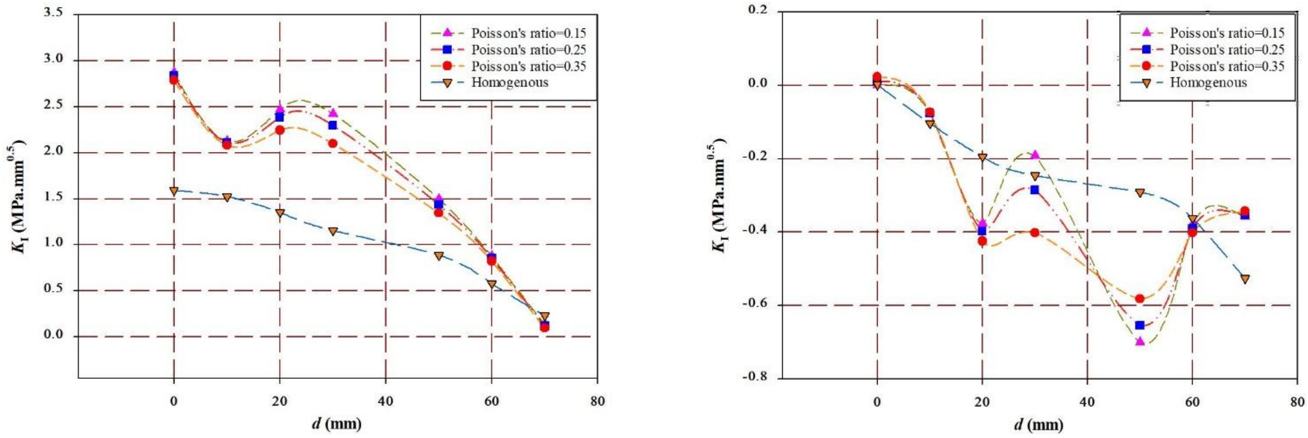

Fig. 9. Effect of Poisson's ratio of mastic on Mode I and Mode II stress intensity factors.

Fig. 10 presents the stress distribution in three different Single Edge Notch Bending (SENB) specimens composed of asphalt materials, modeled with spatial heterogeneity in their mechanical properties. Each specimen exhibits a unique stress field pattern influenced by the non-uniform distribution of stiffness and other material characteristics. The heterogeneous modeling approach captures the inherent variability present in asphalt mixtures, offering a more realistic representation of their fracture behavior.

In all cases, high-stress concentrations are observed near the notch tip, as expected, but their intensity and spread vary significantly among the three configurations. Compared to the homogeneous specimen (Fig. 10), the heterogeneous models reveal more localized and asymmetric stress fields, which are driven by the internal microstructural differences. These localized stress amplifications can lead to premature crack initiation in weaker zones, demonstrating the critical role of material heterogeneity in fracture performance. Moreover, regions with lower stiffness within the heterogeneous models act as preferred paths for crack propagation, confirming that the inclusion of non-uniformity in material properties can have a considerable impact on predicting failure mechanisms in asphalt-based structures.

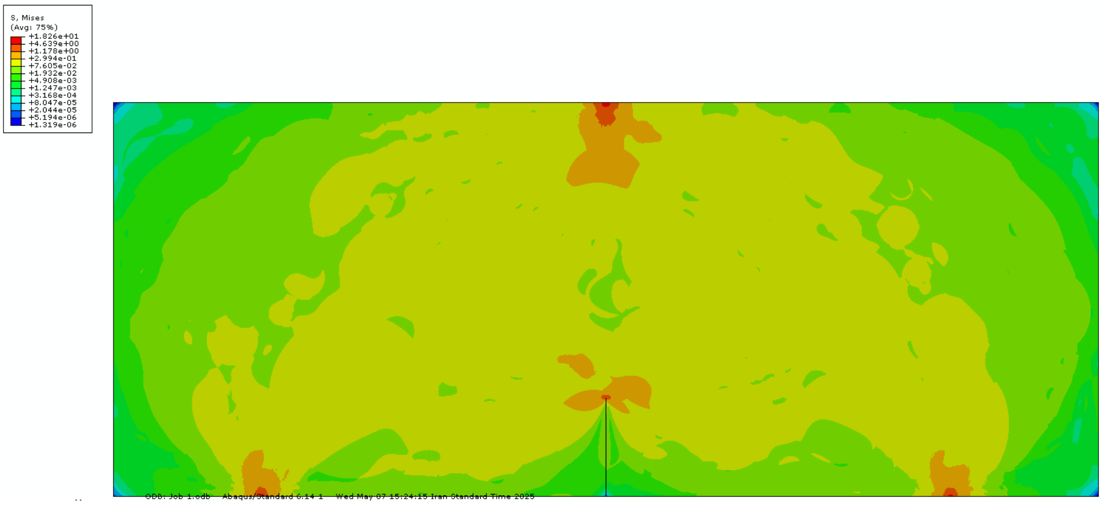

Sample 1

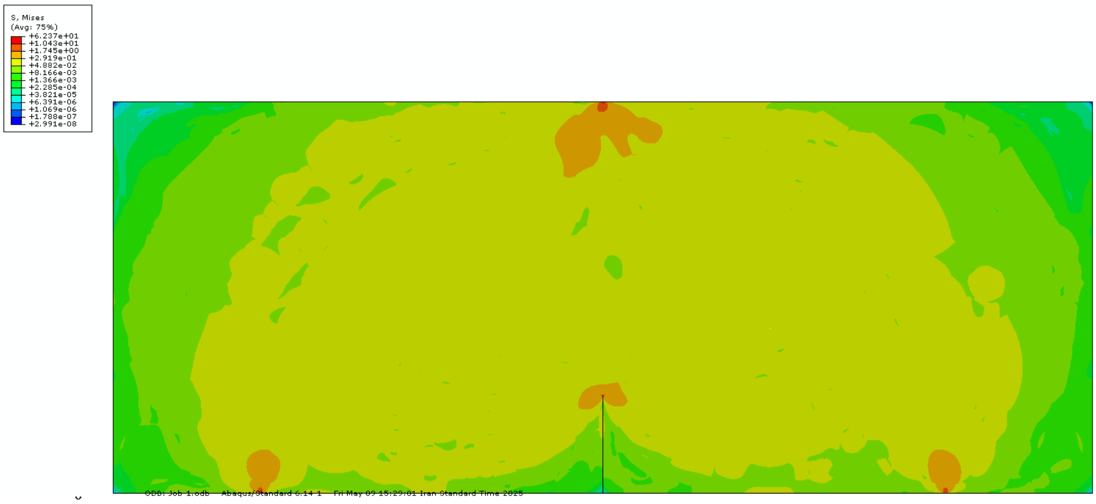

Sample 2

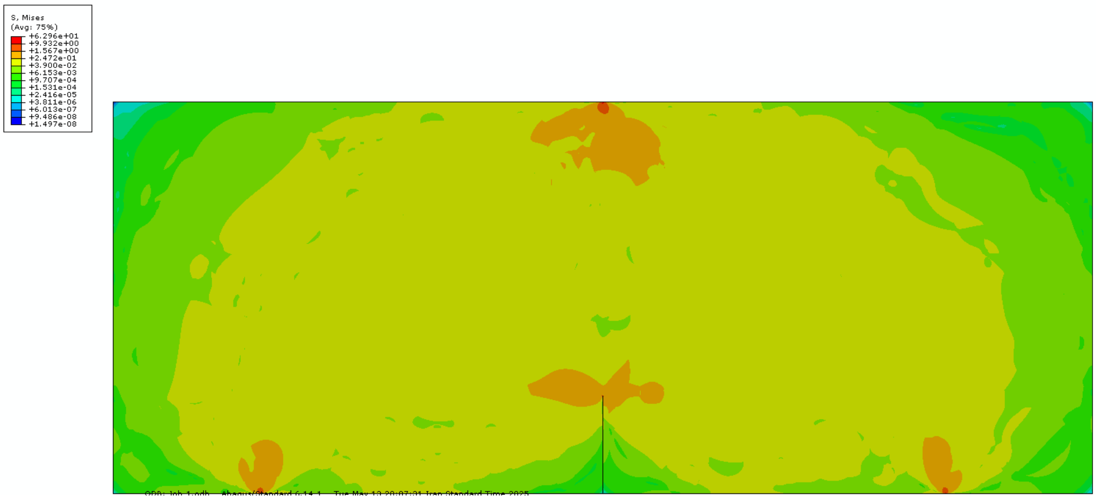

Sample 3

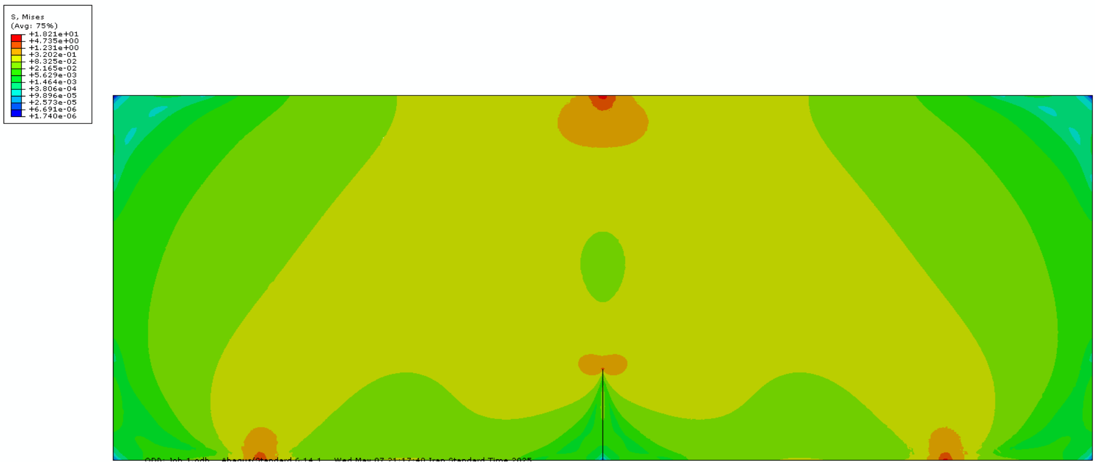

Homogeneous Model

Fig. 10. Stress distribution contours in heterogeneous asphalt specimens modeled using random aggregate generation and distribution algorithm.

Fig. 11 illustrates the stress distribution in a single heterogeneous asphalt SENB specimen at three stages of crack growth—corresponding to crack lengths of 20 mm, 40 mm, and 60 mm. The results reveal clear changes in both the location of stress concentration zones and the overall shape of the stress field as the crack propagates.

At the initial stage with a 20 mm crack (Fig. 11), the stress is primarily concentrated at the notch tip on the lower edge of the specimen. The distribution appears relatively symmetric and broad, indicating a more uniform load-bearing response of the surrounding material. Stress contours spread gradually around the notch, suggesting limited localization.

As the crack extends to 40 mm (Fig. 11), the stress concentration shifts forward along the crack path and becomes more pronounced. The distribution loses its symmetry, becoming elongated and skewed in the direction of crack growth. The high-stress region narrows and intensifies, especially in zones of lower stiffness within the heterogeneous material. These zones act as stress amplifiers, guiding the crack through the weaker areas.

By the time the crack reaches 60 mm (Fig. 11), the stress field becomes sharply localized near the crack tip. The distribution evolves into a narrow, high-intensity peak, reflecting a critical state close to fracture. The stress away from the tip decreases significantly, indicating a transition from distributed elastic deformation to localized failure. The stress contours now align strongly with the crack trajectory, emphasizing the dominant influence of material heterogeneity on fracture direction.

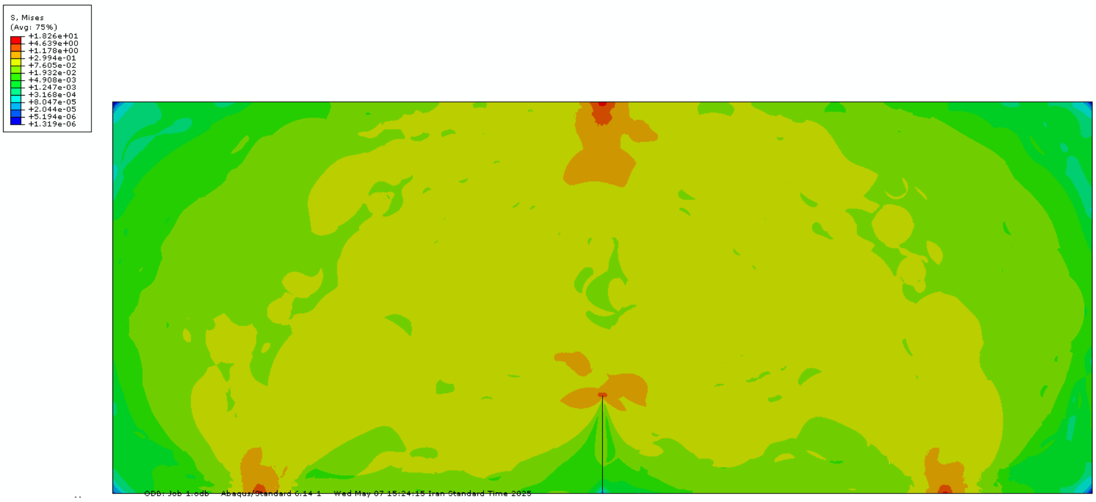

a =20 mm

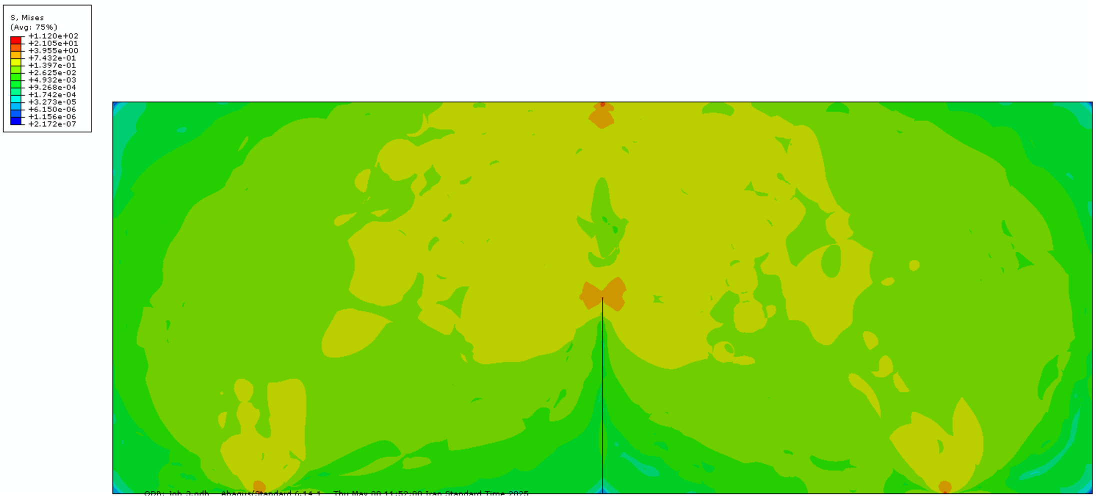

a = 40 mm

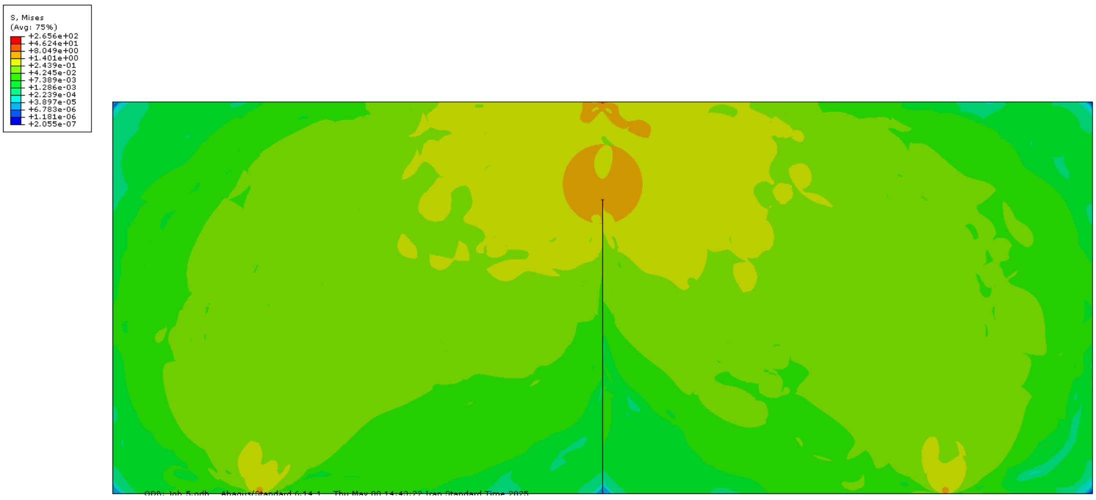

a = 60 mm

Fig. 11. Stress distribution in heterogeneous asphalt specimens for various crack lengths (20 mm, 40 mm, and 60 mm).

7. Conclusion

In this study, the asphalt mixture was modeled as a multiphase material consisting of aggregates and mastic, and its fracture behavior was investigated using a large set of two-dimensional finite element models. To this end, heterogeneous asphalt specimens were numerically generated via a random aggregate generation and distribution algorithm. These models were then analyzed using the ABAQUS finite element software. Mode I and Mode II stress intensity factors (SIFs), along with the stress distribution in a single-edge notched beam (SENB) specimen, were evaluated. Based on the results obtained from the finite element simulations, the following key findings were observed:

- The aggregate distribution significantly influences the fracture behavior of asphalt concrete, particularly the mode and magnitude of stress intensity factors.

- The Poisson ratios of both mastic and aggregates have a minor effect on the stress intensity factors, whereas their elastic moduli exhibit a significant influence.
- As the crack length increases, the stress distribution becomes increasingly asymmetric and focused, highlighting the influence of material heterogeneity on fracture evolution.
- Zones of lower stiffness act as stress amplifiers, redirecting the crack path toward weaker areas and intensifying local stress concentrations.
- With increasing crack length, stress fields evolve from broad and symmetric to narrow and highly localized forms.

Despite these findings, the study involves several simplifying assumptions that introduce limitations. The aggregates were modeled as idealized circular inclusions, which do not capture the irregular geometries of real aggregates. Moreover, a perfect bonding condition was assumed between aggregates and mastic, neglecting potential interfacial debonding or slippage. The analysis was also limited to two-dimensional models, which may not fully capture the three-dimensional stress states present in real asphalt mixtures. Future work will focus on incorporating more realistic aggregate shapes, interface modeling via cohesive zones, and extending the analysis to three-dimensional and coupled thermo-mechanical frameworks for enhanced predictive accuracy.

Statements & Declarations

Author contributions

Majid Jebalbarezi Sarbijan: Investigation, Formal analysis, Validation, Resources, Writing - Original Draft, Writing - Review & Editing.

Bahram Shirini: Investigation, Conceptualization, Methodology, Writing - Review & Editing, Writing - Review & Editing.

Hamed Rooholamini: Investigation, Conceptualization, Methodology, Writing - Review & Editing, Writing - Review & Editing.

Funding

The authors received no financial support for the research, authorship, and/or publication of this article.

Data availability

The data presented in this study will be available on interested request from the corresponding author.

Declarations

The authors declare no conflict of interest.

References

[1] Sarbijan, M. J., Asadi, S., Hamze-Ziabari, S. M. Formulation of stress intensity factor under pure bending condition in multilayer pavements using numerical study and model tree approach. Fatigue & Fracture of Engineering Materials & Structures, 2024; 47: 2506-2520. doi:10.1111/ffe.14314.

[2] Kouzegaran, S., Oliaei, M. Numerical Analysis of the Cellular Geosynthetics Performance in Unpaved Roads and Influencing Factors. Transportation Infrastructure Geotechnology, 2025; 12: 108. doi:10.1007/s40515-024-00500-9.

[3] Aliha, M. R. M., Ziari, H., Sobhani Fard, E., Jebalbarezi Sarbijan, M. Heterogeneity effect on fracture parameters of a multilayer asphalt pavement structure containing a top-down crack and subjected to moving traffic loading. Fatigue & Fracture of Engineering Materials & Structures, 2021; 44: 1349-1371. doi:10.1111/ffe.13434.

[4] Aliha, M. R. M., Ziari, H., Mojaradi, B., Sarbijan, M. J. Heterogeneity effects on mixed-mode I/II stress intensity factors and fracture path of laboratory asphalt mixtures in the shape of SCB specimen. Fatigue & Fracture of Engineering Materials & Structures, 2020; 43: 586-604. doi:10.1111/ffe.13154.

[5] Teng, G., Zheng, C., Chen, X., Lan, X., Zhu, Y., Shan, C. Numerical fracture investigation of single-edge notched asphalt concrete beam based on random heterogeneous FEM model. Construction and Building Materials, 2021; 304: 124581. doi:10.1016/j.conbuildmat.2021.124581.

[6] Chen, J., Ouyang, X., Sun, X. Numerical Investigation of Asphalt Concrete Fracture Based on Heterogeneous Structure and Cohesive Zone Model. Applied Sciences, 2022; 12: doi:10.3390/app122111150.

[7] Shi, L., Wang, Y., Li, H., Liang, H., Lin, B., Wang, D. Recycled asphalt mixture's discrete element model-based composite structure and mesoscale-mechanical properties. Case Studies in Construction Materials, 2023; 18: e01987. doi:10.1016/j.cscm.2023.e01987.

[8] Zhang, L., Zhou, S., Xiong, Z., Mo, Z., Lu, Q., Hong, J. Research on the crack resistance of semi-flexible pavement mixture based on meso-heterogeneous model. Construction and Building Materials, 2024; 411: 134495. doi:10.1016/j.conbuildmat.2023.134495.

[9] Chen, A., Airey, G. D., Thom, N., Li, Y., Wan, L. Simulation of micro-crack initiation and propagation under repeated load in asphalt concrete using zero-thickness cohesive elements. Construction and Building Materials, 2022; 342: 127934. doi:10.1016/j.conbuildmat.2022.127934.

[10] Lu, D. X., Nguyen, N. H. T., Bui, H. H. A cohesive viscoelastic-elastoplastic-damage model for DEM and its applications to predict the rate- and time-dependent behaviour of asphalt concretes. International Journal of Plasticity, 2022; 157: 103391. doi:10.1016/j.ijplas.2022.103391.

[11] Wu, H., Li, Q., Song, W., Chen, X., Wada, S. A., Liao, H. Meso-mechanical characterization on thermal damage and low-temperature cracking of asphalt mixtures. Engineering Fracture Mechanics, 2025; 316: 110862. doi:10.1016/j.engfracmech.2025.110862.

[12] Xue, B., Pei, J., Zhou, B., Zhang, J., Li, R., Guo, F. Using random heterogeneous DEM model to simulate the SCB fracture behavior of asphalt concrete. Construction and Building Materials, 2020; 236: 117580. doi:10.1016/j.conbuildmat.2019.117580.

[13] Gao, L., Zhou, Y., Jiang, J., Yang, Y., Kong, H. Mix-mode fracture behavior in asphalt concrete: Asymmetric semi-circular bending testing and random aggregate generation-based modelling. Construction and Building Materials, 2024; 438: 137225. doi:10.1016/j.conbuildmat.2024.137225.

[14] Du, C., Sun, Y., Chen, J., Gong, H., Wei, X., Zhang, Z. Analysis of cohesive and adhesive damage initiations of asphalt pavement using a microstructure-based finite element model. Construction and Building Materials, 2020; 261: 119973. doi:10.1016/j.conbuildmat.2020.119973.

[15] Sun, Y., Du, C., Gong, H., Li, Y., Chen, J. Effect of temperature field on damage initiation in asphalt pavement: A microstructure-based multiscale finite element method. Mechanics of Materials, 2020; 144: 103367. doi:10.1016/j.mechmat.2020.103367.

[16] Kim, H., Buttlar, W. G. Multi-scale fracture modeling of asphalt composite structures. Composites Science and Technology, 2009; 69: 2716-2723. doi:10.1016/j.compscitech.2009.08.014.

[17] Kim, H., Wagoner Michael, P., Buttlar William, G. Simulation of Fracture Behavior in Asphalt Concrete Using a Heterogeneous Cohesive Zone Discrete Element Model. Journal of Materials in Civil Engineering, 2008; 20: 552-563. doi:10.1061/(ASCE)0899-1561(2008)20:8(552).

[18] Kim, H., Wagoner, M. P., Buttlar, W. G. Micromechanical fracture modeling of asphalt concrete using a single-edge notched beam test. Materials and Structures, 2009; 42: 677-689. doi:10.1617/s11527-008-9412-8.

[19] Li, Y., Metcalf John, B. Two-Step Approach to Prediction of Asphalt Concrete Modulus from Two-Phase Micromechanical Models. Journal of Materials in Civil Engineering, 2005; 17: 407-415. doi:10.1061/(ASCE)0899-1561(2005)17:4(407).

[20] American Association of State Highway and Transportation Officials (AASHTO). AASHTO TP105-13: Standard Method of Test for Determining the Fracture Energy of Asphalt Mixtures Using the Semicircular Bend Geometry (SCB). Washington, D.C. (US): AASHTO;

[21] Mull, M. A., Stuart, K., Yehia, A. Fracture resistance characterization of chemically modified crumb rubber asphalt pavement. Journal of Materials Science, 2002; 37: 557-566. doi:10.1023/A:1013721708572.

[22] Eissa, E. A., Kazi, A. Relation between static and dynamic Young's moduli of rocks. International Journal of Rock Mechanics and Mining Sciences & Geomechanics Abstracts, 1988; 25: 479-482. doi:10.1016/0148-9062(88)90987-4.

[23] Alanazi, N., Kassem, E., Grasley, Z., Bayomy, F. Evaluation of viscoelastic Poisson’s ratio of asphalt mixtures. International Journal of Pavement Engineering, 2019; 20: 1231-1238. doi:10.1080/10298436.2017.1398550.

[24] Gercek, H. Poisson's ratio values for rocks. International Journal of Rock Mechanics and Mining Sciences, 2007; 44: 1-13. doi:10.1016/j.ijrmms.2006.04.011.

[25] Williams, M. L. On the Stress Distribution at the Base of a Stationary Crack. Journal of Applied Mechanics, 2021; 24: 109-114. doi:10.1115/1.4011454.

[26] Anderson, T. L. Fracture Mechanics: Fundamentals and applications. 4th ed. Boca Raton (FL): CRC Press; 2017. doi:10.1201/9781315370293.

[27] Lawn, B. Fracture of Brittle Solids. 2nd ed. Cambridge (UK): Cambridge University Press; 1993. doi:10.1017/CBO9780511623127.

[28] Broek, D. Elementary engineering fracture mechanics. 1st ed. Berlin (DE): Springer Science & Business Media; 1982. doi:10.1007/978-94-009-4333-9.

[29] Christensen, R. M. Mechanics of Composite Materials. 1st ed. Mineola (NY): Dover Publications; 2005.

Civil Engineering and Applied Solutions, 2026; 2(1): 58–73

Civil Engineering and Applied Solutions

Research Article

journal homepage: ceas.journals.umz.ac.ir

Experimental and Numerical Investigation of Landfill Leachate Emission in Unsaturated Sandy Soils

Narges Soleimanian [a], Ali Akhtarpour [a*], Mohammad Saleh Baradaran [a]

[a] *Department of Civil Engineering, Faculty of Engineering, Ferdowsi University of Mashhad, Iran*

ARTICLE INFO

Keywords:
Unsaturated soil
Municipal landfill leachate
Emission pattern
Image analysis
Finite element modeling

Article history:
Received 14 July 2025
Accepted 24 July 2025
Available online 01 January 2026

ABSTRACT

This research represents a novel investigation into the infiltration of municipal waste landfill leachate into unsaturated sandy soil, with a particular focus on the propagation of pollutants. The significance of understanding pollutant emission in unsaturated soil is importance due to its profound environmental impact on ecosystems and its potential challenges to infrastructure development. The study examines key parameters, emphasizing initial matric suction and permeability, using both numerical and laboratory modeling techniques to compare pollutant emission under various conditions, including unsaturated soil in drying path and initially dry soil. Results reveal soil properties (density, permeability, water content) profoundly influence pollutant penetration. Advanced image processing estimates pollutant concentrations at different depths, offering accurate insights. The results derived from the image analysis were then compared with the outcomes obtained from the numerical modeling. This innovative approach holds promise for future applications and environmental monitoring. Findings aid strategies to mitigate landfill leachate effects, informing pollutant containment and prevention in unsaturated soil for sustainable environmental management.

1. Introduction

As urbanization accelerates, the growing prevalence of impermeable surfaces in infrastructures has sparked significant concerns regarding environmental sustainability [1]. These surfaces, which hinder water from naturally permeating into the soil, create an environment where pollutants and chemicals accumulated on the surface can easily infiltrate groundwater reserves. This disruption of natural water flow not only threatens the quality of underground water but also endangers aquatic ecosystems and poses risks to public health . The pollution of both groundwater and soil by contaminants, such as petroleum products and waste leachate, has emerged as a critical environmental challenge worldwide [2].

In this context, it becomes crucial to emphasize the importance of sustainability in all aspects of infrastructure development [3-5], especially in the construction of roads [6], soil stabilization [7], and concrete structures. By integrating sustainable practices into the design and construction of roads and infrastructures [8, 9], we can promote the natural infiltration of water, reduce environmental degradation, and improve the long-term resilience of urban spaces [10, 11]. Sustainable construction techniques, such as permeable pavements, eco-friendly soil treatment methods, and the use of environmentally responsible materials, are vital in mitigating the negative impact of urban development on the environment [12-14].

Incorporating these sustainable practices into the broader framework of urban planning and infrastructure development will ensure that infrastructures not only support economic growth but also protect natural resources, promote ecological balance, and improve the quality of life for urban populations [15, 16].

Pollution of underground water resources and soils by pollutants like petroleum products and waste leachate has become a major

---

* Corresponding author.
E-mail addresses: akhtarpour@um.ac.ir (A. Akhtarpour).

https://doi.org/10.22080/ceas.2025.29684.1028

How to cite this article: Soleimanian, N., Akhtarpour, A., Baradaran, M. S. Experimental and Numerical Investigation of Landfill Leachate Emission in Unsaturated Sandy Soils. Civil Engineering and Applied Solutions. 2026; 2(1): 58–73. doi:10.22080/ceas.2025.29684.1028.

global environmental issue. Soil contamination not only affects underground water tables but also impacts environmental geotechnics. Physical-chemical interactions between soil and pollutants can alter soil resistance, permeability, and compressibility, causing further problems. As pollutants move through unsaturated soil to groundwater, studies must consider unsaturated conditions. Investigating pollutant diffusion in subsurface soils and groundwater is crucial due to their potential widespread entry [17]. Effective rehabilitation of contaminated sites requires understanding pollutant behavior and propagation in subsurface layers. Identifying pollutant emission ranges is the first step in mitigating environmental damage [18, 19]. Knowledge of pollutant movement and accumulation is vital, considering the non-linear nature of fluid transfer in porous, heterogeneous environments [20]. Due to the complexity of factors involved, simple analytical solutions are not feasible at an executive scale.

Eltarabily and Negm [21] studied nitrate movement in different soils, including sandy ones, and evaluated vertical barriers for controlling contamination using FEM model. They found that soil properties significantly affect contaminant movement. They determined the best location and depth for installing sheet pile barriers to minimize contamination reaching groundwater. Szymański et al. [22] stated that closed municipal and industrial waste landfill sites can pollute groundwater. A landfill substratum can filter out pollutants. They research tests with a sand bed showed that filtration efficiency depends on pollutant mass, leachate intensity, and layer thickness. This method helps estimate safe filtration layer thickness. Sharma et al. [23] study quantifies leachate pollution and its effects on groundwater near four nonengineered dump sites in India. It assesses leachate and groundwater using the leachate pollution index (LPI), water quality index (WQI), and heavy metal pollution index (HPI). Results show high pollution levels, with water quality improving downstream. Principal component analysis (PCA) and hierarchical cluster analysis (HCA) identify pollution sources and zones. Javahershenas et al. [24] study assessed surface and groundwater pollution in Lahijan, over 9 months by landfill leachate. Parameters measured included temperature, turbidity, pH, COD, BOD5, metals, and ions. Results indicated elevated levels in the seasonal river, impacting water quality adversely according to the Water Quality Index.

Alghamdi et al. [25] assessed environmental risks associated with leachate from a landfill in Saudi Arabia. They analyzed leachate, groundwater, and soil samples for toxic elements, pH, EC, NO^{3-}, and E. coli. Results showed high concentrations of Fe, Mn, and Zn in leachate, unfit water for irrigation and drinking due to elevated metals and NO^{3-}, and significant soil contamination. The findings underscore the need for improved landfill management to mitigate environmental impacts. Hussein et al. [26] analyzed heavy metal contamination in leachate and surface soils from Malaysian landfills, highlighting significant threats to human health and the environment. Elevated As and Cr levels in leachate indicate progressive contamination. Non-sanitary, unlined landfills show higher metal concentrations compared to background levels. Indexes like Igeo, PI, and IPI confirm moderate to strong pollution in these areas, emphasizing the need for better landfill management to mitigate environmental impacts. Nyika et al. [27] investigates landfill leachate in South Africa, highlighting its potential to pollute groundwater due to high levels of conductivity, dissolved solids, and various ions exceeding WHO and SANS standards for drinking water. The leachate's pH of 4.7 renders it unsuitable for domestic use. Groundwater samples from different boreholes indicated contamination with metals and ions, attributed to decomposed waste infiltrating the resource. Recommendations include regular groundwater monitoring due to slow and unpredictable leachate movement. Alao [28] examines dumpsite leachate effects on soil and groundwater using geophysical and chemical analyses. Findings reveal widespread contamination, emphasizing urgent monitoring and remediation needs to protect groundwater. Depths below 23 meters are identified as potential sources of clean water amid compromised aquifers. Zango et al. [29] investigates the impact of enzymatic induced calcium carbonate precipitation (EICP), or biocementation, on fine-grained soil's hydraulic conductivity using digital image techniques (DIT). Results indicate EICP significantly alters leachate penetration patterns and reduces hydraulic conductivity. By the end of 28 days, treated soils saw reductions of 28.83% and 41.33% in hydraulic conductivity compared to untreated soil.

This research includes three laboratory parts, numerical modeling and image processing (Fig. 1). In the laboratory section, the distribution of municipal waste leachate in samples with different densities in two unsaturated and dry states has been investigated. In the numerical modeling section, SEEP/W and CTRAN/W packages from Geostudio software have been used to validate the samples made in the laboratory. In this way, the effect of the parameters affecting the transfer of pollutants in the soil environment such as the change in the underground water level, the relative density of the pollutant and the change in the dispersion coefficients have been investigated. In the third part, the image processing method was used to estimate the concentration of pollution in the soil so that by knowing the type of soil in real conditions, the concentration and diffusion process of the pollutant in the porous environment of the soil can be estimated relatively accurately and the results was compared with numerical modeling. It should be noted that the innovation of the present research is in 2 parts, investigating diffusion in unsaturated soil and using the image processing method in different concentrations.

2. Materials

2.1. Soil properties

In the current research, in order to test and investigate the effects of leachate contamination in the soil, the standard Firoozkooh No.131 sand has been used. Table 1 shows the geotechnical and chemical characteristics of this soil. Also, grain size distributions of this sand are given in Fig. 2.

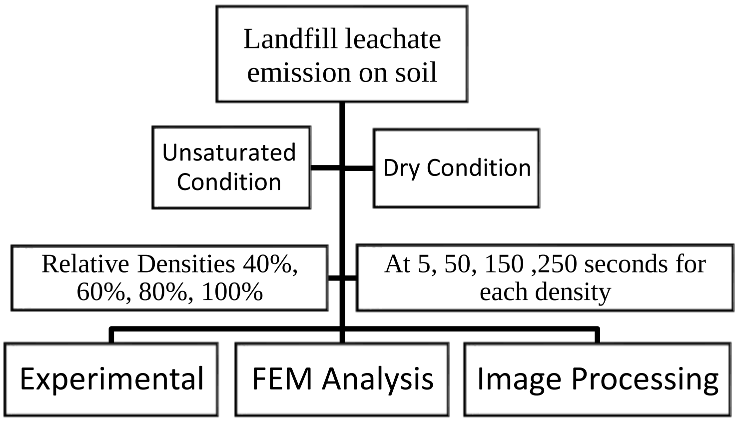

Fig. 1. Flowchart of research process.

Table 1. Geotechnical-chemical characteristics of firoozkooh No.131 sand [30, 31].

Geotechnical specifications	e_{max}	e_{min}	G_s	D_{50}	D_{10}	D_{60}
	1.091	0.710	2.656	0.65	0.45	0.67
Chemical characteristics (%)	SiO_2	Al_2O_3	Fe_2O_3	CaO	Na_2O	K_2O
	98.1	1.1	0.1	0.06	0.5	0.5

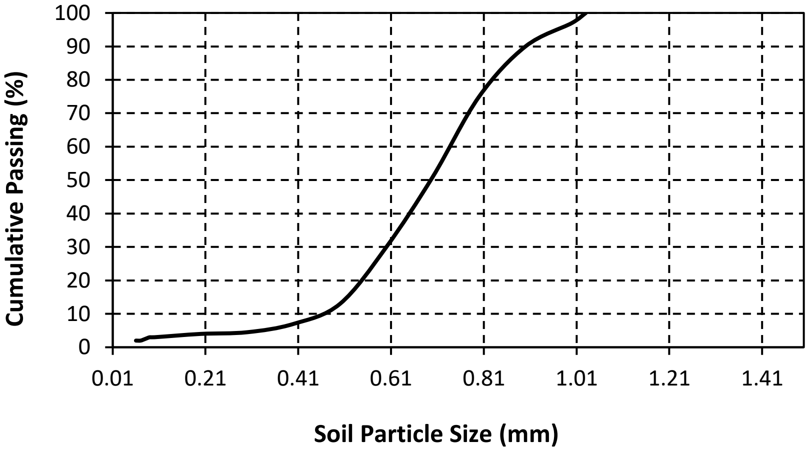

Fig. 2. Soil gradation curve of Firoozkooh No.131 sand.

2.2. Leachate characteristics

The leachate used in this research was prepared and combined with the specific weight of fat (cooking oils), protein (chicken rind), carbohydrates (bread), and fiber (vegetables and watermelon rind) in 11 days for each test to be more similar to municipal wastewater (Fig. 3). To ensure test repeatability, the combinations of leachate had to closely resemble one another. Each test required 4 liters of pollutant, which consisted of 3.5 liters of leachate, 100 cc of edible red colorant, and 400 cc of water. The addition of red colorant had aided in visually tracking the movement of the pollutant within the soil, allowing for straightforward observation and analysis. The characteristics of the leachate used in this research are shown in Table 2.

(a) **(b)**

Fig. 3. (a) Produced rubbish after 11 days and (b) Collecting leachate for experimental procedure.

Table 2. Characteristics of the leachate used in this research.

Parameter	Unit	Value	Test Specification
pH	-	7.1	[32]
Ammonia	mg/L	2470	[33]
TSS	mg/L	14500	[34]
COD	mg/L	190100	[35]
BOD	mg/L	45500	[36]
TDS	mg/L	579	[37]

3. Method

3.1. Experimental investigation

This experiment was divided into two parts: the first part focused on unsaturated soil in the drying path, while the second part examined initially dry soil conditions. Each part of the experiment consisted of four tests, where the soil was subjected to different density levels: 40, 60, 80, and 100% in each test. To perform these tests, a rectangular glass cube measuring 120 × 8× 80 cm^3 with 1 cm thickness was specifically constructed as an experimental chamber to examine the movement of municipal landfill leachate through unsaturated soil. Fig. 4 shows the schematic view of the experimental setup and rainer system. The choice of a low thickness for the cube experimental box served two purposes: first, it allowed for a more detailed investigation of pollutant emission along the length and width of the soil, and second, it minimized two-dimensional numerical modeling errors. To ensure proper soil saturation and water table regulation, two valves were positioned at the bottom of the chamber (Fig. 4a). These valves were covered with geotextile material to prevent sand from being washed away during water entry and exit. To achieve uniform filling and reach the desired densities of the soil in the experimental box, a carefully designed rainer system was employed (Fig. 4b).

To perform the first part of the experimental test, the container box was filled with soil up to a height of 60 cm, and then the bottom valves were opened to ensure complete soil saturation with water. Following saturation, the container remained untouched for a 24-hour period to facilitate the release of any trapped air bubbles. Afterward, the water level was regulated by opening the lower valves, lowering it to around 10 cm from the container's bottom, considering the capillary level (Table 3). Then, a 24-hour period was provided for the soil to attain equilibrium relative humidity before introducing the pollutant for penetration.

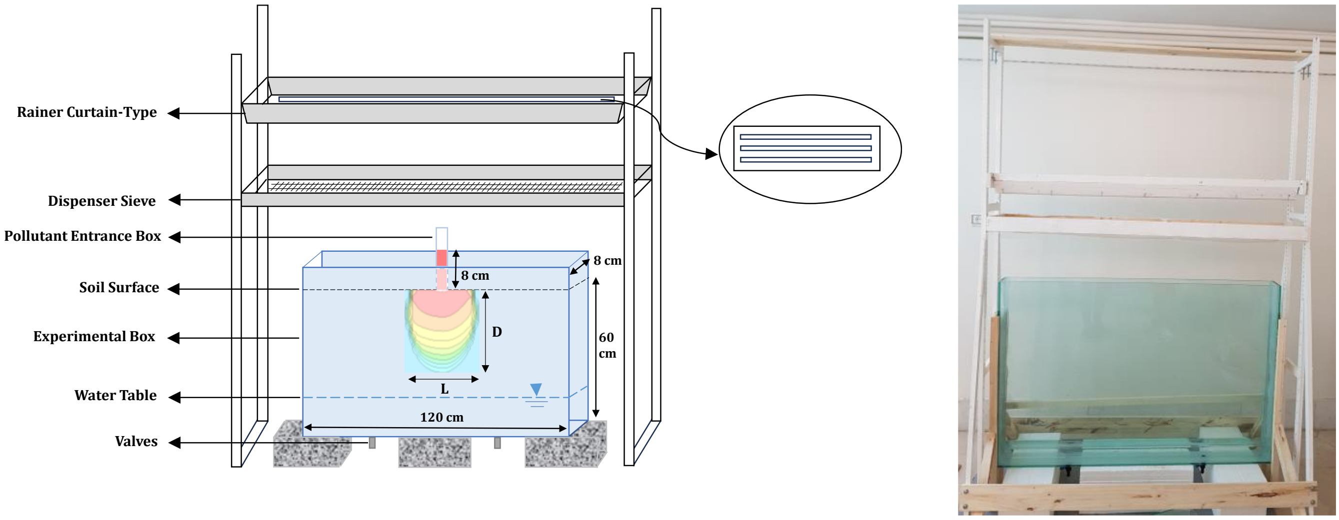

(a) **(b)**

Fig. 4. (a) Schematic of experimental setup and (b) Chamber (container) box and rainer system.

Table 3. Mechanical specifications of the expanded masonry unit.

Density (%)	40	60	80	100
Capillarity level (cm)	6	7	8	8

To perform the second part of the experimental test, the container box was also filled with soil up to 60 cm, and the bottom valves were opened to allow water to reach the desired height of 10 cm, considering the capillary level (Table 3). The difference between the second part and the first part was that the soil was not saturated in the second part (Fig. 5). Then, similar to the first section, a 24-hour period was provided for the soil to attain equilibrium relative humidity. Afterward, the pollutant penetration process was initiated. As shown schematically in Fig. 4a, the pollutant penetrated into the soil through a rectangular glass cube chamber with dimensions of 20¬×¬7×¬3 cm^3 and with a fixed head of 3 cm. The pollutant chamber is placed in the center of the glass box due to symmetry. In the second part, just before the pollutant penetration, soil sampling was conducted using a PVC tube with a diameter of 3 cm, enabling the collection of soil samples from different depths. The water content at various depths was then measured to obtain a water content profile before the testing began (Fig. 6).

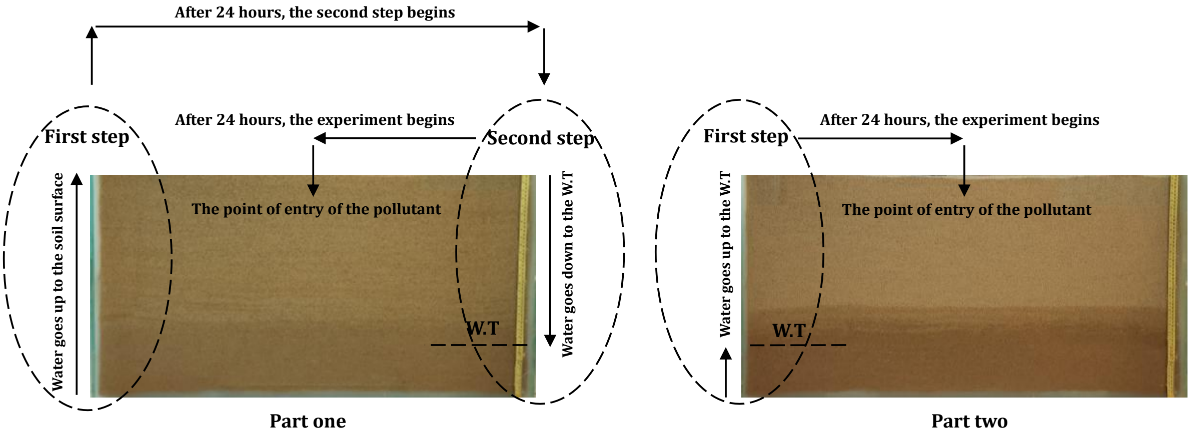

Fig. 5. The difference between part one (Unsaturated soil in drying path) and part two (Initially dry soil) of experimental tests.

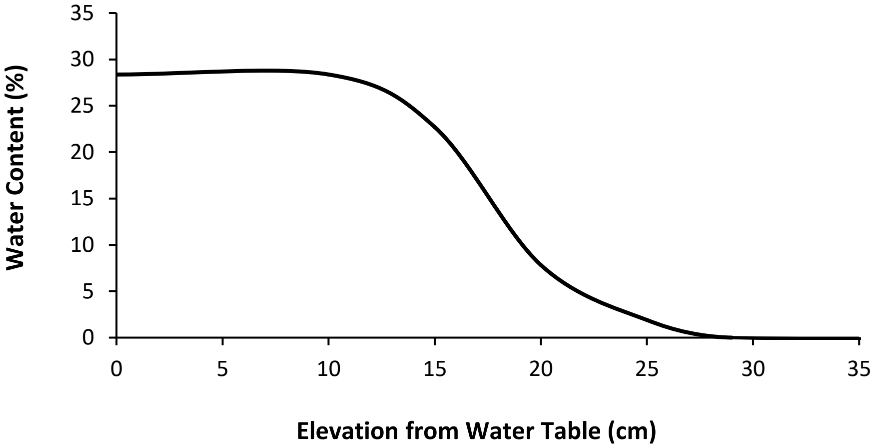

Fig. 6. Percentage of water content in the depth of the soil.

3.2. Numerical modeling

In this research, SEEP/W and CTRAN/W packages from Geostudio were used to model pollutant emissions. The Density-Dependent Analysis in SEEP/W, which combines CTRAN and SEEP, was utilized to study emissions under various relative densities. SEEP/W, developed by GeoStudio, specializes in modeling groundwater flow through porous media like soil [38, 39]. Understanding hydraulic conditions is crucial for investigating pollutant emissions in such media, as they directly affect contaminant transport. Appropriate material properties, such as soil hydraulic conductivity, were defined to represent these conditions and simulate pollutant transport. Defining the soil-water characteristic curve (SWCC) is very important to estimate the behavior of unsaturated soil. As input parameters for defining the SWCC curve, the saturated permeability (Table 4) and specifications of the 131 standard Firoozkooh sand were determined through experimental measurements (Table 1). Fig. 7 illustrates the functions of the SWCC curve for the unsaturated soil for 131 standard sands of Firoozkooh at different density.

Table 4. Firoozkooh sand soil properties in numerical modeling.

Density (%)	Saturated permeability (m/s)	Porosity
40	79×10-5	0.927
60	51×10-5	0.848
80	30×10-5	0.769
100	15×10-5	0.69

Through mesh studies, the mesh dimensions were set to 0.02 m2, and nine Gaussian points were used to ensure accurate representation. The boundary conditions of the model included specifying the groundwater table elevation (10 cm depth from the bottom of the model), using a constant head for the region of pollutant penetration, and using a spatial function for pressure head that was applied to establish varying pressure head values at different depths above the water table [40].

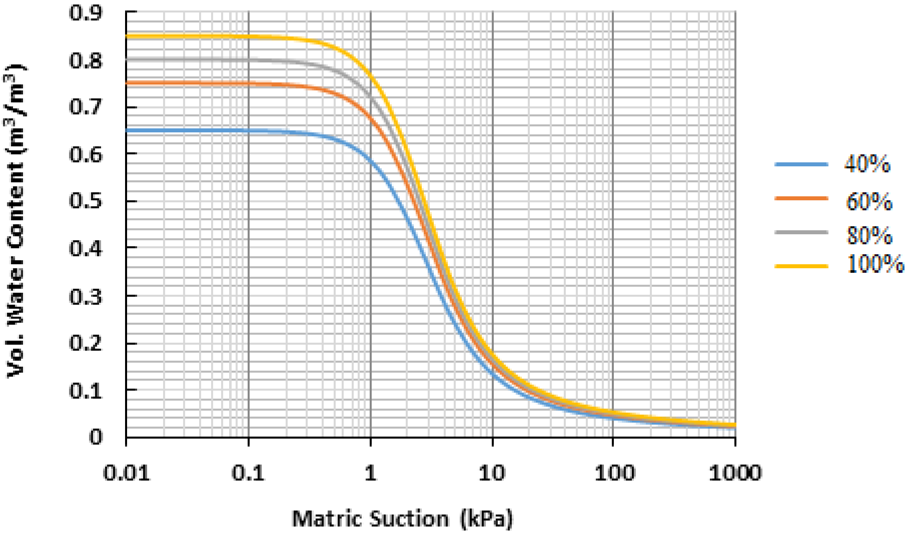

Fig. 7. SWCC curve for unsaturated soil in different densities.

In dry conditions, by utilizing available water content profiles at different depths and applying Eqs. 1 and 2, the volumetric water content can be calculated for each depth. Consequently, the water negative pressure head can be obtained by referring to the SWCC curve for each respective depth.

$$Sr\,.W = Gs\,.e \tag{1}$$

$$Sr\,.n = \theta \tag{2}$$

In these Equations, S_r, w, e, G_s, n, and θ, represent degree of saturation, water content, void ratio, specific volume, porosity, and volumetric water content respectively. Fig. 8 shows a difference in water negative pressure head between unsaturated soil in the drying path and initially dry soil.

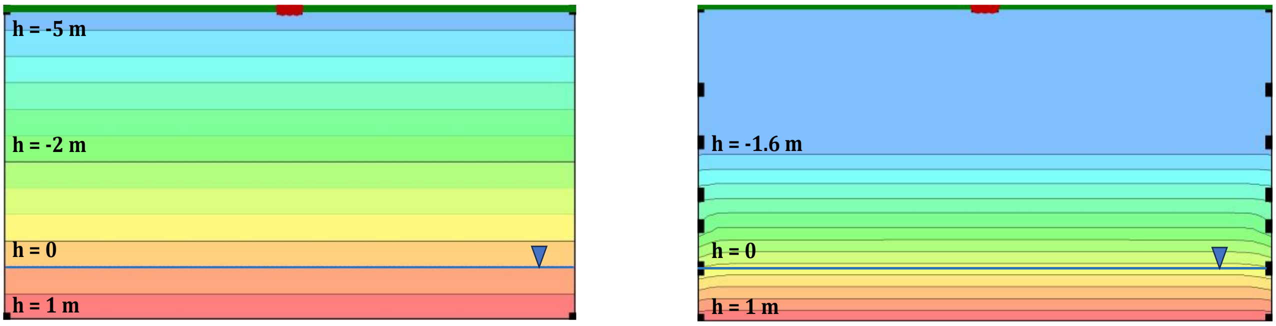

(a) (b)

Fig. 8. Comparison water negative pressure head between (a) unsaturated soil in drying path and (b) initially dry soil.

The SEEP/W model was converted to CTRAN/W, requiring the determination of pollutant attributes like diffusion and dispersion. Using Kuo [41] guidelines, the diffusion coefficient and dispersion coefficients were set, longitudinal dispersion coefficient of 0.1 times the length of the relevant dimensions. Pollutant entry conditions were defined at a constant concentration of 1 g/m³, and the model was analyzed with specific time steps. Parameters used in SEEP/W and CTRAN/W are detailed in Table 5, with pollutant emission analyzed for dry and unsaturated soil at 5, 50, 150, and 250 seconds.

Table 5. Numerical model details.

Parameter	Unit	Value
The relative density of pollutant	-	1.2
Pollutant head	cm	3
The water level of groundwater	cm	10
Longitudinal Dispersivity	m	0.12
Transverse Dispersivity	m	0.06
Diffusion	m^2/s	10-9
Time	s	400
Width of the model	cm	60
Length of model	cm	120

3.3. Image processing

In this study, MATLAB was used for image analysis. Images from an experimental chamber box containing soil and pollutant emissions were processed to generate visual representations in the form of curves. These curves illustrated changes in color intensity across pixels at varying soil depths, revealing pollutant distribution and behavior. Initially, a pre-leakage image was captured to document the test box and lighting conditions. Consistent lighting was maintained for subsequent images taken at various leakage stages. Images, originally in RGB color space, were converted to grayscale using a binary filter and then transformed into HSV color space, focusing on the value band. Average and median filters were applied to reduce noise. Figs. 9 and 10 illustrate the image processing algorithm with the applied filters.

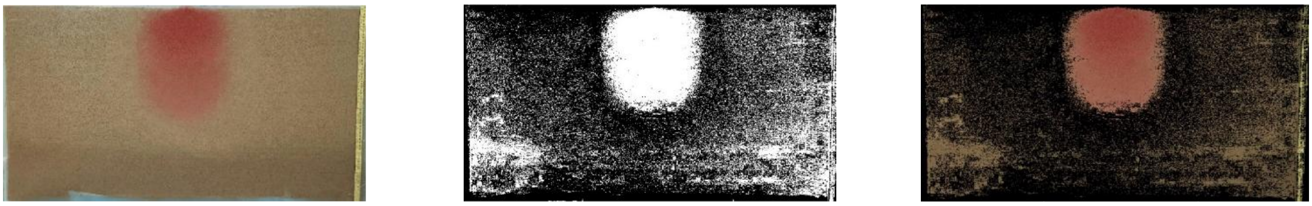
(a) (b) (c)

Fig. 9. Function of image processing algorithm (a) Image in RGB color space, (b) Image in binary space, (c) Using binary image as a filter on RGB image.

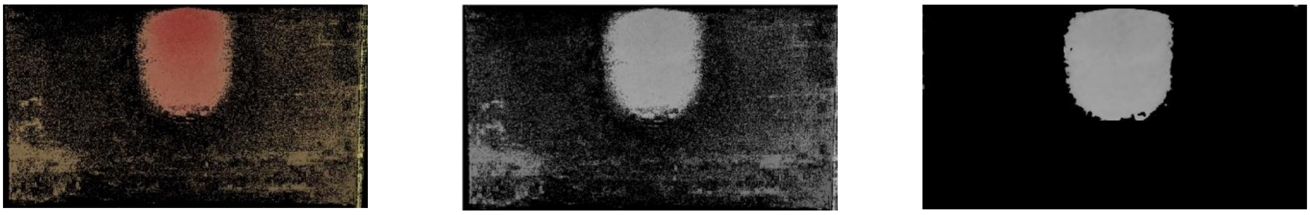
(a) (b) (c)

Fig. 10. Using average and median filter on image (a) Using binary image as a filter on RGB image, (b) Image in HSV color space, (c) Filtered image.

A curve showing color intensity variation with soil depth was plotted (Fig. 11a), then transformed into a concentration curve proportional to depth. The curves were calibrated to show 100% concentration at maximum color intensity and 0% at minimum. Due to inherent noise, a linear function fit was applied to compare these curves with concentration curves derived from the FEA. Fig. 11b shows the concentration change curve with respect to depth, as produced by GeoStudio.

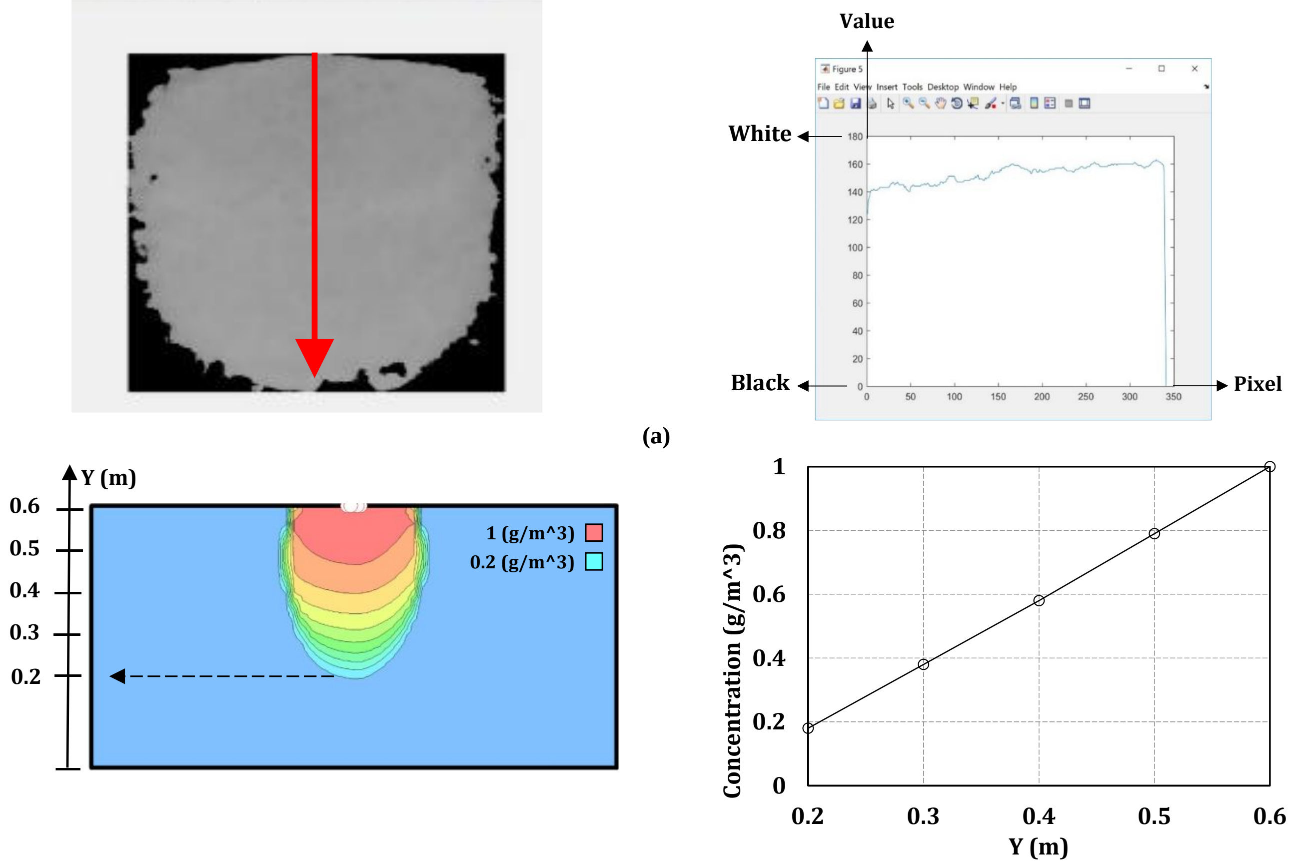

(a)

(b)

Fig. 11. Change in concentration in soil depth estimated by (a) MATLAB (b) Numerical analysis.

4. Results and discussion

4.1. Density and condition impact on penetration depth

Fig. 12 compares pollutant penetration in different soil densities under both dry and unsaturated conditions. The experimental results indicate that pollutants tend to penetrate dry soil at a faster rate compared to unsaturated soil. Capillary forces, caused by the surface tension of moisture in soil pores, play a crucial role in slowing down the movement of pollutants in unsaturated soil. When soil is unsaturated, these capillary forces tend to retain moisture within the soil matrix, making it more difficult for pollutants to infiltrate. In dry soil, these capillary forces are largely absent, allowing pollutants to move more freely through the larger air-filled pores. Moreover, Unsaturated soil typically contains some moisture that can interact with pollutants through sorption (absorption processes). These interactions can temporarily hold pollutants in the soil and reduce their mobility. In contrast, dry soil has limited or no moisture content to facilitate these sorption mechanisms, resulting in less resistance to pollutant movement. On the other hand, in unsaturated soil, the presence of water leads to higher viscosity, which creates more drag on pollutant particles as they move through the soil. In dry soil, with minimal moisture content, the viscosity is lower, resulting in reduced resistance to pollutant penetration.

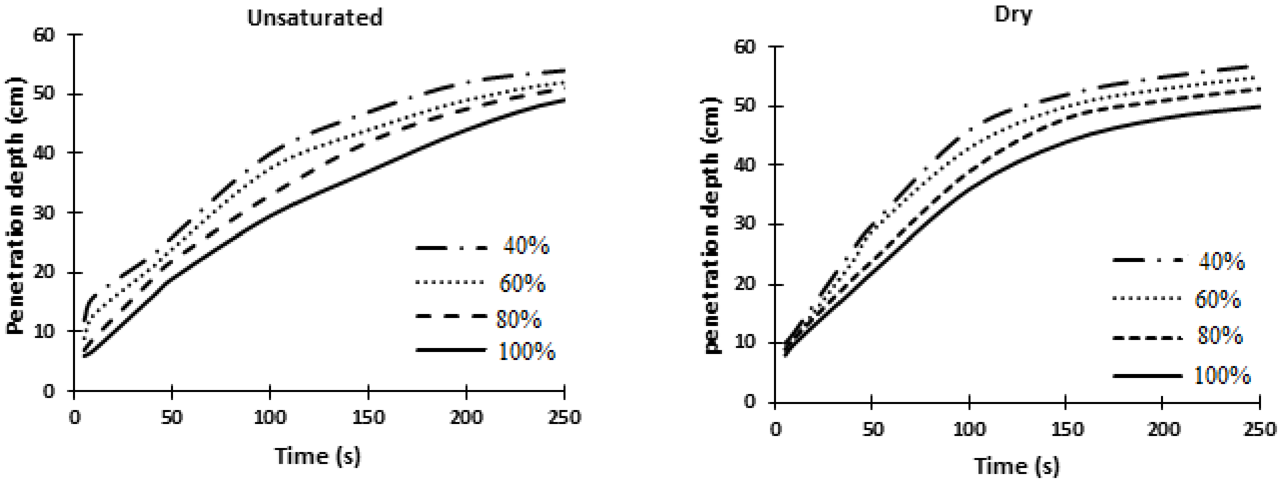

Fig. 12. Penetration depth of the pollutant by passing time in different densities in experimental tests on unsaturated and dry soil.

Fig.s 13 and 14 present a comprehensive comparison between numerical analysis and experimental test results for different densities. The curves depicted in Fig.s 13 and 14 demonstrate a satisfactory level of consistency between the numerical and experimental states. The results show that the numerical models estimate the pollutant penetration into the soil in unsaturated soil about 4% more than the experimental models. This is while the numerical models estimate the pollutant penetration into the soil in dry soil with 100% density about 5% less than the experimental models.

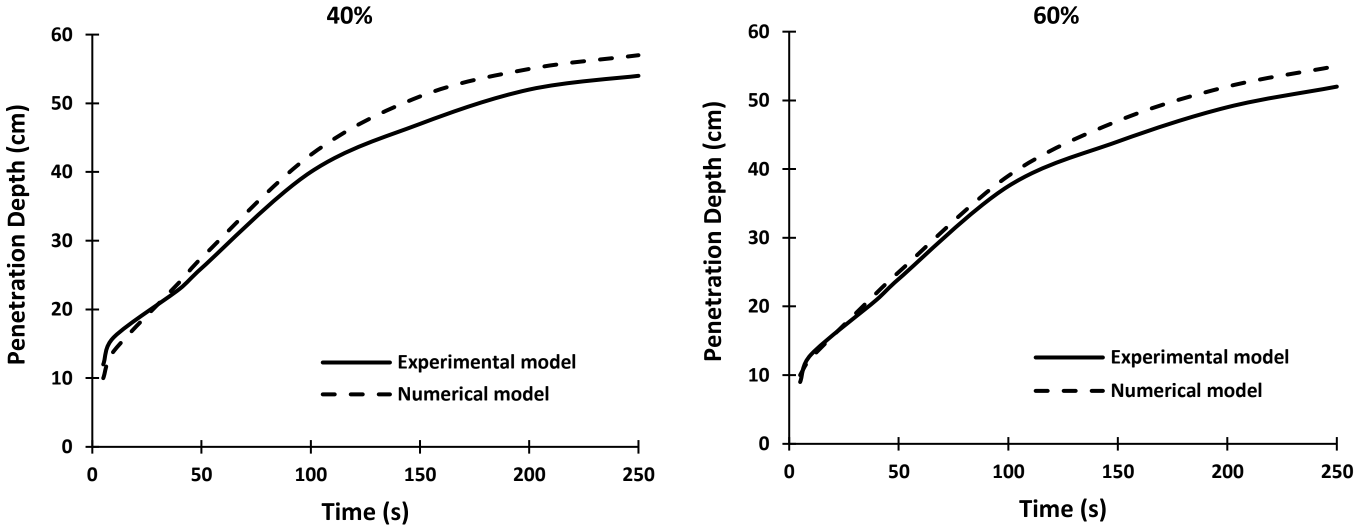

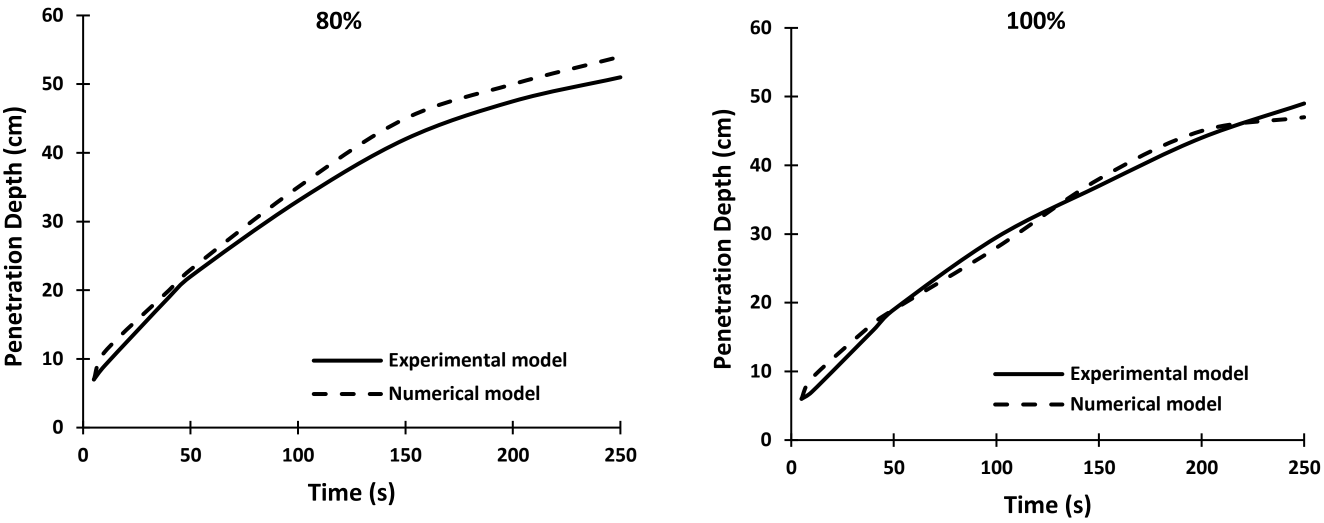

Fig. 13. Comparison between the results of numerical analysis and experimental test in unsaturated soil for different densities from 40% to 100%.

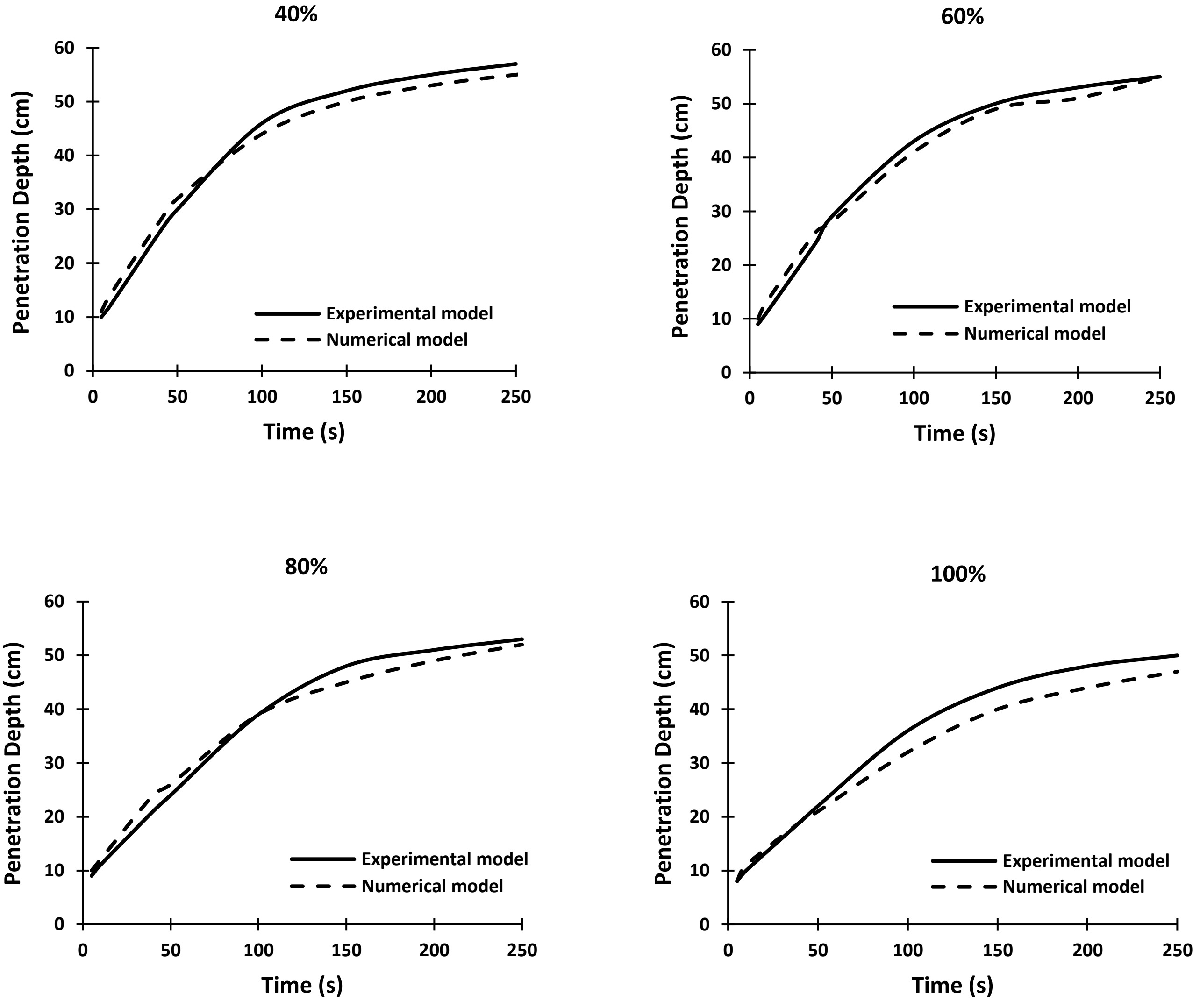

Fig. 14. Comparison of the results of numerical analysis and experimental test in dry soil for different densities from 40% to 100%.

4.2. Density and soil condition impact on penetration time

The time for the pollutant to reach the underground water (deep penetration) in four tests performed in unsaturated and dry conditions is presented in Fig. 15. As can be seen from the results, at the same density, the time of reaching the pollutant in dry soil is much less than that in unsaturated soil, which has been confirmed in previous researches. Also, according to the results of Fig. 15, it can be said that with the increase in the relative density of the soil, the time for the pollutant to reach the underground water has increased. The reason for this is that increasing the relative density of the soil reduces the empty space and porosity of the soil, reduces the hydraulic conductivity, and increases the resistance to the flow of water and pollutants. As a result, the speed of movement of pollutants decreases and the time they reach the underground water increases.

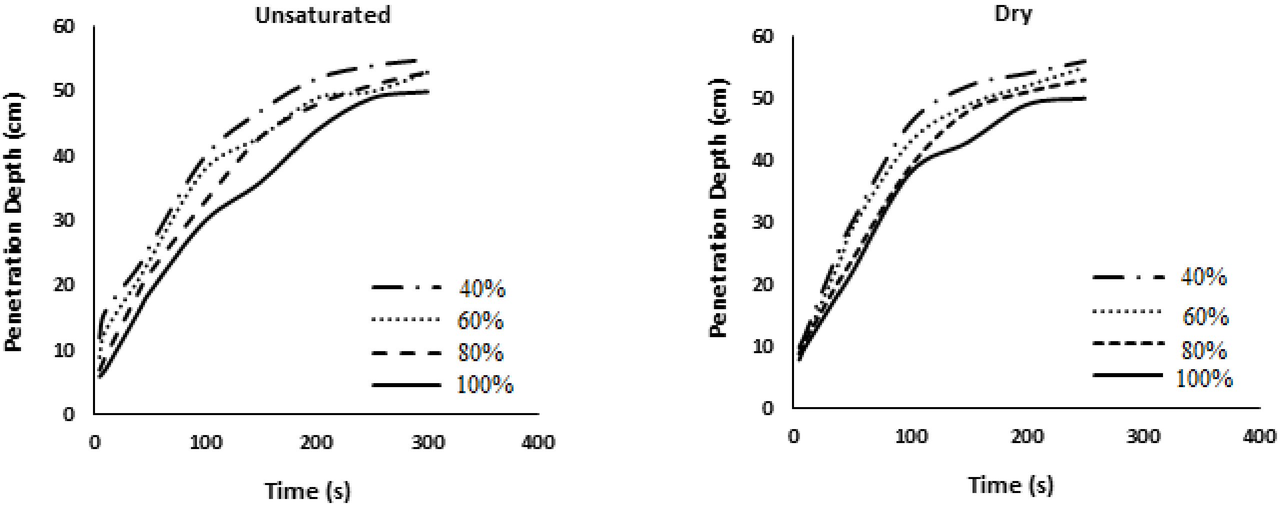

Fig. 15. Penetration time of pollutant at different densities on unsaturated and dry soil.

4.3. Longitude dispersivity

Based on the given explanation, it is expected that longitudinal dispersivity of pollutants in unsaturated soils is greater than that in dry soil (Fig. 16). According to the results of Fig. 16, longitudinal dispersivity in unsaturated soil is about 25 to 40% more than that in dry soil. This increase can be attributed to the presence of water in unsaturated soils, which enhances diffusion and advection processes. Water films around soil particles create pathways that facilitate pollutant movement, leading to higher dispersivity. Additionally, soil-water interactions affect hydraulic conductivity and porosity, promoting more extensive mixing and spreading of contaminants. Capillary forces in unsaturated soils also play a role by creating preferential flow paths, increasing overall dispersivity. These findings highlight the importance of considering soil moisture when evaluating pollutant dispersivity. The observed 25 to 40% increase in dispersivity in unsaturated soils emphasizes the need for detailed hydrogeological studies to accurately predict and manage pollutant spread in different soil conditions.

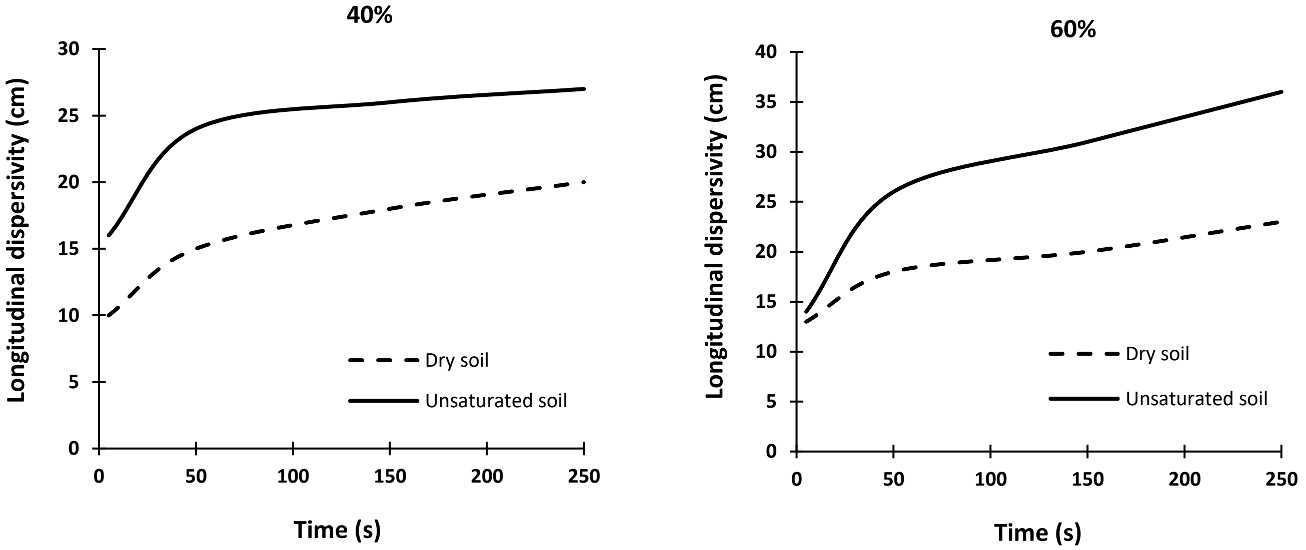

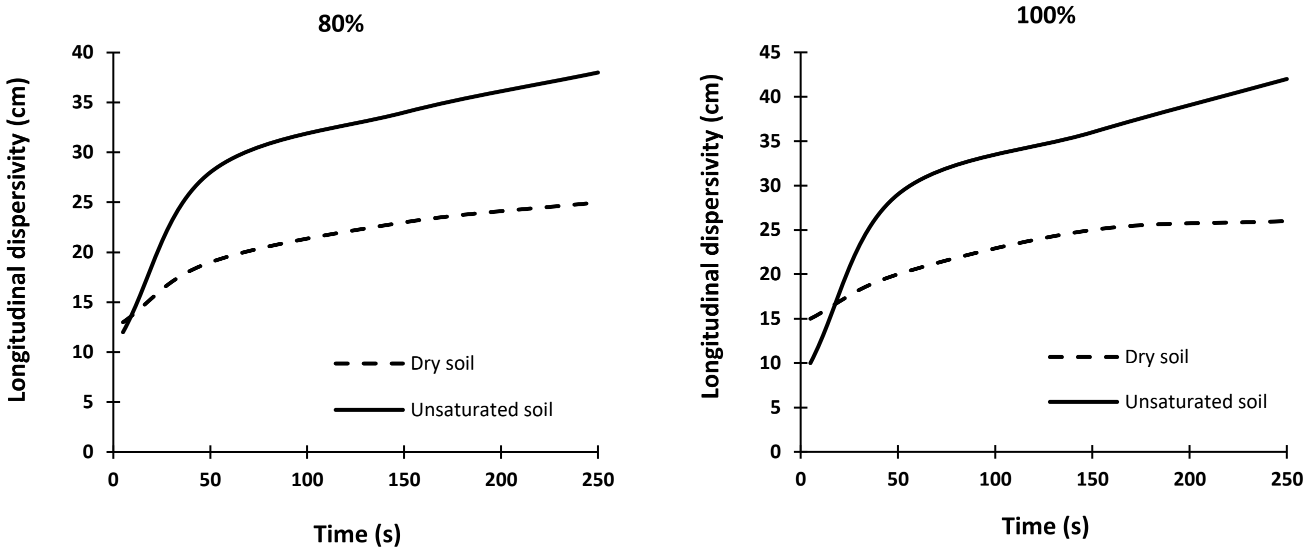

Fig. 16. Comparison of longitudinal dispersivity of pollutants in unsaturated and dry soil with different densities from 40% to 100% in experimental tests

Subsequently, Figs. 17 and 18 provide a comparison between pollution emissions in a numerical and an experimental model specifically at 100% density for unsaturated and dry condition, respectively. Based on the results, an intriguing phenomenon comes to light: in the dry soil, the penetration rate of pollutants into the soil depth is notably greater than their longitudinal expansion, a phenomenon that is not seen in unsaturated soil. Several factors contribute to this intriguing observation. Firstly, in dry soil, the absence of moisture limits lateral movement, causing pollutants to predominantly travel in the path of least resistance, vertically downward. Without the presence of water to aid in lateral dispersion, pollutants are more likely to percolate deeper into the soil, potentially reaching groundwater reservoirs and posing a heightened risk to water quality. Secondly, the compacted nature of dry soil hinders the spread of contaminants laterally, leading to a concentration of pollutants in the immediate vicinity of their source. Thus, the combination of limited horizontal movement and enhanced vertical penetration results in a higher potential for contaminants to infiltrate deeper soil layers, necessitating increased vigilance in managing pollutant sources and their potential long-term impacts on soil and water ecosystems.

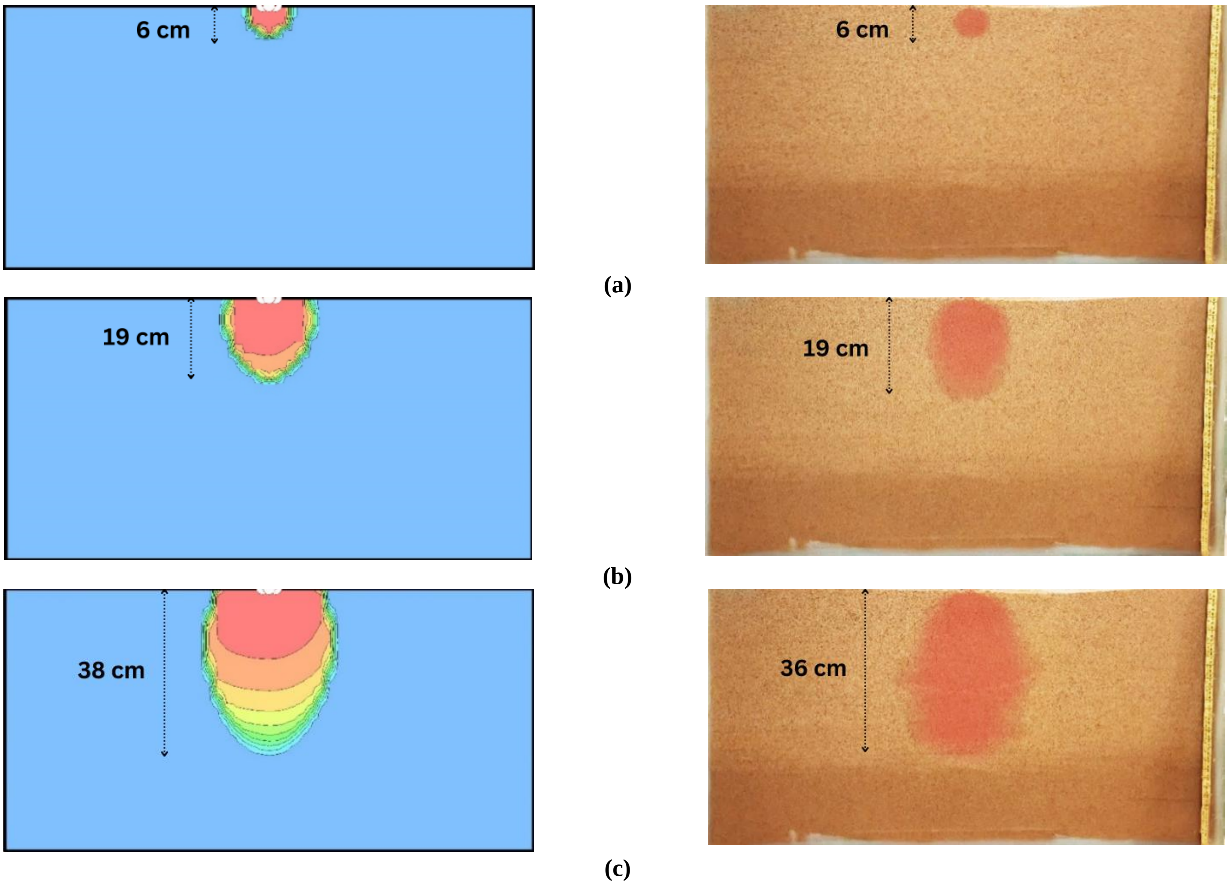

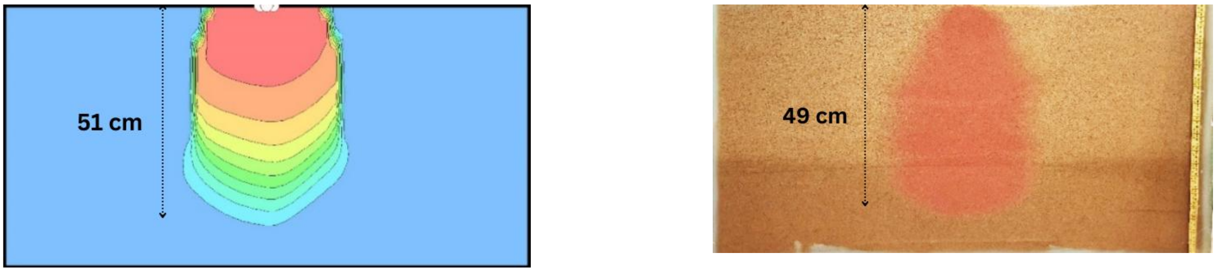

(d)

Fig. 17. Comparison between pollution emission in the experimental test and numerical analysis at unsaturated soil with 100% density at times: (a) 5, (b) 50, (c) 150, and (d) 250 second.

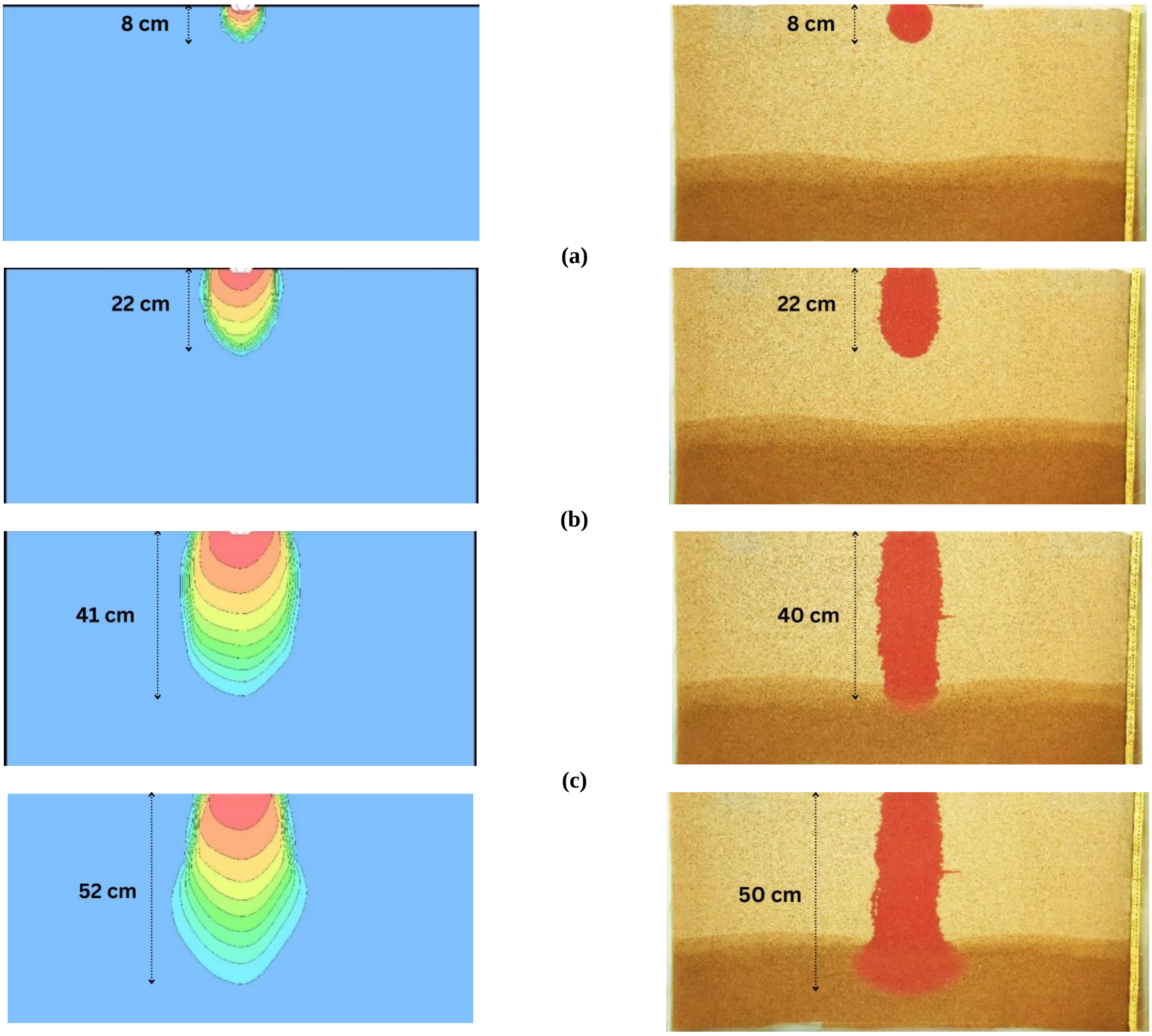

(a)

(b)

(c)

(d)

Fig. 18. Comparison of pollution emission in the experimental test and numerical analysis at dry soil with 100 % density at times: (a) 5, (b) 50, (c) 150, and (d) 250 second.

4.4. Verifying image processing analysis

In this analysis image analysis method was used for estimating the pollutant penetration in depth of sandy soils. For sandy soils with densities ranging from 40% to 100%, Fig. 19 shows a comparison of the curves generated from image analysis and finite element models (GeoStudio). Based on the depicted curves, it can be observed that the concentration curves obtained from both image analysis and FEM exhibit a similar rate of decline. As a result, it appears that these approaches can accurately (and with a small margin of error) predict the soil pollution concentration. Differences between image analysis and FEM curves reduced approximately from 8% to 1% as soil density increased. It should be noted, though, that the variation in backdrop color within the soil saturation region impacts the intensity of the pollutant's color when it enters the groundwater. Consequently, image analysis may not accurately predict the concentration in such cases. It is, therefore, recommended to focus on examining the concentration changes near the boundary between the pollutant and the groundwater level, where the impact of color intensity variations is prominent.

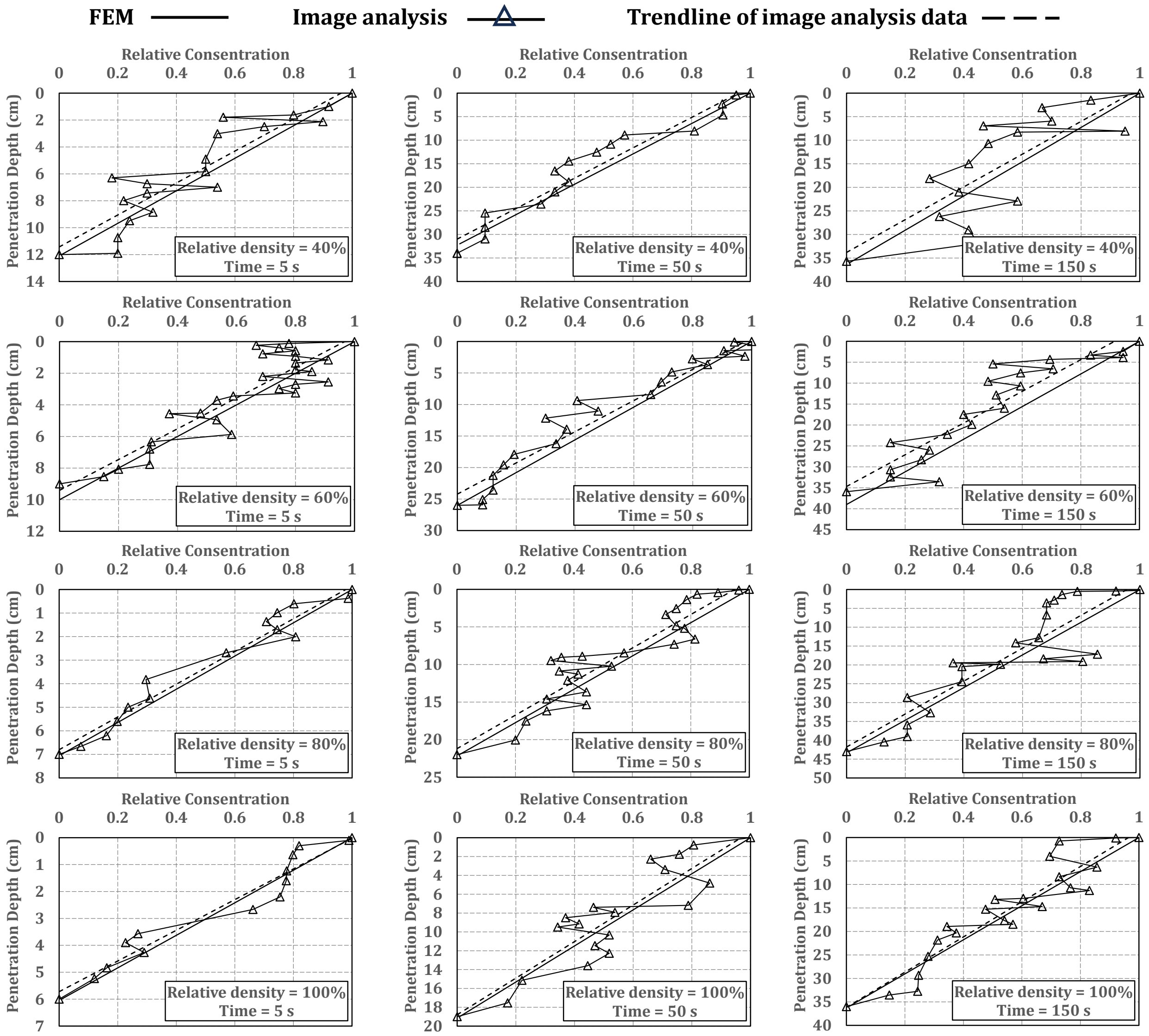

Fig. 19 Comparison of concentration curve in FEM and image analysis in soil (to the level of groundwater).

5. Conclusions

In recent years, the pollution of underground water resources and soils by pollutants such as petroleum products and waste leachate has become a serious global environmental problem. Soil contamination affects underground water tables and impacts environmental geotechnics, as physical-chemical interactions between soil and pollutants can alter soil properties like resistance, permeability, and compressibility, leading to potential issues. Since soil is often in an unsaturated state when pollutants are released, studies and modeling must consider unsaturated conditions. This research aims to investigate the distribution of municipal waste leachate in unsaturated and dry soils, identify effective parameters in unsaturated soils, develop a numerical model to predict leachate release, and use image processing to estimate pollution concentration and compare it with the numerical and experimental models. The key findings are as follows:

- Discrepancies in longitudinal pollutant expansion between numerical and experimental models may result from slight errors in laboratory measurements and the anisotropic nature of permeability.
- Relative density, permeability, matric suction, gradient, and water content are key parameters influencing pollutant emission.
- Increasing relative density reduces pollutant penetration depth but increases longitudinal penetration.
- Pollutant penetration in initially dry soil is faster compared to unsaturated soil in the drying path due to increased gradient.
- Image processing accurately estimates pollutant concentration at different depths in soils even before reaching the water table.
- Numerical, experimental, and image processing results show good agreement with each other.
- Increasing soil density leads to improved consistency between image processing and finite element model results.

Statements & Declarations

Author contributions

Narges Soleimanian: Investigation, Formal analysis, Validation, Writing - Original Draft, Writing - Review & Editing.

Ali Akhtarpour: Investigation, Formal analysis, Validation, Resources, Project administration, Supervision, Writing - Original Draft, Writing - Review & Editing.

Mohammad Saleh Baradaran: Conceptualization, Methodology, Writing - Review & Editing.

Funding

The authors received no financial support for the research, authorship, and/or publication of this article.

Data availability

The data presented in this study will be available on interested request from the corresponding author.

Declarations

The authors declare no conflict of interest.

References

[1] Ayar, P., Baradaran, S., Abdipour Vosta, S. A Review on the Effect of Various Additives on Mechanical Properties of Stone Mastic Asphalt (SMA). Road, 2022; 30: 57-86. doi:10.22034/road.2021.295635.1969.

[2] Almahmodi, R., Abdalhusein, M. M., Akhtarpour, A., Mahmood, M. S. Characterization of collapsible gypsum sand soil with the presence of matric suction using a modified odometer apparatus. The International Journal of Advanced Manufacturing Technology, 2022; doi:10.1007/s00170-022-10146-x.

[3] AlNaddaf, H. Q. A., Kouzegaran, S., Akhtarpour, A., Fattah, M. Y. Effects of Cement Treatment on the Behavior of Unsaturated Gypseous Soils. Transportation Infrastructure Geotechnology, 2025; 12: 140. doi:10.1007/s40515-025-00602-y.

[4] Baradaran, S., Aliha, M. R. M., Maleki, A., Underwood, B. S. Fracture properties of asphalt mixtures containing high content of reclaimed asphalt pavement (RAP) and eco-friendly PET additive at low temperature. Construction and Building Materials, 2024; 449: 138426. doi:10.1016/j.conbuildmat.2024.138426.

[5] Baradaran, S., Ameri, M. Investigation of Rutting Failure in Asphalt Mixtures and Its Improvement Strategies. Road, 2023; 31: 53-70. doi:10.22034/road.2022.337945.2041.

[6] Baradaran, S., Rahimi, J., Ameri, M., Maleki, A. Mechanical performance of asphalt mixture containing eco-friendly additive by recycling PET. Case Studies in Construction Materials, 2024; 20: e02740. doi:10.1016/j.cscm.2023.e02740.

[7] Balighi, M., Baradaran, M. S., Akhtarpour, A. Numerical investigation of swelling soil behavior and its effect on gas well casing internal forces based on unsaturated soil mechanics, case study: Khangiran, Sarakhs. Amirkabir Journal of Civil Engineering, 2024; 56: 885-908. doi:10.22060/ceej.2024.22616.8006.

[8] Baradaran, S., Aliha, M. R. M. Mode I and Mode II fracture assessment of green asphalt pavements containing plastic waste and RAP at low and intermediate temperature. Results in Engineering, 2025; 25: 103734. doi:10.1016/j.rineng.2024.103734.

[9] Baradaran, S., Ziaee, S. A. Review of the Mechanical Properties of Asphalt Pavement Reinforced with Natural Plant Fibers as an Eco-Friendly Solution in Pavement Engineering. Road, 2025; 33: 167-192. doi:10.22034/road.2025.471341.2308.

[10] Akhtarpour, A., Khodaii, A. Nonlinear Numerical Evaluation of Dynamic Behavior of an Asphaltic Concrete Core Rockfill Dam (A Case Study). Journal of Seismology and Earthquake Engineering, 2009; 11: 143-152.

[11] Niri, S. R., Akhtarpour, A., Daliri, F., Baradaran, M. S. Experimental investigation of dewatering silty tailings using electrokinetic method. Canadian Geotechnical Journal, 2025; 62: 1-25. doi:10.1139/cgj-2024-0069.

[12] Abdulameer AlNaddaf, H. Q., Kouzegaran, S., Fattah, M. Y., Akhtarpour, A. Effects of Cement Treatment on Water Retention Behavior and Collapse Potential of Gypseous Soils: Experimental Investigation and Prediction Models. Advances in Civil Engineering, 2024; 2024: 6637911. doi:10.1155/2024/6637911.

[13] Wang, X., Gao, Y., Jiang, X., Zhang, Q., Liu, W. Analysis on the Characteristics of Water Pollution Caused by Underground Mining and Research Progress of Treatment Technology. Advances in Civil Engineering, 2021; 2021: 9984147. doi:10.1155/2021/9984147.

[14] Mineo, S. Groundwater and soil contamination by LNAPL: State of the art and future challenges. Science of The Total Environment, 2023; 874: 162394. doi:10.1016/j.scitotenv.2023.162394.

[15] Abbas, S. Z., Rafatullah, M. Recent advances in soil microbial fuel cells for soil contaminants remediation. Chemosphere, 2021; 272: 129691. doi:10.1016/j.chemosphere.2021.129691.

[16] Baradaran, M. S., Aftabi Sani, A., abrishami, S. Application of Differential Transform Method for Solving Free-Surface Seepage Problem of One-Dimensional Porous Media. Ferdowsi Civil Engineering, 2024; 37: 1-18. doi:10.22067/jfcei.2024.82170.1226.

[17] Baradaran, M. S., Qazanfari, R., Baradaran, S. Study of soil reinforcement in the east of Mashhad using glass granule. Materials Research Express, 2023; 10: 055202. doi:10.1088/2053-1591/acd5af.

[18] Pargar, J., Akhtarpour, A., Baradaran, M. S. An Unsaturated Soil Mechanics-Based Numerical and Experimental Method to Assess Soil Settlement Due to Ground Water Level Rise. Transportation Infrastructure Geotechnology, 2024; 11: 3621-3646. doi:10.1007/s40515-024-00422-6.

[19] Tareghian, B., Baradaran, M. S., Akhtarpour, A. The effect of sand-crumb rubber mixture treatment on the seismic response of a low-rise building located on liquefiable soil. Discover Geoscience, 2024; 2: 11. doi:10.1007/s44288-024-00014-4.

[20] Pournoori, P., Davarpanah T.Q, A., Rajaee, A., Ghodratnama, M., Abrishami, S., Masoodi, A. R. Experimental exploration of fracture behavior (pure mode III) in eco-friendly steel fiber-reinforced self-compacting concrete with waste tempered glass as coarse aggregates. Scientific Reports, 2024; 14: 9043. doi:10.1038/s41598-024-58912-z.

[21] Eltarabily, M. G. A., Negm, A. M. Numerical Simulation of Fertilizers Movement in Sand and Controlling Transport Process via Vertical Barriers. International Journal of Environmental Science and Development, 2015; 6: 559-565. doi:10.18178/IJESD.

[22] Szymański, K., Janowska, B., Iżewska, A., Sidełko, R., Siebielska, I. Method of evaluating the impact of landfill leachate on groundwater quality. Environmental Monitoring and Assessment, 2018; 190: 415. doi:10.1007/s10661-018-6776-2.

[23] Sharma, A., Ganguly, R., Kumar Gupta, A. Impact Assessment of Leachate Pollution Potential on Groundwater: An Indexing Method. Journal of Environmental Engineering, 2020; 146: 05019007. doi:10.1061/(ASCE)EE.1943-7870.0001647.

[24] Javahershenas, M., Nabizadeh, R., Alimohammadi, M., Mahvi, A. H. The effects of Lahijan landfill leachate on the quality of surface and groundwater resources. International Journal of Environmental Analytical Chemistry, 2022; 102: 558-574. doi:10.1080/03067319.2020.1724984.

[25] Alghamdi, A. G., Aly, A. A., Ibrahim, H. M. Assessing the environmental impacts of municipal solid waste landfill leachate on groundwater and soil contamination in western Saudi Arabia. Arabian Journal of Geosciences, 2021; 14: 350. doi:10.1007/s12517-021-06583-9.

[26] Hussein, M., Yoneda, K., Mohd-Zaki, Z., Amir, A., Othman, N. Heavy metals in leachate, impacted soils and natural soils of different landfills in Malaysia: An alarming threat. Chemosphere, 2021; 267: 128874. doi:10.1016/j.chemosphere.2020.128874.

[27] Nyika, J., Dinka, M., Onyari, E. Effects of landfill leachate on groundwater and its suitability for use. Materials Today: Proceedings, 2022; 57: 958-963. doi:10.1016/j.matpr.2022.03.239.

[28] Alao, J. O. Impacts of open dumpsite leachates on soil and groundwater quality. Groundwater for Sustainable Development, 2023; 20: 100877. doi:10.1016/j.gsd.2022.100877.

[29] Zango, M. U., Kassim, K. A., Sa'ari, R., Rashid, M. F. A., Muhammed, A. S., Ahmad, K., Makinda, J. Use of digital image technique to study leachate penetration in biocemented residual soil. Materials Today: Proceedings, 2022; 48: 734-740. doi:10.1016/j.matpr.2021.02.211.

[30] Vafaei, N., Fakharian, K., Sadrekarimi, A. Sand-sand and sand-steel interface grain-scale behavior under shearing. Transportation Geotechnics, 2021; 30: 100636. doi:10.1016/j.trgeo.2021.100636.

[31] Behdad, A., Moradi, M., Afshari Aghajari, A. The Effect of Soil–Cement Barriers in Containing the LNAPL Contaminants Transport in Unsaturated Soil; A Physical Modeling. Soil and Sediment Contamination: An International Journal, 2022; 31: 692-714. doi:10.1080/15320383.2021.2000364.

[32] Buck, R. P., Rondinini, S., Covington, A. K., Baucke, F. G. K., Brett, C. M. A., Camoes, M. F., Milton, M. J. T., Mussini, T., Naumann, R., Pratt, K. W., Spitzer, P., Wilson, G. S. Measurement of pH. Definition, standards, and procedures (IUPAC Recommendations 2002). 2002; 74: 2169-2200. doi:doi:10.1351/pac200274112169.

[33] Schwab, J. J., Li, Y., Bae, M.-S., Demerjian, K. L., Hou, J., Zhou, X., Jensen, B., Pryor, S. C. A Laboratory Intercomparison of Real-Time Gaseous Ammonia Measurement Methods. Environmental Science & Technology, 2007; 41: 8412-8419. doi:10.1021/es070354r.

[34] Nasrabadi, T., Ruegner, H., Sirdari, Z. Z., Schwientek, M., Grathwohl, P. Using total suspended solids (TSS) and turbidity as proxies for evaluation of metal transport in river water. Applied Geochemistry, 2016; 68: 1-9. doi:10.1016/j.apgeochem.2016.03.003.

[35] Kayaalp, N., Ersahin, M. E., Ozgun, H., Koyuncu, I., Kinaci, C. A new approach for chemical oxygen demand (COD) measurement at high salinity and low organic matter samples. Environmental Science and Pollution Research, 2010; 17: 1547-1552. doi:10.1007/s11356-010-0341-z.

[36] Siwiec, T., Kiedrynska, L., Abramowicz, K., Rewicka, A. L. E. K. S. A. N. D. R. A., Nowak, P. BOD measuring and modelling methods – review. Annals of Warsaw University of Life Sciences, 2011; 43: 143–153. doi:10.2478/v10060-008-0100-8.

[37] Boerlage, S. F. E. Measuring salinity and TDS of seawater and brine for process and environmental monitoring—which one, when? Desalination and Water Treatment, 2012; 42: 222-230. doi:10.5004/dwt.2012.2827.

[38] Alwan, A. H., Al-Adili, A. Numerical Analysis of Water and Crude Oil Flux from Clayey Soil by GeoStudio-SEEP/W. In: Geotechnical Engineering and Sustainable Construction; 2022 March 20; Singapore. p. 191-206. doi:10.1007/978-981-16-6277-5_16.

[39] Harish Kumar Reddy, P., Ramya Krishna, V., Srinivas, K. Design of landfill liners for fine grained soils using CTRAN/W. Materials Today: Proceedings, 2021; 45: 3413-3418. doi:10.1016/j.matpr.2020.12.857.

[40] Lu, N., Likos William, J. Suction Stress Characteristic Curve for Unsaturated Soil. Journal of Geotechnical and Geoenvironmental Engineering, 2006; 132: 131-142. doi:10.1061/(ASCE)1090-0241(2006)132:2(131).

[41] Kuo, J. Practical Design Calculations for Groundwater and Soil Remediation. 2nd ed. Florida (US): CRC Press; 2014. doi:10.1201/b17013.